Flavio Nucciarelli

DOCTORAL THESIS

# SURFACE MODIFICATION OF OPTOELECTONIC DEVICES WITH GALLIUM NANOPARTICLES

Universidad Autónoma de Madrid

FACULTAD DE CIENCIAS

Madrid, June 2019

# *Ringraziamenti (Acknowledgements)*

# *Resumen*

El presente trabajo aborda la investigación y desarrollo de procedimientos de modificación de superficies mediante el uso de nanopartículas (NPs) de galio. En primer lugar se diseñó un método nuevo para producir coloides de galio en diferentes disolventes. Las nanopartículas fueron evaporadas térmicamente sobre una capa sacrificable de oxido de zinc dopado con aluminio (AZO) para posteriormente ser transferidas a disolventes como tetrahidrofurano (THF), agua desionizada (DIW) o etanol (EtOH). Las muestras permitieron investigar las características de absorcion plasmonica de superficie y volumen de las NPs.

Una vez determinada la propiedad óptica intrínseca de las nanoestructuras de galio, la tésis se focalizó en el estudio de distintos tratamientos químicos y de plasma para dar forma a los patrones superficiales con NPs. Mediante el proceso de ataque seco se obtuvieron estructuras nanocónicas. El proceso de modificación se basó en el factor de mérito altura/diámetro (h/d), dónde mediante la comparación con las NPs sin alterar se observó que cuanto más pequeño es el ratio h/d, mayor es la luz absorbida, hecho que se confirmó mediante simulaciones de campo lejano. Se realizaron cálculos analíticos adicionales de distintos ratios h/d que demostraron una mejora de hasta dos veces el campo cercano alrededor de la estructura modificada. Adicionalmente, se utilizaron las Ga NPs para fabricar nanocolumnas de silicio empleando las NPs como máscara durante el ataque seco. Debido a la elevada razón de aspecto de la nanocolumnas, se reduce la reflexión especialmente en el rango del infrarrojo. Dado que la superficie de modificación depende altamente de la densidad del recubrimiento de las nanoparticulas, se utiliza el ataque químico con ácido clorhídrico como procedimiento compatible con muchos procesos microelectrónicos

Por ultimo, se estudió el efecto de las NPs de galio sobre la superficie de fotodiodos de avalancha de InGaAs/InAlAs en combinación con una capa aislante de polimetilmetacrilato (PMMA). Esta actúa como una capa intermedia entre el Ga y la mesa para detener el fenómeno de conducción y reducir la corriente de fuga. Además, las

muestras fueron térmicamente tratadas para alterar la composición de las capas de NPs y por tanto, su permitividad efectiva. El tratamiento llevó a la mejora de, al menos, un 30% de la corriente generada por el dispositivo bajo iluminación.

La presente tesis ha recibido la financiación del programa PROMIS de investigación e innovación de Horizonte 2020 de la Unión Europea bajo el acuerdo de subvención Marie Sklodowaska-Curie número 641899.

# *Abstract*

This work aimed to the investigation and develop material surface modification procedures with the use of gallium nanoparticles (Ga NPs). Firstly, a new method to produce Ga colloids in different solvents was designed. The NPs were thermally evaporated on an aluminium zinc oxide (AZO) expendable layer to be transferred later to the solvent such as tetrahydrofuran (THF), deionized water (DIW) or ethanol (EtOH). The sample allowed to investigate the characteristic surface and bulk plasmonic absorptions of the growth NPs.

Once determined the intrinsic optical property of the Ga nanostructures, the thesis work focused on the study of plasma and chemical treatment for shaping and tuning NPs arrays. By means of dry etching process, nanocone structures were obtained. The reshaping process was based on the height/diameter (h/d) ratio figure of merit. Comparing to the unmodified NPs, the smaller the h/d, the higher the light absorbed value as also confirmed by far field simulations. Further analytic calculation of different h/d ratios demonstrated up to two fold enhancement of the near field around the modified structure. Additionally, the Ga NPs were also used to fabricate Si nanocolumns with a Ga cap. The exotic shape guaranteed remarkable antireflective coating property, especially in the near infrared range. Since the surface modification strongly depends on the NPs coverage density, our study found that chloridric acid wet etching – a compatible method with many microelectronic processes - can easily control this parameter.

Finally, Ga NPs were applied on an InGaAs/InAlAs avalanche photodiode surface jointly to a polymethylmethacrylate (PMMA) passivation layer. The latter helped as a buffer layer between the Ga and the mesa to stop conduction phenomena and reducing the leakage current contribution. Additionally, samples were thermally treated to tune the NPs layer physical composition, hence their effective permittivity. The treatment led to almost 30 % enhancement of the device light current generation. This thesis received funding from the European Union's Horizon 2020 research and innovation programme under the Marie Sklodowska-Curie grant agreement No 641899.

# Index

# Chapter 1
# Introduction

## 1.1 Metal nanoparticles plasmonic properties

In the last decades, nanotechnology science has been largely used to improve upcoming technologies in the human's everyday life, which are the fruit of new materials and devices innovations. But since the antiquity, dedicated and brilliant artisans manipulated materials to discover new properties and functionalities. Nanocomposite materials had been also used in the past to create weapons, artefacts and textiles.[1,2] One of the most noteworthy example is the Roman Lycurgus decorative treasure dated in A.D. 400, which is a cup made of glass with mixed gold-silver NPs that vary its colour when sun light pass through it. Prior to Romans, Damascus blacksmiths discovered the exceptional property of nanotubes and nanowires in steel to forge impressive resistance and sharp swords. Nowadays, nanomaterials have been used for a plenty of scopes, from biology (e.g. drug delivery)[3] to material surface properties modification (e.g. self-cleaning dye).[4] Because of their small dimensions, these structures show a high surface-to-volume ratio that allows the employment of uncommon physical and chemical properties compared to those in the bulk materials.

Among the possible effects, localized surface plasmonic resonance (LSPR) can be generated from the light interaction with a metal nanoparticle in a surrounded media. As it will explain in Chapter 2, if plasmon resonance condition is satisfied, the propagating wave in free space will transform into a surface wave whose propagation is limited by the dimensions of the nanoparticle. In fact, when light impinges on the NP, these surface waves produces collective oscillations of the electrons conforming the nanoparticle, which generates a surrounding electric field.

By means of LSPR, a multitude of effects to manipulate an incoming light signal has been possible. Subwavelength structures can act as nanoantennas for local electric field enhancement, which has been found particularly useful to increase the signal resolution in Raman[5] or infrared spectroscopy. [6] When NPs are orderly assembled on a surface, the propagation of the plasmonic signal jointly to the nanostructured modification allow to control the transmission property.[7,8] Remarkably, the incident beam direction can be control with original optical properties of these structure such as negative refraction[9,10] or superlensing effect. [11] Historically, Au has been the first material where NPs LSPR effect was investigated, selecting the aqueous colloidal absorption wavelength among the visible range.[12] More recently, Alonso-Gonzales group investigated their contribution to enhance the overall extinction signal in the infrared range[13], where the Au NPs improvements was suggested to scale with the local near field value.[14] The latter was found to be also effective to enhance the incoming light absorption in photovoltaics or detector surface[15], as it will discuss further on. Finally, among the large variety of growing materials, Ag and Al have demonstrated outstanding performance and versatility in different areas such as photovoltaics[16], drug delivery[17,18] ,(bio)sensing[19,20] , disinfection[21] and catalysis.[22,23] However, better performance and novel applications has been investigated using unconventional plasmonic material such as gallium as we will further discuss.

# 1.2 Synthesis of metal NPs

In order to find suitable materials for the right application, a large number of metals with plasmonic behaviours have been investigated. Their fabrication involved the use of a variety of techniques to obtain shape tunability and high yield. Most common physical and chemical processes to grow NPs are: electron beam evaporation, laser ablation, thermal evaporation, molecular beam epitaxy and colloidal synthesis. The main fabrication challenge regards the optimization of the synthesis parameters such as pressure and temperature to obtain the appropriate thermodynamic conditions that enables the

nucleation process. With respect to physical deposition methods such as electron beam or thermal evaporation, the fabrication will strongly depends on the substrate interface wettability (Figure 1). Thus, the contact angle of the growing structure needs to be as high as possible, in order to form isolated structures and minimize the risk of interparticles coalescence.[24] These methods usually allow lower shape and dimension tunability compared to the chemical but large area and high yield growth are achieved.

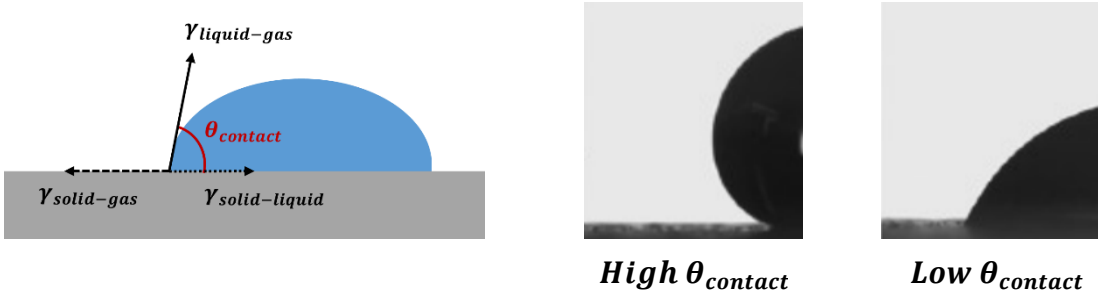


Figure 1: The angle between the Υ tensor at the solid-liquid and the liquid-gas interface defines the $\boldsymbol{\theta_{contact}}$ between the NP and the surface.

However, controlling the wetting properties of the materials can be challenging through the growth conditions. In particular, the temperature becomes a critical parameter during the chemical synthesis, where chemical precursors need to react commonly in an aqueous solution. Since Turkevich's work for the Au NPs synthesis in aqueous solution at boiling temperature,[25] metal salts reductions become a popular bottom-up modus operandi for producing metal NPs phase.[26,27,28] Using this method, NPs with a narrow diameter distribution between 60 and 2 nm can be achieved.[29] After the synthesis, further addition of colloidal stabilizers is needed in order to avoid the colloidal agglomeration. Nevertheless, NPs shape can be tuned among a plenty of structure types such as nanorods[30,31], nanoshell[32,33] , nanocage[34,35] and many others.[36,37] A more accurate discussion on the colloidal synthesis processes will be considered in Chapter 2.

# 1.3 NPs applications for innovative optoelectronic devices

High-performance optical detectors have been highly demanded for cutting edge applications in the market. New materials and technological solutions are continuously investigated. The use of semiconductor compounds has led to obtain high photo-conversion yield and spectral selectivity.[38] Nevertheless, the design and simulations of new structures have played a crucial role in the fabrication of a reliable, high-endurance and efficient light detector. A key step to optimize device performance is the processing of device surface to minimize optical losses. This surface processing commonly takes place as one of the last steps of the device fabrication layout. Lately, the NPs have been largely used to this scope, since they can help the incident light to reach the active area by different approaches:

- *1) Enhancing incoupling of light (Light scattering)*

  The presence of a metal NP can scatter the incoming light with high directionality towards the device. The light wavelength and the size of the NP need to match the Rayleigh or Mie conditions, where the NP diameter will decide the driving effect (scattering, focusing and trapping).[39,40,41] The scattered light path trajectory usually will increase leading to higher absorption probability into the active area. This long-distance effect can occur for a wide spectral range and strongly depends on the nanoparticle surface density.

- *2) Local filed enhancement (Light concentration)*

  The NP can literally act as a nanoantenna for the incoming electromagnetic radiation, transforming it into a SP excitation.[42,43,44 , 45] The absorption enhances because of the strong near-field amplitude due to the plasmonic effect. This method is particularly useful if the NP are directly in contact with the active area

and requires that the impinging light properties (wavelength, polarization, incidence angle) satisfy the resonance condition.

- *3) Changing surface refractive index ($n_{eff}$)*

  Considering the effective medium approach based on the Maxwell-Garnet theory (see Chapter 2), the NPs on a surface can be treated as an equivalent homogenous layer. The effective refractive index ($n_{eff}$) will depend on the NPs surface coverage, their material composition and their shape. Easier coupling of the incident light will be possible by lowering the reflection component.

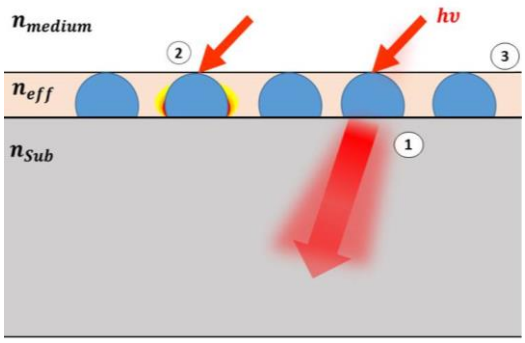


Figure2: Sketch of the three possible light/matter interactions during the device modified sensor surface

Historically, Fraunhofer first investigated the antireflective effect of roughed surface during his experiment. [46] Later, it was discovered that nature systems also take advantage by nanostructuring surface to reduce the reflected incoming light like in moth eye corneal. [47, 48] Depending on the pattern structure geometry, it will possible to grade the refractive index value of the layer for a better incoming light coupling with the substrate compared to conventional multilayer ARC. [49] Additionally, the nanostructured surface allows easier light trapping [50, 41] into the substrate, due to strong forward (F) and low back (B) scattering. [51, 52] As simulations demonstrated, the F scattered light can be optimized depending on the NP shape and high values of the F/B ratio have been experimentally confirmed either with metal or semiconductor NP materials, with remarkable

enhancements in terms of the device light conversion performance. [53, 54, 55] The Catchpole and Polman simulation study based on Ag NPs on Si substrates demonstrated that almost a 30 fold light scattering enhancement can be obtained using a 100 nm hemisphere structure.

Remarkable results have been also achieved in the solar cell field. Thermally evaporated 40 nm diameter Ag NPs on an amorphous silicon photo-device can lead to relevant enhancement of the quantum efficiency at the near IR wavelengths.[56] Also, Nakayama and his group obtained 8% increase of the short circuit current density of a GaAs solar cell by means of 100 nm Ag NPs of different shape. In this case, the NPs were made by deposition through anodic aluminum oxide patterns. Among the studied geometries, low surface density hemisphere shown best transmission property, while higher photovoltaic current was achieved for surface nanocones high density. But also common photodetectors can be improve.[57] Using plasmonic metal nanoparticles, it has been demonstrated that the incoming photon/semiconductor interaction factor – measured by the transit time per unit thickness – will be related with the lifetime of the SP wave. Typical lifetime value of a surface plasmon was attested around 5 $fs$,[58] positively contributing to the interaction probability considering the average photon path of $100nm/_{1fs}$ in that zone.[59] Furthermore, the enhanced near-field amplitude at the NP surroundings has been expected to increase the overall extinction factor due to light the light scattering and concentration approaches previously presented.

However, the tuning of the structure parameters such as permittivity, shape and dimension is not an easy task and new material and fabrication method are needed. In particularly, most of the used NP materials are able to guarantee good results in the UV or near and mid IR range. A solution is offered by thermally evaporated gallium nanoparticles (Ga NPs). Their peculiar composition and shape perfectly fit the required criteria for the developing of innovative surface modification for optical detector device.

# 1.4 Gallium nanoparticles (Ga NPs): hard shell with a liquid core

Since tunability of the surface properties are required to match different application issues, the used NPs material should theoretically cover an operational broad spectral range with reliable and stable performances. Noble and semi-noble metals, such as Au and Al, have been largely employed in the visible range but their permittivity and absorption properties have been mostly found inadequate for the UV applications.[60,61] Additionally, these types of NP are mostly synthetize via chemical method, which is great for liquid media application but can be problematic to employ for surface modification.

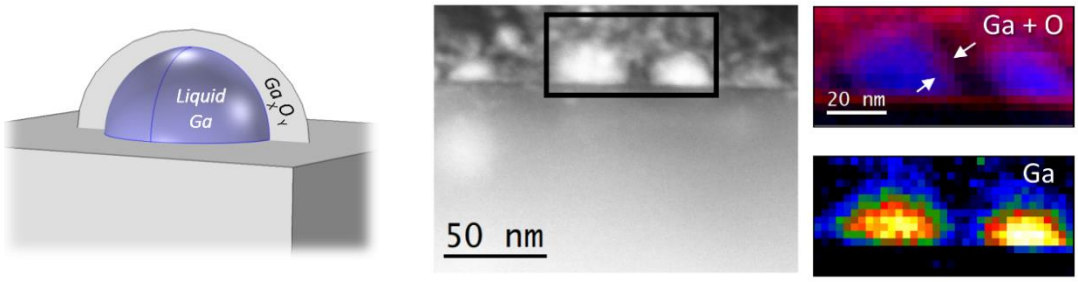


Figure 3: TEM images of Ga NPs thermally evaporated on a Si. The images also shown elemental analysis that allowed to determinate the Ga Ox shell thickness that is around 2 nm.

With this regards, Ga has been attested as an excellent candidate due to its easy synthesis and peculiar physical and structural properties.[62] In fact, when solid Ga is grown on a semiconductor or quartz surface[63,64,65], the specific thermodynamic conditions allows the creation of a hemispheric NPs. Since Ga is a low melting point material, the structure at its very first stage will be a perfectly round hemisphere of liquid Ga. Recent studies attested its plasmonic resonance tunability in a broad wavelength range between UV and near IR part of the spectra simply by changing the hemisphere dimension.[32] When the growth process is concluded, the NP surface is exposed to the atmosphere and a thin Ga

oxide (Ga Ox) layer is formed.[66,67] The shell provides chemical and structural stability at room temperature. Interestingly, it was found that the surrounding shell thickness can be varied through thermal annealing processes due to core material oxidation.[68] The tuning of the liquid/oxide rate will lead to a change of the NP permittivity value, hence a modification of the surface refractive index $n_{eff}$. Figure 3 shows TEM evidences of the core-oxide shell structure for a Ga NP growth on Si. Elemental analysis allowed to determinate a shell thickness value of around 2 nm.

The plasmonic resonance tunability and the NP material composition property make Ga NPs very attractive for surface modification[69], ellipsometry-based biosensors[70] or surface-enhanced Raman spectroscopy (SERS).[71] Nevertheless, Ga NPs can be also synthetize as colloidal to be used in the energy storage field or as optimal drug delivery for tumours especially in acidic environment.[67,72]

# 1.5 Goals and thesis structure

This work aims to investigate the use of Ga NPs for optical detector surface modification. As previously discussed, the peculiar core-shell structure allows high tunability of the NPs layer for optical device photo response improvements.

In Chapter 2, the proposed theoretical background provides to give the tools for a complete and exhausting understanding of the treated topics.

In Chapter 3, the used fabrication and experimental techniques for the optical, electrical and morphology investigation are presented.

In Chapter 4, a new synthetize method for colloidal Ga NPs and their optical characterization was discussed. The development of the colloidal solution has allowed further investigation of the NP optical property in different solvents. Finally, the plasmonic resonance of a single drop casted NP was studied by means of the EELS technique thanks to the collaboration with the University of Cadiz.

In Chapter 5, plasma and chemical treatments of the Ga NPs are described. After their thermal evaporation on silicon surface, the NPs were plasma etched with $O_2$ reactive ion etching (RIE) technique. Remarkably, after the process optimization, Ga nano-pyramid structure was achieved. Further simulation supported the near field enhancement due to the new structure shape. Additionally, silicon nanocolumns with Ga hemisphere cap were also obtain using different RIE gasses mix ($CHF_3/O_2$). In order to modify the Ga NPs coverage and their dimension distribution, wet etching with chloridric acid was found effective.

In Chapter 6, NPs were used to modify a InGaAs/InAlAs avalanche photodiode (APD) provided by the University of Sheffield. The photo response was improved by the use of thermally treated Ga NPs layer on a PMMA buffer layer. Previous studies of the NPs antireflective property were done in order to identify the right NPs size and treatment for the wanted spectral range. Remarkably, the modified structure achieved to maintain the same dark current signal jointly with a 30% enhancement of the light current conversion. The chapter concludes with the results of using AlN material instead of PMMA as the device passivation layer.

# References


[1] Philippe Colomban, "The Use of Metal Nanoparticles to Produce Yellow, Red and Iridescent Colour, from Bronze Age to Present Times in Lustre Pottery and Glass: Solid State Chemistry, Spectroscopy and Nanostructure", Journal of Nano Research **8**, 109 (2009).

[2] M. Reibold, N. Pätzke, A. A. Levin, W. Kochmann, I. P. Shakhverdova, P. Paufler, and D. C. Meyer, "Structure of several historic blades at nanoscale", Crystal Research and Technology **44** (10), 1139 (2009).

[3] Kwangjae Cho, Xu Wang, Shuming Nie, Zhuo Chen, and Dong M. Shin, "Therapeutic Nanoparticles for Drug Delivery in Cancer", Clinical Cancer Research **14** (5), 1310 (2008).

[4] Kaishu Guan, "Relationship between photocatalytic activity, hydrophilicity and self-cleaning effect of TiO2/SiO2 films", Surface and Coatings Technology **191** (2), 155 (2005).

[5] Hongxing Xu, Javier Aizpurua, Mikael Käll, and Peter Apell, "Electromagnetic contributions to single-molecule sensitivity in surface-enhanced Raman scattering", Physical Review E **62** (3), 4318 (2000).

[6] F. Neubrech, T. Kolb, R. Lovrincic, G. Fahsold, A. Pucci, J. Aizpurua, T. W. Cornelius, M. E. Toimil-Molares, R. Neumann, and S. Karim, "Resonances of individual metal nanowires in the infrared", Applied Physics Letters **89** (25), 253104 (2006).

[7] Christian Girard and Romain Quidant, "Near–field optical transmittance of metal particle chain waveguides", Opt. Express **12** (25), 6141 (2004).

[8] Alexandre G. Brolo, Reuven Gordon, Brian Leathem, and Karen L. Kavanagh, "Surface Plasmon Sensor Based on the Enhanced Light Transmission through Arrays of Nanoholes in Gold Films", Langmuir **20** (12), 4813 (2004).

[9] J. B. Pendry, "Negative Refraction Makes a Perfect Lens", Physical Review Letters **85** (18), 3966 (2000).

[10] Vladimir M. Shalaev, "Optical negative-index metamaterials", Nature Photonics **1**, 41 (2007).

[11] Nicholas Fang, Hyesog Lee, Cheng Sun, and Xiang Zhang, "Sub–Diffraction-Limited Optical Imaging with a Silver Superlens", Science **308** (5721), 534 (2005).

[12] M. Faraday, "Experiemntal relations of gold (and other metals) to light", Philosophical Transactions of the Royal Society of London **147** (36.) (1857).

[13] P. Alonso-González, P. Albella, M. Schnell, J. Chen, F. Huth, A. García-Etxarri, F. Casanova, F. Golmar, L. Arzubiaga, L. E. Hueso, J. Aizpurua, and R. Hillenbrand, "Resolving the electromagnetic mechanism of surface-enhanced light scattering at single hot spots", Nature Communications **3**, 684 (2012).

[14] Lauren A. Austin, Bin Kang, and Mostafa A. El-Sayed, "Probing molecular cell event dynamics at the single-cell level with targeted plasmonic gold nanoparticles: A review", Nano Today **10** (5), 542 (2015).

[15] S. Pillai and M. A. Green, "Plasmonics for photovoltaic applications", Solar Energy Materials and Solar Cells **94** (9), 1481 (2010).

[16] Peng Hui Wang, Morgan Millard, and Alexandre G. Brolo, "Optimizing Plasmonic Silicon Photovoltaics with Ag and Au Nanoparticle Mixtures", The Journal of Physical Chemistry C **118** (11), 5889 (2014).

[17] Nancy A. Monteiro-Riviere, Steven J. Oldenburg, and Alfred O. Inman, "Interactions of aluminum nanoparticles with human epidermal keratinocytes", Journal of Applied Toxicology **30** (3), 276 (2010).

[18] Lauren A. Austin, Megan A. Mackey, Erik C. Dreaden, and Mostafa A. El-Sayed, "The optical, photothermal, and facile surface chemical properties of gold and silver nanoparticles in biodiagnostics, therapy, and drug delivery", Archives of Toxicology **88** (7), 1391 (2014).

[19] Gonçalo Doria, João Conde, Bruno Veigas, Leticia Giestas, Carina Almeida, Maria Assunção, João Rosa, and Pedro V. Baptista, "Noble Metal Nanoparticles for Biosensing Applications", Sensors **12** (2), 1657 (2012).

[20] Mustafa H. Chowdhury, Krishanu Ray, Stephen K. Gray, James Pond, and Joseph R. Lakowicz, "Aluminum Nanoparticles as Substrates for Metal-Enhanced Fluorescence in the Ultraviolet for the Label-Free Detection of Biomolecules", Analytical Chemistry **81** (4), 1397 (2009).

[21] Zhihua Yuan, Yunbin Chen, Tingting Li, and Chang-Ping Yu, "Reaction of silver nanoparticles in the disinfection process", Chemosphere **93** (4), 619 (2013).

[22] Takato Mitsudome, Shusuke Arita, Haruhiko Mori, Tomoo Mizugaki, Koichiro Jitsukawa, and Kiyotomi Kaneda, "Supported Silver-Nanoparticle-Catalyzed Highly Efficient Aqueous Oxidation of Phenylsilanes to Silanols", Angewandte Chemie **120** (41), 8056 (2008).

[23] Hai-Long Jiang, Tomoki Akita, Tamao Ishida, Masatake Haruta, and Qiang Xu, "Synergistic Catalysis of Au@Ag Core−Shell Nanoparticles Stabilized on Metal−Organic Framework", Journal of the American Chemical Society **133** (5), 1304 (2011).

[24] M. José-Yacamán, C. Gutierrez-Wing, M. Miki, D. Q. Yang, K. N. Piyakis, and E. Sacher, "Surface Diffusion and Coalescence of Mobile Metal Nanoparticles", The Journal of Physical Chemistry B **109** (19), 9703 (2005).

[25] John Turkevich, Peter Cooper Stevenson, and James Hillier, "A study of the nucleation and growth processes in the synthesis of colloidal gold", Discussions of the Faraday Society **11** (0), 55 (1951).

[26] J. Kimling, M. Maier, B. Okenve, V. Kotaidis, H. Ballot, and A. Plech, "Turkevich Method for Gold Nanoparticle Synthesis Revisited", The Journal of Physical Chemistry B **110** (32), 15700 (2006).

[27] Magali Boutonnet, Jerzy Kizling, Per Stenius, and Gilbert Maire, "The preparation of monodisperse colloidal metal particles from microemulsions", Colloids and Surfaces **5** (3), 209 (1982).

[28] Alain Roucoux, Jürgen Schulz, and Henri Patin, "Reduced Transition Metal Colloids: A Novel Family of Reusable Catalysts?", Chemical Reviews **102** (10), 3757 (2002).

[29] Werner Baschong, John Lucocq, and J. Roth, *Thiocyanate gold: Small (2-3 nm) Colloidal Gold for Affinity Cytochemical Labeling in Electron Microscopy*. (1985), pp.409.

[30] Gülis Zengin, Göran Johansson, Peter Johansson, Tomasz J. Antosiewicz, Mikael Käll, and Timur Shegai, "Approaching the strong coupling limit in single plasmonic nanorods interacting with J-aggregates", Scientific Reports **3**, 3074 (2013).

[31] Huanjun Chen, Lei Shao, Qian Li, and Jianfang Wang, "Gold nanorods and their plasmonic properties", Chemical Society Reviews **42** (7), 2679 (2013).

[32] Mark W. Knight, Toon Coenen, Yang Yang, Benjamin J. M. Brenny, Maria Losurdo, April S. Brown, Henry O. Everitt, and Albert Polman, "Gallium Plasmonics: Deep Subwavelength Spectroscopic Imaging of Single and Interacting Gallium Nanoparticles", ACS Nano **9** (2), 2049 (2015).

[33] Ken-Tye Yong, Yudhisthira Sahoo, Mark T. Swihart, and Paras N. Prasad, "Synthesis and plasmonic properties of silver and gold nanoshells on polystyrene cores of different size and of gold–silver core–shell nanostructures", Colloids and Surfaces A: Physicochemical and Engineering Aspects **290** (1), 89 (2006).

[34] Xueyu Zhao, Ran Long, Dong Liu, Binbin Luo, and Yujie Xiong, "Pd–Ag alloy nanocages: integration of Ag plasmonic properties with Pd active sites for light-driven catalytic hydrogenation", Journal of Materials Chemistry A **3** (18), 9390 (2015).

[35] Jingyi Chen, Charles Glaus, Richard Laforest, Qiang Zhang, Miaoxian Yang, Michael Gidding, Michael J. Welch, and Younan Xia, "Gold Nanocages as Photothermal Transducers for Cancer Treatment", Small **6** (7), 811 (2010).

[36] Nikolai Khlebtsov and Lev Dykman, (2010), pp. 37.

[37] Xianmao Lu, Matthew Rycenga, Sara E. Skrabalak, Benjamin Wiley, and Younan Xia, "Chemical Synthesis of Novel Plasmonic Nanoparticles", Annual Review of Physical Chemistry **60** (1), 167 (2009).

[38] A. Rogalski, "Recent progress in infrared detector technologies", Infrared Physics & Technology **54** (3), 136 (2011).

[39] C.F. Bohren and D.R. Huffman, *Absorption and Scattering of Light by Small Particles*. (Wiley, 2008).

[40] Xiaofeng Fan, Weitao Zheng, and David J. Singh, "Light scattering and surface plasmons on small spherical particles", Light: Science &Amp; Applications **3**, e179 (2014).

[41] Harry A. Atwater and Albert Polman, "Plasmonics for improved photovoltaic devices", Nature Materials **9**, 205 (2010).

[42] Jon A. Schuller, Edward S. Barnard, Wenshan Cai, Young Chul Jun, Justin S. White, and Mark L. Brongersma, "Plasmonics for extreme light concentration and manipulation", Nature Materials **9**, 193 (2010).

[43] T. Kalkbrenner, M. Ramstein, J. Mlynek, and V. Sandoghdar, "A single gold particle as a probe for apertureless scanning near-field optical microscopy", Journal of Microscopy **202** (1), 72 (2001).

[44] Min-Ki Kwon, Ja-Yeon Kim, Baek-Hyun Kim, Il-Kyu Park, Chu-Young Cho, Clare Chisu Byeon, and Seong-Ju Park, "Surface-Plasmon-Enhanced Light-Emitting Diodes", Advanced Materials **20** (7), 1253 (2008).

[45] Yinan Zhang, Boyuan Cai, and Baohua Jia, "Ultraviolet Plasmonic Aluminium Nanoparticles for Highly Efficient Light Incoupling on Silicon Solar Cells", Nanomaterials **6** (6), 95 (2016).

[46] Hemant Kumar Raut, V. Anand Ganesh, A. Sreekumaran Nair, and Seeram Ramakrishna, "Anti-reflective coatings: A critical, in-depth review", Energy & Environmental Science **4** (10), 3779 (2011).

[47] C. Bernhard, "Structural and functional adaptation in a visual system", Endeavour **26** (79) (1967).

[48] P. B. Clapham and M. C. Hutley, "Reduction of Lens Reflexion by the “Moth Eye” Principle", Nature **244** (5414), 281 (1973).

[49] Mehdi Keshavarz Hedayati and Mady Elbahri, "Antireflective Coatings: Conventional Stacking Layers and Ultrathin Plasmonic Metasurfaces, A Mini-Review", Materials **9** (6), 497 (2016).

[50] K. V. Baryshnikova, M. I. Petrov, V. E. Babicheva, and P. A. Belov, "Plasmonic and silicon spherical nanoparticle antireflective coatings", Scientific Reports **6**, 22136 (2016).

[51] Steven Person, Manish Jain, Zachary Lapin, Juan Jose Sáenz, Gary Wicks, and Lukas Novotny, "Demonstration of Zero Optical Backscattering from Single Nanoparticles", Nano Letters **13** (4), 1806 (2013).

[52] Yuan Hsing Fu, Arseniy I. Kuznetsov, Andrey E. Miroshnichenko, Ye Feng Yu, and Boris Luk'yanchuk, "Directional visible light scattering by silicon nanoparticles", Nature Communications **4**, 1527 (2013).

[53] S. Pillai, K. R. Catchpole, T. Trupke, and M. A. Green, "Surface plasmon enhanced silicon solar cells", Journal of Applied Physics **101** (9), 093105 (2007).

[54] Se-Woong Baek, Jonghyeon Noh, Chun-Ho Lee, BongSoo Kim, Min-Kyo Seo, and Jung-Yong Lee, "Plasmonic Forward Scattering Effect in Organic Solar Cells: A Powerful Optical Engineering Method", Scientific Reports **3**, 1726 (2013).

[55] P. Matheu, S. H. Lim, D. Derkacs, C. McPheeters, and E. T. Yu, "Metal and dielectric nanoparticle scattering for improved optical absorption in photovoltaic devices", Applied Physics Letters **93** (11), 113108 (2008).

[56] Etienne Moulin, Peiqing Luo, Bart Pieters, Joachim Sukmanowski, Joachim Kirchhoff, Wilfried Reetz, Thomas Müller, Reinhard Carius, Francois-Xavier Royer, and Helmut Stiebig, "Photoresponse enhancement in the near infrared wavelength range of ultrathin amorphous silicon photosensitive devices by integration of silver nanoparticles", Applied Physics Letters **95** (3), 033505 (2009).

[57] Howard R. Stuart and Dennis G. Hall, "Island size effects in nanoparticle-enhanced photodetectors", Applied Physics Letters **73** (26), 3815 (1998).

[58] F. Stietz, J. Bosbach, T. Wenzel, T. Vartanyan, A. Goldmann, and F. Träger, "Decay Times of Surface Plasmon Excitation in Metal Nanoparticles by Persistent Spectral Hole Burning", Physical Review Letters **84** (24), 5644 (2000).

[59] D. M. Schaadt, B. Feng, and E. T. Yu, "Enhanced semiconductor optical absorption via surface plasmon excitation in metal nanoparticles", Applied Physics Letters **86** (6), 063106 (2005).

[60] Christoph Langhammer, Markus Schwind, Bengt Kasemo, and Igor Zorić, "Localized Surface Plasmon Resonances in Aluminum Nanodisks", Nano Letters **8** (5), 1461 (2008).

[61] Xiaohua Huang and Mostafa A. El-Sayed, "Gold nanoparticles: Optical properties and implementations in cancer diagnosis and photothermal therapy", Journal of Advanced Research **1** (1), 13 (2010).

[62] J. M. Sanz, D. Ortiz, R. Alcaraz de la Osa, J. M. Saiz, F. González, A. S. Brown, M. Losurdo, H. O. Everitt, and F. Moreno, "UV Plasmonic Behavior of Various Metal Nanoparticles in the Near- and Far-Field Regimes: Geometry and Substrate Effects", The Journal of Physical Chemistry C **117** (38), 19606 (2013).

[63] M. F. Meléndrez, G. Cárdenas, and J. Arbiol, "Synthesis and characterization of gallium colloidal nanoparticles", Journal of Colloid and Interface Science **346** (2), 279 (2010).

[64] Pae C. Wu, Christopher G. Khoury, Tong-Ho Kim, Yang Yang, Maria Losurdo, Giuseppe V. Bianco, Tuan Vo-Dinh, April S. Brown, and Henry O. Everitt, "Demonstration of Surface-Enhanced Raman Scattering by Tunable, Plasmonic Gallium Nanoparticles", Journal of the American Chemical Society **131** (34), 12032 (2009).

[65] Paolo Ghigna, Giorgio Spinolo, Giovanni Battista Parravicini, Angiolino Stella, Andrea Migliori, and Richard Kofman, "Metallic versus Covalent Bonding: Ga Nanoparticles as a Case Study", Journal of the American Chemical Society **129** (25), 8026 (2007).

[66] M. J. Regan, H. Tostmann, P. S. Pershan, O. M. Magnussen, E. DiMasi, B. M. Ocko, and M. Deutsch, "X-ray study of the oxidation of liquid-gallium surfaces", Physical Review B **55** (16), 10786 (1997).

[67] Maksym Yarema, Michael Wörle, Marta D. Rossell, Rolf Erni, Riccarda Caputo, Loredana Protesescu, Kostiantyn V. Kravchyk, Dmitry N. Dirin, Karla Lienau, Fabian von Rohr, Andreas Schilling, Maarten Nachtegaal, and Maksym V. Kovalenko, "Monodisperse

Colloidal Gallium Nanoparticles: Synthesis, Low Temperature Crystallization, Surface Plasmon Resonance and Li-Ion Storage", Journal of the American Chemical Society **136** (35), 12422 (2014).

[68] S. Catalán-Gómez, A. Redondo-Cubero, F. J. Palomares, F. Nucciarelli, and J. L. Pau, "Tunable plasmonic resonance of gallium nanoparticles by thermal oxidation at low temperatures", Nanotechnology **28** (40), 405705 (2017).

[69] H.C. Hulst and H.C. van de Hulst, *Light Scattering by Small Particles*. (Dover Publications, 1981).

[70] T. García-Mendiola A. García Marín, C. N. Bernabeu, M. J. Hernández, J. Piqueras, J. L. Pau, F. Pariente, E. Lorenzo, "Gallium plasmonic nanoparticles for label-free DNA and single nucleotide polymorphism sensing", Nanoscale **8**, 9842 (2016).

[71] Yang Yang, John M. Callahan, Tong-Ho Kim, April S. Brown, and Henry O. Everitt, "Ultraviolet Nanoplasmonics: A Demonstration of Surface-Enhanced Raman Spectroscopy, Fluorescence, and Photodegradation Using Gallium Nanoparticles", Nano Letters **13** (6), 2837 (2013).

[72] Yue Lu, Quanyin Hu, Yiliang Lin, Dennis B. Pacardo, Chao Wang, Wujin Sun, Frances S. Ligler, Michael D. Dickey, and Zhen Gu, "Transformable liquid-metal nanomedicine", Nature Communications **6**, 10066 (2015).

# Chapter 2
# Background

## 2.1 Plasmonics

When light interacts with matter, scattering and absorption phenomena occur, both of which contribute to the alteration of the impinging electromagnetic wave. During the scattering event, the light beam can change its wave vector direction (elastic scattering) or even modify the radiation wavelength, hence the energy. Generally, the scattering and absorption events occur due to the non-uniform nature of the medium at the so called scatter center. Since the entity of the phenomena will depend on the center concentration and dimension, it is common to use the absorption ($C_{abs}$) and scattering ($C_{sca}$) total cross section factor in the medium as follows[1]:

$$C_{ext} = C_{sca} + C_{abs} \quad (1)$$

$$C_{sca} = \frac{k^4 \alpha^2}{6\pi} \quad (2)$$

$$C_{abs} = Im[\alpha]k \quad (3)$$

Where $k$ is the wave vector and $\alpha$ is the polarizability factor. The extinction cross section ($C_{ext}$) will be the sum of the scattering and absorption factors. Thus, when the energy of an incoming photon is taken up from the matter, the loss energy during the exchange can be detected. Depending on the losing energy level, the absorption event can be label in plenty of different way. In the case of collective oscillation of free electron between a positive and negative dielectric constant materials, the related signal will be called plasmonic absorption. According to the material plasma frequency theory [2], charge

density in a metal oscillates at a fix frequency called plasma frequency ($\omega_P$), which is characteristic of each material due to structural parameters. This frequency had been found related to the energy loss radiation during the collision of a photon with a thin metal layer as follows:

$$\omega = \frac{\omega_P}{\sqrt{2}} \qquad (4)$$

Evidence of this phenomena were firstly attested by Sir Ritchie in the early 1957, who referred to it as Surface Plasmon (SP). The electrons plasma oscillation direction depends on the incoming light polarization vector respect to the normal of the surface, which can be *s* (transversal) or *p* (perpendicular) polarized. However, it is not trivial to excite the SP in a material due to difficulties in momentum and energy transfer from the incident free wave. Solving the Maxwell equations at the interest material interface, SP conditions can be found:

Table 1: Wave vectors formulation extrapolated by the Maxwell equation of the 2D boundary conditions

| 2D Boundary Conditions | Obtained equations | Wave vectors formulation |
|---|---|---|
| $E_{x\,Me} = E_{x\,Die}$ | $\frac{\kappa_{z\,Me}}{\kappa_{z\,Die}} = -\frac{\varepsilon_{Me}}{\varepsilon_{Die}}$ | $\kappa_x^2 = \frac{\omega^2}{c^2}\frac{\varepsilon_{Me}\varepsilon_{Die}}{\varepsilon_{Me}+\varepsilon_{Die}}$ |
| $H_{y\,Me} = H_{y\,Die}$ | | |
| $\kappa_{x\,Me} = \kappa_{x\,Die}$ | $\kappa_x^2 + \kappa_{z\,Die}^2 = \varepsilon_{Die}\frac{\omega^2}{c^2}$ | $\kappa_{z\,Die}^2 = \frac{\omega^2}{c^2}\frac{{\varepsilon_{Die}}^2}{\varepsilon_{Me}+\varepsilon_{Die}}$ |
| $\kappa_y = 0;\ \ \kappa^2 = \varepsilon\frac{\omega^2}{c^2}$ | | |
| ${\kappa_x}^2 + {\kappa_y}^2 + {\kappa_z}^2 = \kappa$ | $\kappa_x^2 + \kappa_{z\,Me}^2 = \varepsilon_{Me}\frac{\omega^2}{c^2}$ | $\kappa_{z\,Me}^2 = \frac{\omega^2}{c^2}\frac{{\varepsilon_{Me}}^2}{\varepsilon_{Me}+\varepsilon_{Die}}$ |

Since the wave has to propagate at the material interface, the $k_x$ wave vector has to be real to avoid amplitude decays along the propagating direction while $k_z$ has to be

imaginary. This condition can be achieved for a permittivity with Re($\varepsilon_{Me}$) < 0 and $|\varepsilon_{Me}|$ >$|\varepsilon_{Die}|$. According to Drude free electron model in a metal, permittivity can be expressed as follows:

$$\varepsilon(\omega) = 1 - \frac{\omega_P^2}{\omega^2} \qquad (5)$$

for high value of the wave vector, the SP frequency will be expressed as:

$$\omega_{SP} = \frac{\omega_P}{\sqrt{1+\varepsilon_{Die}}} \qquad (6)$$

Since boundary conditions lead to the equality $\varepsilon_{Me}$= - $\varepsilon_{Die}$, if the considered dielectric is air ($\varepsilon_{Air}$=1), Eq. (4) is obtained. Interestingly, in the case that metal material shows no loss (Im ($\varepsilon_{Me}$)=0), the calculated group velocity will be equal to zero, denoting a electrostatic nature of the phenomena. However, real metals always show some loss depending on the incoming light wavelength and the traveling SPP will be attenuated with common propagation length between 10 and 100 um in the visible spectra range. [3]

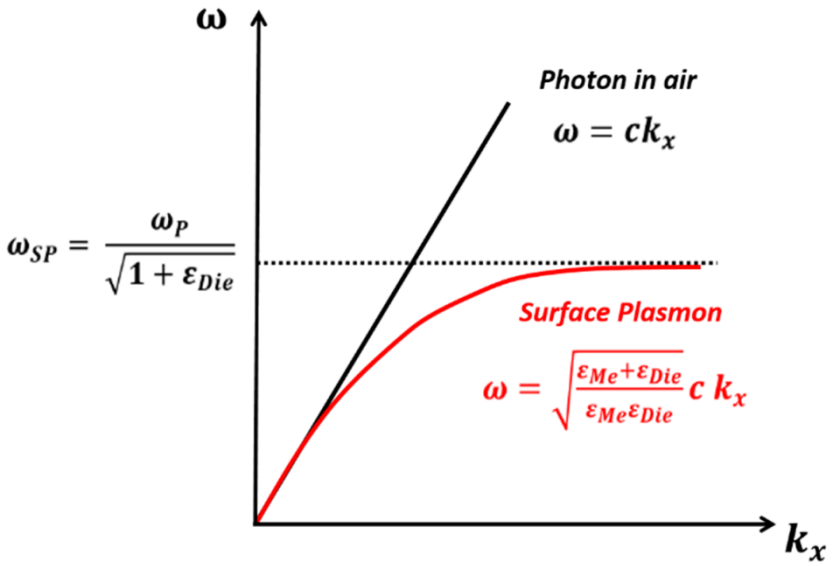


Figure 1: Plasmon resonance condition compared to the angular frequency of a photon in air.

Figure 1 graphically shows the plasmon condition compared to the frequency of a photon in air (solid black curve). The SP curve always has larger value than the one of the photon, although the curve seem to overlap at low wave vector values. Thus, the excitation of SP at the shallow metal/dielectric interface is practically impossible by direct illumination. Surface grating or roughness can provide the right coupling thanks to Umklapp processes strategies. [4] Others techniques based on attenuated total reflection method were also developed. [5] The main advantage of using the plasmonic effect lays on its effectivity to concentrate the radiation into subwavelength structures depending on their permittivity. Enclosing light in such a small region allows strong near-field enhancement at the metal/dielectric interface because of non-linear phenomena.

But SP has been also detected in 3D confined surface such as nanoparticles or holes array of different shapes. In this case, the localized surface plasmon resonance (LSPR) is a non-propagating wave confined at the metal/medium interface. When photons with the required energy and polarization imping on the nanostructure, the LSPR manifests itself. Considering a sphere nanoparticle of a radius $a$ smaller than the light wavelength, the polarization vector $\vec{P}$ can be obtained by the Laplace equation solution under the boundary conditions of tangential and normal component equality:

$$\vec{P} = \varepsilon_0 \varepsilon_{medium} \alpha \overrightarrow{E_0} \qquad (7)$$

$$\alpha = 4\pi a^3 \left( \frac{\varepsilon_{Me} - \varepsilon_{medium}}{\varepsilon_{Me} + 2\varepsilon_{medium}} \right) \qquad (8)$$

where $\overrightarrow{E_0}$ is the electric field vector along the propagating direction. The interaction between the structure and an electromagnetic wave will generate a dipole moment. Generally, plasmonic absorption in a NP can be represented as a monopole electromagnetic source (single resonance) or a multipoles electromagnetic source (multi-peak resonance) depending of the structure size and dimension. The resonance is frequency dependent and it corresponds to the maximum value of the $\alpha$ that occurs if

$Re(\varepsilon) = -2\,\varepsilon_{Me}$ (Fröhlich condition). Thus, a change of the nanostructure material will vary the resonance peak position, while a change in shape could be even generate new plasmonic mode due to different $\alpha$ factor across the NP. Each peak will be related with the electron plasma oscillation along the structure symmetry axis. Considering a hemisphere nanoparticles for instead, a transversal and longitudinal modes could be excited depending on the impinging wave polarization.

Nevertheless, the plasma Drude model contemplates the vibrational mode attenuation due to collisions between electron-electron, electron-phonon or electron-defect. For a bulk material, the impacts rate is considered constant, hence the permittivity will not depends on it. As the considered volume size reduces, collision rate increases relating the permittivity and the plasmonic resonance to the NP size. Additionally, the scattering and absorption cross section also will depends on the structure dimension, scaling with proportional and quadratic trend respectively to the volume.[6]

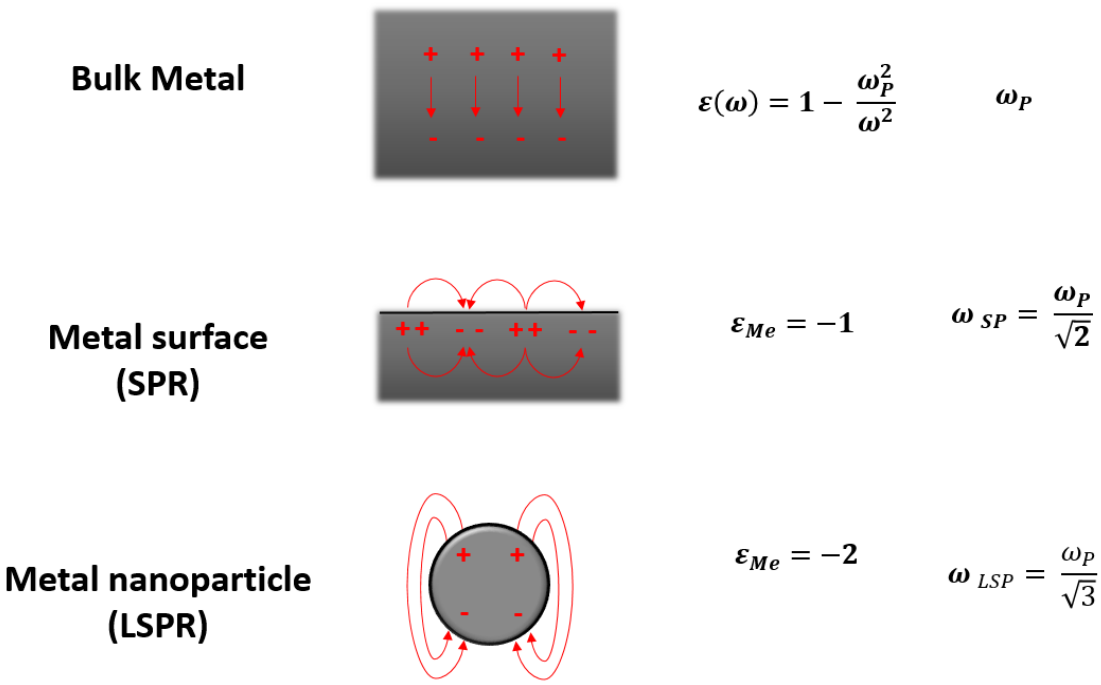


Figure 2: SPR and LSPR permittivity and resonance conditions compared to the Drude bulk metal equations

# 2.2 Colloidal NPs

Even before that plasmonic phenomena became clear to science community, it was the uncharted reason of interesting colloidal field issues about the interaction between light and matter. Dispersing NPs in a solution gives the advantage to study their optical property and additionally their easy application on a surface by means of drop casting technique.

## 2.2.1 Synthesis and scope overview

The term colloidal originates from the ancient Greek word “kolla” that means glue. The modern concept of a colloidal solution was credited to the British chemist Thomas Graham (1861) that referred to it for a heterogeneous mixture where particles were suspended in a medium (e.g. smoke, aerogel, Bolognese sauce). The first in study the light scattering property of Au colloidal NPs was Lord Faraday in 1857.[7] Unfortunately its study did not have any particular resonance at that time and only the later works of Professor Zsigmondy were brought the topic to attention of the global science community. He developed an innovative protocol of synthesis (seed-mediated method) jointly to accurate studies of the colloidal chemical-physical properties, for which was assigned him the Nobel Prize in 1925. At the same time, Theodor Svdeberg found a way to divide and to know the exact colloidal dimension by means of an ultracentrifuge equipment, while Mie was concluding his theory to explain the different NP size light scattering and absorption contributions. Remarkably, liquid crystal material were also discovered by Zocher and Langmuir within the frame of the colloidal study matter. These and others more investigations helped to developed metallic and oxide nanoparticles mixture that have been used in a plenty of applications such as chemical and biological sensing[8,9], catalysis[10], drug delivery[11] or light surface scatter. [12]

The colloidal synthesis have been developed in a variety of processes depending of the NP material, shape and dispersed medium. Generally, to obtain a large yield and controlled synthesis, two possible approach are possible: top-down and bottom-up (Figure 3). The first is based on the idea of breaking down a bulk material to smaller parts until the desired properties and dimension are obtained. Here some of the most common used top-down methods:

- Laser ablation
- Machining
- Ball milling

Compared to others methods, these approaches are cheaper and easier but usually do not allow a complete tuning of the size distribution. Thus, the top-down process are mostly destructive and they can cause material structural modification due to local crystal damage, punctual defects or chemical modifications. These changes may lead to surface alteration affecting the ultimate nanomaterials properties.

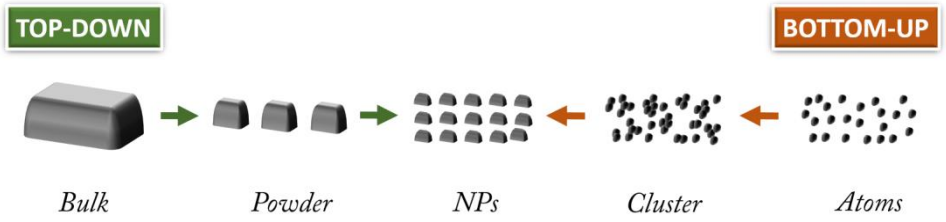


Figure 3: Methods to avoid colloids agglomeration phenomena

Regard to bottom-up processes, the concept is to use atoms or molecules as possible building block to form the desired nanostructure. These methods allow high tunability of the process and they are mostly non-destructive. Contrary to the top-down approach, there are higher chances to obtain defects-free surface and homogeneous size distribution. Common processes involved are:

- Vapor phase deposition

- Sol-gel
- Chemical reductions

Table 2 presents some of common methods to synthetize Ga and other material colloidal NPs compared to their related advantages and disadvantages.

Table 2: Colloidal common synthesis methods

| Fabrication processes | Advantages | Disadvantages |
|---|---|---|
| *Ball milling* | 5 nm < NPs diameter < 20 nm<br>0.1 h < Operating time < 20 h<br>Large scale production<br>Standard pressure and Temperature<br>Solvent selectivity<br>Green process | NOT for all materials<br>NO NPs shape selectivity<br>Possible contamination |
| *Biological (organic bacteria)* | 1 nm < NPs diameter < 200 nm | NOT for Large scale production<br>NOT for all materials<br>NO NPs shape selectivity<br>NO NPs dimension selectivity<br>NO solvent selectivity |
| *Chemical Liquid Deposition (CLD)* | 9 nm < NPs diameter < 14 nm<br>Solvent selectivity<br>Spheroid shape | Needs liquid N2<br>NOT for Large scale production<br>Complicated |
| *Laser ablation* | 8 nm < NPs diameter < 200 nm<br>1 h ≥Operating time<br>Solvent selectivity<br>Spheroid shape | NOT for Large scale production<br>(NPs size Vs Laser power issue) |
| *Ultra-sonication* | 10 nm < NPs diameter < 250 nm<br>2 h ≤ Operating time<br>Spheroid shape | NOT for Large scale production<br>Long process time<br>Large NPs size distribution |
| *Chemical synthetized* | 3 nm < NPs diameter < 100 nm<br>12 h < Operating time < 6 days<br>Shape selectivity<br>Dimension selectivity | Large scale production problem<br>(30% < reaction yield < 70% )<br>NO solvent selectivity<br>Chemical additive contaminations |

## 2.2.2 Stabilization methods

Generally, colloidal solutions can be stabilized by steric shielding between the particles or by electrostatically screening repulsion (Figure 4). Because of the ease implementation, the first method is largely used for aqueous colloidal synthesis. Usually, the used stabilizing agents are chemical surfactants[13, 14] or polymer chains[15, 16] that leads to a more stable phase of the colloidal solution. The NPs will not interact because of the steric obstacle on their surface. Common problems in the use of surfactants are related to the poor stability of those at high temperatures (typically > 70 °C) and possible undesired chemical contamination of the solution. About the electrostatic stabilization method, the ion concentration charge in the solution (e.g. change of pH level or different solvents) can increase the inter-particles repulsive force with no remarkable problems about the residues. In the next sections, we will discuss the optical characterization results of electrostatically repulsed stabilized Ga NP colloids for three different solvents: THF, DIW and EtOH. The NPs agglomeration status will mostly differ because of the solvent nature, which has intrinsic physico-chemical properties such colloidal/solvent wettability or its specific ionic strength.

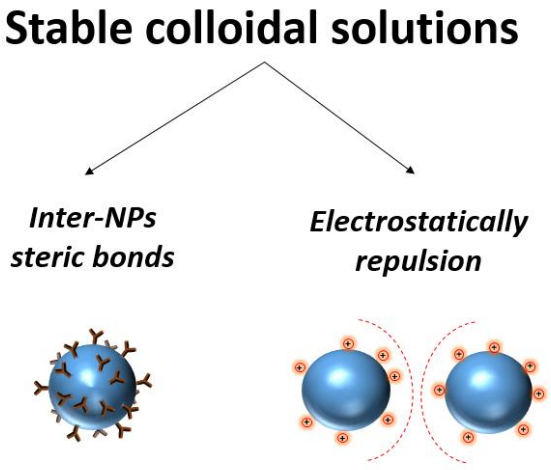


Figure 4: Methods to avoid colloids agglomeration phenomena

In order to understand and possibly to control the NPs agglomeration phenomena in a dispersed solution, the interface between the NP and the liquid needs to be fully characterize. Contrary to the solid/solid abrupt surfaces bounding, the solid/liquid material interface will be composed by several transition regions where the free ions spatial arrangement differs from the extended liquid phase (Figure 5.a). Since the NP surface is supposed to be natural positively or negatively charged, a balancing counter charge is needed. The surrounding volume with the interacting ions is called diffuse double layer (DDL). Thus, in the region between the surface and the counter charge (Helmholtz layer), the surface charge potential (ϕ) will decay linearly with the distance until its amplitude fall to the so-called zeta potential value (ζ). However, according to the Gouy-Chapman theory not all the potential can be screened by surface contact ions [17], since they could possibly detached and diffuse in the liquid cyclically . The ϕ will be influenced from the kinetic energy of the ions along the whole DDL (Figure 5.b). The size of this DDL strongly depends on the ions concentration and their valence and it can be analytically calculated by solving the Poisson equation considering a Boltzman distribution.

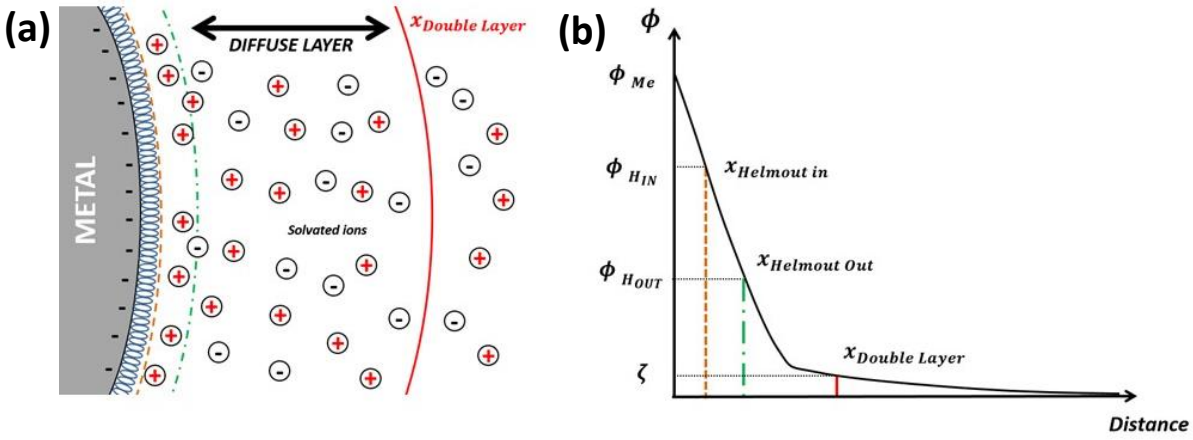


Figure 5: Sketch of the Helmholtz and diffuse layers physical position around a dispersed NP with the schematic plot of the related potential value. The distance from the NP surface that correspond to the ζ value is also called Debye length, which is the reverse of the Debye-Huckel constant $\kappa$.

Thus, the colloidal NPs surface charge can be estimated by means of dynamic light scattering technique measuring the specific ζ.[18] The latter calculates the electrokinetic potential at the Ga NP surface in the liquid medium. It can give a picture of the colloidal potential stability, where a large positive or negative value will indicate a strong mutual repulsion tendency between the dispersed NPs. The closer the |ζ|value to zero, the more the NPs aggregate due to lower surrounding ions screening effect. It common to consider a threshold ζ value of ± 30 mV to define a stable colloidal solution. Factors that can affect the colloidal stability may regards the NP charge and wettability as the liquid viscosity or ionic strength.

# 2.3 Maxwell-Garnett theory

Since NPs can be applied or directly evaporated on a material, it will be useful to predict the modified surface properties depending on the considered NP material, shape and distribution. For this purpose, the educationist Maxwell Garnett (MG) developed his theory in 1904 to calculate the effective permittivity value of a complex system made by embedded inclusions in a medium. Because of charges dipoles and multipoles presence in the inhomogeneous material, the total system induced dipole moment will be related with permittivity and the $E$ field. The analytical solution can be found considering the case of a sphere NP with $\varepsilon_{NP}$ surrounded by a no absorbing medium with $\varepsilon_{med}$ (Figure 6) for which the related extinction is calculated using Eq. (9):

$$C_{ext} = 4\pi\, Re\left[\frac{S(0)}{\kappa^2}\right] \qquad (9)$$

where S(0) is the forward direction scattering amplitude and $\kappa$ is the wave vector in the considered medium:

$$\kappa = \frac{2\pi}{\lambda} \qquad (10)$$

Since the scattering amplitude can be expressed as the follow[19]:

$$S(0) = \frac{1}{2}\sum_{n=1}^{\infty}(2n+1)(\alpha_n + \beta_n) \qquad (11)$$

where $\alpha$ and $\beta$ are complicated functions of the Bessel differential equations. The series can be further expanded concerning ($\kappa b$):

$$S(0) = i(\kappa b)^3 \frac{(\varepsilon_{med}-\varepsilon_{MG})(\varepsilon_{NP}-2\varepsilon_{med})+f(2\varepsilon_{med}+\varepsilon_{MG})(\varepsilon_{NP}-\varepsilon_{med})}{(\varepsilon_{med}+2\varepsilon_{MG})(\varepsilon_{NP}+2\varepsilon_{med})+f(2\varepsilon_{med}-\varepsilon_{MG})(\varepsilon_{NP}-\varepsilon_{med})} + \mathcal{O}[(\kappa b)^5] \qquad (12)$$

$$f = (a/b)^3 \qquad (13)$$

Finally, according to the proposed definition of the extinction factor, the MG solution can be found putting S(0)=0 finding:

$$\varepsilon_{MG} = \varepsilon_{med}\frac{\varepsilon_{NP}+2\varepsilon_{med}+2f(\varepsilon_{NP}-\varepsilon_{med})}{\varepsilon_{NP}+2\varepsilon_{med}-f(\varepsilon_{NP}-\varepsilon_{med})} \qquad (14)$$

This expression allows to calculate effective permittivity value for a colloidal solution but can be easily apply to the study of the optical behavior of NP surface modified material (chapter 6).

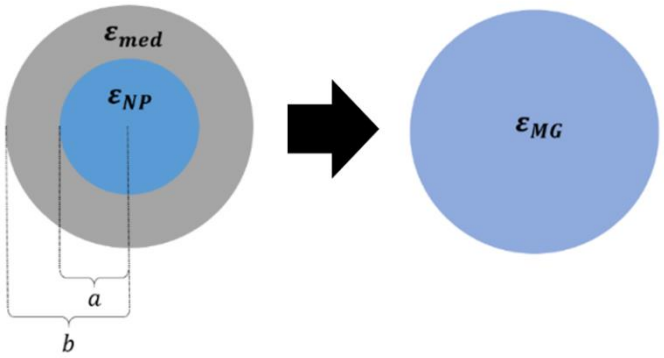


Figure 6: Considering a heterogeneous media with embedded inclusions with $\varepsilon_{med}$ and $\varepsilon_{NP}$ respectively, the effective permittivity of the two-phase system can be calculated according to Maxwell Garnett theory

# 2.4 Avalanche photodiodes (APD) basics

A photodetector is a device that convert optical to electrical signal also referred as photocurrent. Usually, the conversion process is made by three fundamental steps: absorption of the incident light with generation of carriers, their transportation across the device by means of an applied electric field and carriers gathering to provide the photo current to an external circuit. Usually, the performances required to a detector device are bandwidth selectivity, low noise, high sensitivity, high reliability and low cost.

The most studied and developed types of photodetectors are the pin diodes, photoconductors, and APD. The first only converts the light to an electric signal with usually large bandwidths, while the other two structures have internal gain (higher sensitivity). Since devices are made by III-V semiconductor materials, they can also classified as extrinsic or intrinsic type. The first can detects light of energy smaller than the material bandgap energy due to the presence of defect, impurities or quantum well inside the device. The intrinsic one absorbs light signal with similar energy to the absorption layer bandgap creating carriers that will contribute to the photocurrent.

This work has been developed within the frame of an interdisciplinary European project called PROMIS (Postgraduate Research on Dilute Metamorphic Nanostructures and Metamaterials in Semiconductor Photonics). The program were divided in four work package (WP):

- WP1: Material for ICT
- WP2: Materials for Security
- WP3: Materials for Energy
- WP4: Materials for Environment

The close collaboration between the fellows institutions made easier the control of all the fabrication, characterization and modification steps involved. This thesis belonged to the WP2, where the main developed detectors (University of Sheffield) were APDs and by

means of Ga NPs surface modification a better light conversion signal performance was achieved.

The APD structure has been suited for applications where a low number of incoming photons needs to be detected. It would be desirable a high sensitivity with large optical gain. This device are made by a p-n junction with a reverse bias equal to the device breakdown voltage. At this condition, photo-generated carries have enough energy to generate new carriers by random ionizing collisions with the material lattice, also known as impact ionization process. The ionization process occurs in the high field depletion region, where the carrier impact energy is greater than the material bandgap value. The threshold ionization energy is equal to the lost energy during the primary carrier collision. However, it is not only a matter of energy, since the material inclination to let a carriers flow and collide through the electric field direction is also important. The carrier has to have enough free path into the material to get energy but not too much in order to maximize the number of impacts during the multiplication process. This can be expressed with the use of ionization coefficients $\alpha_e$ and $\alpha_h$ that are the reciprocal of the average travelled distance of an electron ($e$) and hole ($h$) respectively. In the case of a device multiplication region width of $W$, the product between this and $\alpha$ will be the probability of the ionizing collision event. The multiplication strictly depends on the ionizing probability and the device structure and material. The random multiplication factor for $e$ and $h$ can be calculated as follows:

$$M_e = \frac{1}{1 - \int_0^W \alpha_h \exp\left[\int_0^x (\alpha_h - \alpha_e) dx'\right] dx} \qquad (15)$$

$$M_h = M_e exp\left[\int_0^x (\alpha_h - \alpha_e) dx'\right] \qquad (16)$$

Breakdown condition is when $M_e \to \infty$ or:

$$\int_0^W \alpha_h exp\left[\int_0^x (\alpha_h - \alpha_e)dx'\right]dx = 1 \qquad (17)$$

In the case of holes avalanche process:

$$\int_0^W \alpha_e exp\left[\int_0^x (\alpha_e - \alpha_h)dx'\right]dx = 1 \qquad (18)$$

But the main limitation factor of the theoretical gain of an APD device is due to noise factors associated to unwanted current sources (primary, multiplied bulk signal, dark and background currents). However, main noise source is given by the avalanche process its self. The excess noise factor for $e$ and $h$ can be expressed as:

$$F_e = M_e\left\{1 - (1 - k_r)\left[\frac{(M_e - 1)}{M_e}\right]^2\right\} \qquad (19)$$

$$F_h = M_h\left\{1 - \left(1 - \frac{1}{k_r}\right)\left[\frac{(M_h - 1)}{M_h}\right]^2\right\} \qquad (20)$$

where $k_r$ is the ratio $\alpha_e / \alpha_h$ and it has to be as small or large as possible to minimize the avalanche noise. The total signal to noise expression for an APD device can be expressed as the ratio between the gained optical power ( $\langle {i_{ph}}^2 \rangle M^2$) and the possible noise sources:

$$\langle i_N^2 \rangle = 2q\left(I_{ph} + I_D\right)FB \qquad [Detector\ noise\ power] \qquad (21)$$

$$\langle i_B^2 \rangle = 2qI_L\,B \qquad [Shot\ amplifier\ noise\ power] \qquad (22)$$

$$\langle i_T^2 \rangle = \frac{4k_BTB}{R_{eq}} \qquad [Thermal\ amplifier\ noise\ power] \qquad (23)$$

$$\left(\frac{S}{N}\right)_{Power} = \frac{\frac{1}{2}\left(\frac{q\eta P_{incident}\,\Gamma g}{h\nu}\right)M^2}{\langle i_N^2\rangle M^2 + \langle i_B^2\rangle + \langle i_T^2\rangle} \qquad (24)$$

where $q$ is the elementary electron charge, $I_D$ the dark current, B the device bandwidth, $I_L$ the induced background radiation current and $R_{eq}$ the load amplifier resistance.

# Reference


[1] Vivek Sharma, Kyoungweon Park, and Mohan Srinivasarao, "Colloidal dispersion of gold nanorods: Historical background, optical properties, seed-mediated synthesis, shape separation and self-assembly", Materials Science and Engineering: R: Reports **65** (1), 1 (2009).

[2] R. H. Ritchie, "Plasma Losses by Fast Electrons in Thin Films", Physical Review **106** (5), 874 (1957).

[3] William L. Barnes, Alain Dereux, and Thomas W. Ebbesen, "Surface plasmon subwavelength optics", Nature **424**, 824 (2003).

[4] W.E. Lawrence, *A study of umklapp scattering and transport coefficients in simple metals*. (Cornell University, 1970).

[5] E. Kretschmann and H. Raether, in *Zeitschrift für Naturforschung A* (1968), Vol. 23, p. 2135.

[6] H.C. Hulst and H.C. van de Hulst, *Light Scattering by Small Particles*. (Dover Publications, 1981).

[7] M. Faraday, "Experiemntal relations of gold (and other metals) to light", Philosophical Transactions of the Royal Society of London **147** (36.) (1857).

[8] Gonçalo Doria, João Conde, Bruno Veigas, Leticia Giestas, Carina Almeida, Maria Assunção, João Rosa, and Pedro V. Baptista, "Noble Metal Nanoparticles for Biosensing Applications", Sensors **12** (2), 1657 (2012).

[9] Pooja Tiwari, Komal Vig, Vida Dennis, and Shree Singh, "Functionalized Gold Nanoparticles and Their Biomedical Applications", Nanomaterials **1** (1), 31 (2011).

[10] Reuben Hudson, Go Hamasaka, Takao Osako, Yoichi M. A. Yamada, Chao-Jun Li, Yasuhiro Uozumi, and Audrey Moores, "Highly efficient iron(0) nanoparticle-catalyzed hydrogenation in water in flow", Green Chemistry **15** (8), 2141 (2013).

[11] Erik C Dreaden, Lauren A Austin, Megan A Mackey, and Mostafa A El-Sayed, "Size matters: gold nanoparticles in targeted cancer drug delivery", Therapeutic Delivery **3** (4), 457 (2012).

[12] Peng Hui Wang, Morgan Millard, and Alexandre G. Brolo, "Optimizing Plasmonic Silicon Photovoltaics with Ag and Au Nanoparticle Mixtures", The Journal of Physical Chemistry C **118** (11), 5889 (2014).

[13] H. Bönnemann, G. Braun, W. Brijoux, R. Brinkmann, A. Schulze Tilling, K. Seevogel, and K. Siepen, "Nanoscale colloidal metals and alloys stabilized by solvents and surfactants Preparation and use as catalyst precursors", Journal of Organometallic Chemistry **520** (1), 143 (1996).

[14] T. N. Castro Dantas, M. H. de Lucena Neto, A. A. Dantas Neto, M. C. P. Alencar Moura, and E. L. Barros Neto, "New Surfactant for Gallium and Aluminum Extraction by Microemulsion", Industrial & Engineering Chemistry Research **44** (17), 6784 (2005).

[15] Ekaterina B. Zhulina, Oleg V. Borisov, and Victor A. Priamitsyn, "Theory of steric stabilization of colloid dispersions by grafted polymers", Journal of Colloid and Interface Science **137** (2), 495 (1990).

[16] T. A. Witten and P. A. Pincus, "Colloid stabilization by long grafted polymers", Macromolecules **19** (10), 2509 (1986).

[17] B. E. Conway, J. O'M Bockris, and I. A. Ammar, "The dielectric constant of the solution in the diffuse and Helmholtz double layers at a charged interface in aqueous solution", Transactions of the Faraday Society **47** (0), 756 (1951).

[18] W. I. Goldburg, "Dynamic light scattering", American Journal of Physics **67** (12), 1152 (1999).

[19] Arthur L. Aden and Milton Kerker, "Scattering of Electromagnetic Waves from Two Concentric Spheres", Journal of Applied Physics **22** (10), 1242 (1951).

# Chapter 3
# Fabrication and characterization techniques

## 3.1 Material growth methods

### 3.1.1 Thermal evaporation

Since almost every material presents a characteristic boiling point, it is possible to change its status from solid to vapor to let it condensate on a chosen surface. Among many of the physical vapor deposition (PVD) methods, thermal evaporation systems will use Joule effect to heat the target material. Once that the material is turned to vapor, the spare atoms acquired ballistic kinetic energy towards the sample surface, where an high vacuum level was previously created to assure the highest particle free mean path.

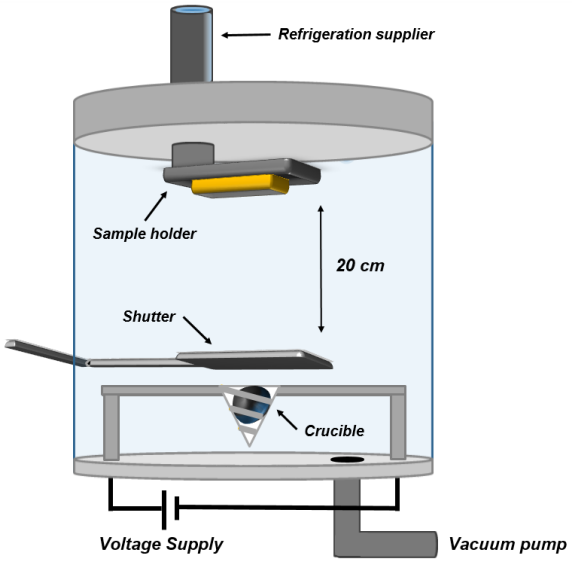


Figure 1: Thermal evaporation system.

Figure 1 shows the evaporation system used in the further experiments, where target material is placed in a heater crucible. Most common used thermal source is made of a tungsten filament (99.9% purity) heated by Joule effect. It can be heated up to 3.400 °C allowing the evaporation of most of the target materials including Ga and Au. The presence of a shutter allows a relative short time to start and end the growing process by physically blocking the material flow toward the sample. Typical working pressure is about $2 \cdot 10^{-3}$ mTorr made by the help of a turbomolecular vacuum pump. For our process, 0.28 g of solid Ga target (99.999%) was load in a Edwards E306 thermal evaporator for 30 seconds with 50 W DC power supply. To pursuit a more uniform deposition, the substrate temperature was kept as low as possible with the aid of a built-in ice cooling system.

## 3.1.2 Magnetron sputtering

One of the most exploited physical deposition method employs the use of a gas plasma to sputter a target material and let its atoms reorganize on a selected surface. The plasma is usually generate using inert gasses such as Argon, which is a low reacting gas but a large variety of species can be employed for the formation of multicomponent thin film. Typical equipment configuration consists of a metal anode and cathode where the sample and the material target will be allocated respectively. Depending on the gas flow and the applied voltage, the plasma ions bombardment energy and rate will change, hence the deposition of the sputtered material. The latter will form a coverage layer that may present inclusions of other reacting gasses like $N_2$ or $O_2$.

The equipment used in this thesis was an Alcatel A450 RF sputtering equipment. During the AZO deposition (chapter 4) the system used an RF source set at 150 W with a 50 sccm Ar flow at $10^{-2}$ mbar in order to create the plasma to etch the AZO target (Kurt J. Lesker ZnO / Al2O3, 2% Standard Doping). While for the fabrication of the AlN passivation layer (chapter 6), same chamber pressure and Ar flow were used but adding 40 sccm of $N_2$. For the latter case, the gasses were accelerated with a 250 W DC source for different

times to study the thickness layer properties. For all the process, a pre-sputtering step of 1 minute was run to avoid possible impurity contamination of the target.

# 3.2 Electro-optical characterization

## 3.2.1 Ellipsometry

The optical characterization of thin layers has been a prime role tool for many investigation fields such as material science, semiconductor technology or sensing development. Among many optical analysis technique, spectroscopic ellipsometry (SE) allows a fast and precise analysis to investigate the material surface properties. By the determination of the layer effective permittivity ($\varepsilon_{eff}$) it is possible to study the layer thickness and optical parameter.

Considering an incident light beam, it can be treated as an electromagnetic wave with an amplitude $E_0$ and a phase $\delta$, which can be related in the phasor form as follows:

$$\hat{E} = E_0 e^{j\delta} \qquad (1)$$

However, depending on the electric field oscillation plane respect to the incident plane, it will be possible to refer to the wave as parallel ($\mathcal{s}$) or perpendicular (p) polarized:

$$\hat{E}_p = E_p e^{j\delta_p} \qquad (2)$$

$$\hat{E}_\mathcal{s} = E_\mathcal{s} e^{j\delta_\mathcal{s}} \qquad (3)$$

Ellipsometry measurement use these to extrapolate the so called Fresnel reflection coefficients ($r_p$, $r_S$), which are define as:

$$r_p = \frac{\hat{E}_p^R}{\hat{E}_p^I} = |r_p| e^{j\delta_P}, \qquad |r_p| = \frac{E_{R,p}}{E_{I,p}}, \qquad \delta_P = \delta_{I,p} - \delta_{R,p} \tag{4}$$

$$r_S = \frac{\hat{E}_s^R}{\hat{E}_s^I} = |r_s| e^{j\delta_S}, \qquad |r_s| = \frac{E_{R,s}}{E_{I,s}}, \qquad \delta_S = \delta_{I,s} - \delta_{R,s} \tag{5}$$

where the $R$ and $I$ notation are the reflected and the incident component respectively. Thus, the equipment will give back the information about the related amplitude change between p and s component of the reflected beam ($\Psi$) and their phase shift ($\Delta$):

$$\tan(\Psi) = \frac{|r_p|}{|r_S|}, \qquad \Delta = \delta_P - \delta_S \tag{6}$$

In the case of a thin film covered substrate, the Fresnel coefficients can be expressed as the geometrical series of all the reflected component from each interface (air/layer and layer/substrate) which converges to:

$$N = n + ik \tag{7}$$

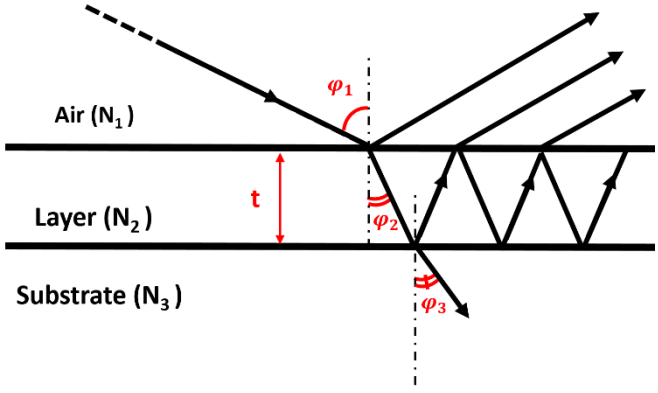


$$r_{1,3}^p = \frac{r_{1,2}^p + r_{2,3}^p\, e^{-j2\beta}}{1 + r_{1,2}^p \cdot r_{2,3}^p\, e^{-j2\beta}} \tag{8}$$

$$r_{1,3}^S = \frac{r_{1,2}^S + r_{2,3}^S\, e^{-j2\beta}}{1 + r_{1,2}^S \cdot r_{2,3}^S\, e^{-j2\beta}} \tag{9}$$

$$\beta = 2\pi \frac{t_{layer}}{\lambda} N_2 \cos\varphi_2 \tag{10}$$

Figure 3: Ellipsometry multiple light scattering sketch in air/layer/substrate sample. In this case, Fresnel coefficient can be obtained by Eq. (8) and Eq. (9).

where n is the refractive index and k is the absorption coefficient. From the relation between the Fresnel coefficients and the physical parameter N of the layer, it is possible to calculate the so called pseudo-electric permittivity $\langle\varepsilon\rangle$. The latter gives physical information of the considered multilayer structure, where single material parameters can be extrapolated:

$$\langle\varepsilon\rangle = \langle\varepsilon_r\rangle + i\langle\varepsilon_i\rangle \qquad (11)$$

$$\langle\varepsilon_r\rangle = \sin^2(\varphi_1)\cdot\left(1+\frac{\tan^2(\varphi_1)\cdot(\cos^2(2\Psi)-\sin^2(\Delta)\cdot\sin^2(2\Psi))}{(1+\sin(2\Psi)\cdot\cos(\Delta))^2}\right) \qquad (12)$$

$$\langle\varepsilon_i\rangle = \frac{\sin^2(\varphi_1)\cdot\tan^2(\varphi_1)\cdot\sin(4\Psi)\cdot\sin(\Delta)}{(1+\sin(2\Psi)\cdot\cos(\Delta))^2} \qquad (13)$$

The equipment used in this work was a UVISEL Jobin-Yvon photoelastic modulator (HR-250 model) with a Xenon source for input unpolarized light in the UV-Visible spectral range (1.5 and 4.5 eV). The output signal was detected by a photomultiplier tube Hamamatsu R928S.

## 3.2.2 Spectrophotometry

To study the interaction between the light and dispersed entities in a solution, a direct evidence of the absorption and scattering properties is needed. With the use of spectrophotometer, it is possible to detect both these features in a single spectrum, simply calculating the sample absorbance using the Beer-Labert law:

$$A = \log_{10}\left(\frac{\Phi_e^i}{\Phi_e^t}\right) = -\log_{10}(T) \qquad (14)$$

where $\Phi_e^i$is the light transmitted radiant flux through the sample, $\Phi_e^i$ is the incident radiant flux of photons and their ratio $T$ is also known as transmission. Of course the measured out coming signal does not discern from absorbed or scattered light, since it directly takes into account the impinging light on the final light sensor.

Figure 4 shows a real image and a schematic of a real equipment. A lamp source light is collimated to a monochromator crystal, which returns a precise wavelength depending on the light incident angle. Finally, the light is collimated through a fiber on the sample and the output signal is measured with the help of an appropriate detector. Typically, UV-VIS lamp source is the most used because of the large use of spectrophotometry in the chemical analysis field.

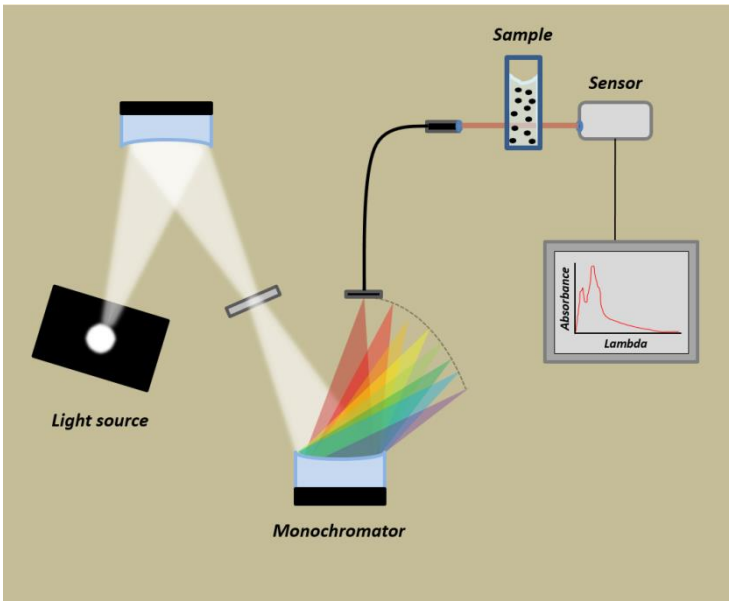


Figure 4: (On the left) A schematic illustration of the main spectrophotometer components. After that the light from the source is collimated to the monochromator, one of the out-coming light is selected and guided by an optical fiber to the sample stage. The light/sample interactions are measured with a sensor that allows to display the absorbance trend as function of the wavelength. (On the right) A picture of the used equipment.

The UV-visible spectra measurement in this thesis were done using a Thermo Scientific GO spectrophotometer. The analysis interested a spectral range between 200

and 1000 nm with a resolution of 1 nm, where the temperature was fixed at 25 °C by means of the equipment. The sample were analyzed in a 1.0 $cm^2$ quartz cuvette using the same colloidal solvent as reference.

## 3.2.3 Fourier transform infrared (FTIR) analysis

Similarly to spectrophotometer, dispersive instruments had been used to measure sample interaction with a broad range of infrared (IR) light. Typical issues related to these type of measurements are:

- Slow scanning time
- Low measurement sensitivity (instrument SNR)
- Can be a destructive technique

These problems were overcome when the first interferometer was used to measure the range frequencies simultaneously at the same time. The out-coming signal from an interferometer is called interferogram and it contains information about all the required wavelength decoded with post processing Fourier transform calculations. This method allows faster measurement (seconds instead minutes) with a lower SNR compared to other similar analysis technique.

An infrared light source is used as the interferometer input to create the interferogram and further directed on the sample surface. The light can be reflected, absorbed or transmitted and the detector measured parameter will depends on the analysis. Last step involved the signal post processing to interpret the Fourier transformation data.

FT-IR measurements are often used for biological samples analysis due to the peculiar molecules vibration in the IR (absorption measurements). However, the used of this technique has been found fruitful for other investigation scopes such as material reflection and transmission analysis. In this thesis a Bruker IFS66v was used for reflection and transmission measurements between 7000 and 500 $cm^{-1}$ at a working vacuum level of $10^{-4}$ mbar. The measurements were taken for a 1 cm aperture of the incident light with a resolution of 6 $cm^{-1}$ every 250 scan.

## 3.2.4 I-V photocurrent

An optical setup for the characterization of the Avalanche photodiode has been built. The sensor photocurrent measurement required the use of a laser diode device with a 1550 nm wavelength. The laser, acquired from Covega/Thorlabs, was temperature stabilized under DC operation by a temperature controller (TEC) and it was assembled onto a faraday cage in a customized setup (Figure 5). This allows us to directly insert the fiber on a Karl Suss four-probe station inside the cage to prevent environmental light noise. The laser beam was collimated at the fiber output and the power was adjust by changing laser currents and using fiber optical attenuators. To calculate the beam power density, a power meter equipment with thermocouple array sensor was used.

The device was connected with micro tips to an HP 4145B parameter analyzer to measure the I-V characteristic. The applied voltage ranges from 0 to 75 V with a step of 300 mV and the maximum current was limited at 1 mA. The signals were acquired every 20 ms as a result of a mean integration of 16 point (medium integration time) allowing to low the overall SNR of the measurement.

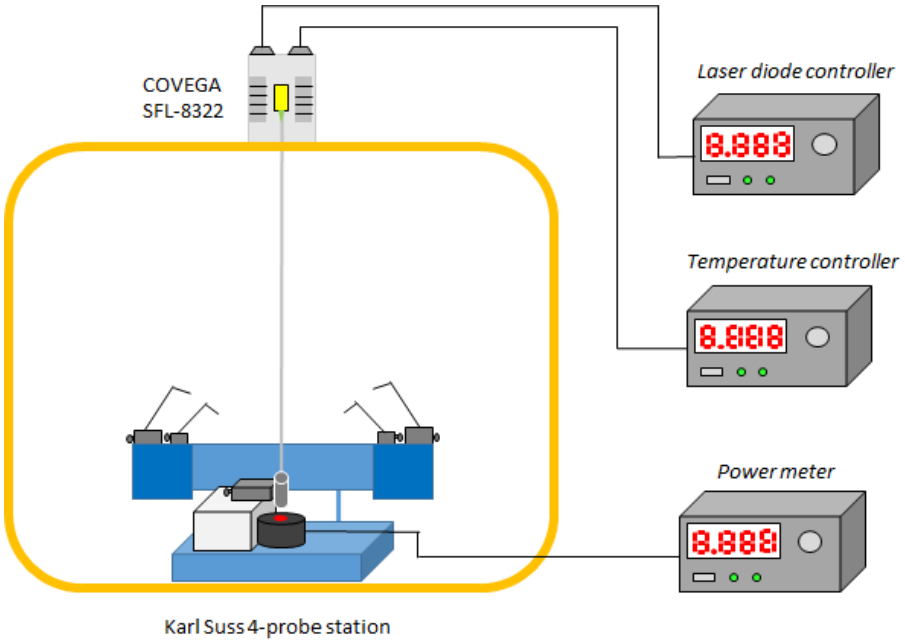


*Figure 5:* Optical setup for photocurrent measurement

# 3.3 Morphological studies

## 3.3.1 Scanning electron microscopy (SEM)

To visualize a live image of a surface at the nanoscale, scanning electron microscopy (SEM) can be used. This technique allows to raster a surface profile with a collimate electrons ray, detecting the signal after their interaction with the sample. Depending on the particle lost energy, different types of information can be extrapolated to reconstruct a 3D view of the profile. The SEM investigation was carried out using a Philips XL30 S-FEG microscope (Philips, Amsterdam, The Netherlands) under a $10^{-3}$ bar pressure at room temperature. Sample were analyzed for three main types of analysis:

- Top view

- Tilted view
- Cross section view

As-evaporated Ga NP on semiconductor or metal substrates allowed to acquire good images up to a magnification factor of 400k with an electron ray acceleration voltage of 10 kV in all types of images. Regards the evaporated sample on quartz instead, previous metallization of the sample was required due to high surface local charge of the beneath insulator material. Finally, top and tilted view images of the synthetized colloidal drop casted also were taken. After the investigation, images were post-processed by Gwyddion open-source software to estimate nanoparticle size and distribution.

## 3.3.2 Transmission electron microscopy (TEM)

Since the SEM allows fast and medium resolution analysis, higher resolution images with additional elemental information can be obtained using transmission electron microscopy (TEM) technique. In this case, the generated electron beam passes through the sample, which need previous preparation steps to be turn into a thin foil. This can be usually achieved using a tomography equipment or even by focused ion beam (FIB) method. The detection of transmitted and scattered particles in the measurement chamber allows to collect a plenty of material information such as crystallization zones, morphology issues, material composition or interlayer mechanical stress areas. Among all these analysis, the electron energy loss spectroscopy (EELS) was used in Chapter 4 for the detection of LSPR and bulk plasmon resonance in the synthetized colloidal Ga NPs. Since scattering plasmon excitation is due to inelastic interactions, it will be possible to map the resonance energy across the sample area with spatial and energy high resolution. The used equipment in this thesis was a JEOL JEM-2010F with a electron cannon energy of 200 kV with a GATAN GIF energy filter.

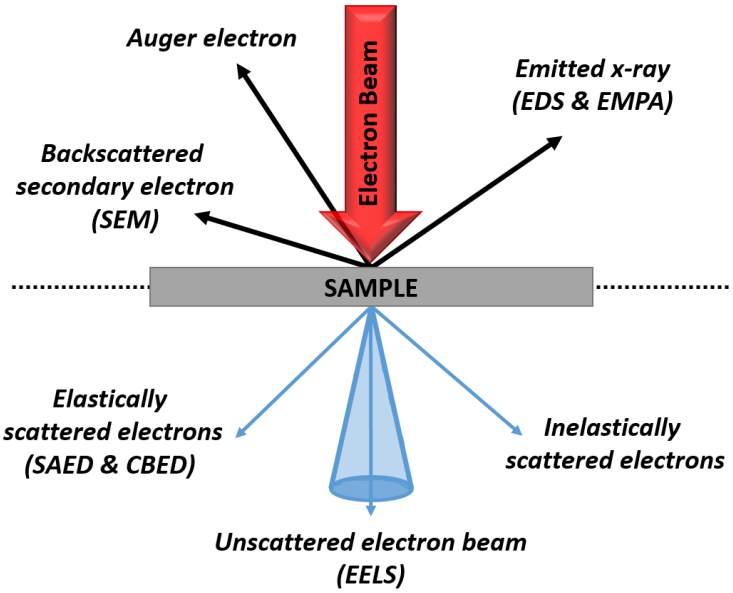


*Figure 6:* TEM detectable signals and their related analysis

## 3.3.3 Atomic force microscopy (AFM)

Even if SEM and TEM analysis give good visual perception of the sample surface structure, quantitative measures such as surface roughness or inclination degree are not easy information to extrapolate. For this purpose, other investigation methods like the atomic force microscopy (AFM) can be helpful.

The AFM system is made by a resonant cantilever with an ending tip that acts as a scan probe. The interaction between the surface and the tip, which are mostly Van de Walls type, will be traduce in height position that will form the analyzed surface profile. The movements of the tip will be detected by means of a focused laser beam on the cantilever and a photodiode detector as shown in figure 7. The change in light amplitude will be traduce as tip height displacement along the three axes. There are three possible imaging modes in AFM:

- Contact mode
- Taping mode
- Non-contact mode

The first let the cantilever bends because of the repulsive surface forces maintaining a deflection offset used as feedback in order to calculate the forces, hence the movement value. This mode allows fast and good results but with the possibility to damage the tip or the sample. Typically, the resolution is about 1 nm and 0.1 nm on the x-y (parallel plane to the surface) and z axes respectively.

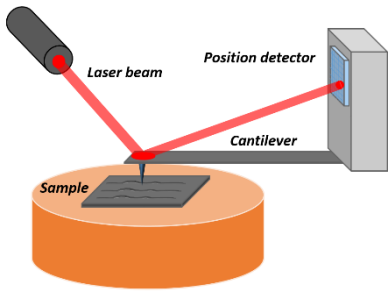


*Figure 7:* AFM system sketch. The tip ending of the equipment cantilever raster the sample surface to map the profile. The movements of the tip in one of the axes directions is promptly registered by sensor, which traduce the laser intensity variations to position coordinates.

About the taping mode, the cantilever oscillates at a certain resonant frequency, gently tapping on the sample surface, limiting the contact time. It allows good images result but with slower acquisition time. Finally, non-contact mode used the attractive force due to the presence of some surface liquid (e.g. air humidity condensation). This method assures a long lifetime of the probe with low applied force on the sample. However, images show lower resolution and impurities on the surface can give misleading results.

The sputtered AZO layer surface in chapter 4 was investigated using an Agilent PicoPlus 5500 AFM was used operating in taping mode. Images were analyzed and post-processed by Gwyddion open source software to investigate the surface morphology of both samples.

## 3.3.4 X-ray diffraction (XRD)

Light can interact with matter in a plenty of way depending of its energy and frequency and the intrinsic material structural composition. When a monochromatic x-ray beam is used, the beam can interact with the atoms and if it is scattered can give compositional and crystallographic information about the sample. In order to let the scattered light at different atomic planes interfere constructively, the Bragg's law has to be satisfied:

$$\lambda = 2d_{hkl}\sin(\theta) \qquad (15)$$

where $d$ is the plane distance calculated at a certain Miller indices $h, k$ and $l$. In the case the diffraction is produced, the angle and intensity scattered light measurement allows the material identification. Each material has its characteristic diffraction pattern that makes it recognizable in large material data base.

The equipment used in this work was a X'Pert Pro Panalytical system with Cu X-ray tube as source and collimated light in a Soller slit (0.04 rad). The output signal was detected by means of a Xe gas scintillator with fixed incidence angle of 0.5°, 2θ angle varied from 10° to 90° with 0.04° step and an acquisition time of 4 s analyzed.

# Chapter 4
# New synthesis method for colloidal Ga NPs in a chosen solution

The possibility of tuning the NPs properties by the selection of specific material, shape and surface functionalization has made them suitable candidates for plenty of applications. It has been demonstrated how NPs deposition on light sensor surface may lead to an enhancement of the detected optical signal[1] but also their use as bio-sensor[2] and drug delivery[3] has been attested. The NP interaction with an incoming light can excite a localized surface plasmon resonance (LSPR), which has been matter of study by many groups. The optical absorption peak, which is related to the LSPR of the sample can range from UV to the IR spectra, depending the NPs physical and geometrical features. In the case of Gallium NP (Ga NPs), the resonance can be tuned between the visible and the UV range of the electromagnetic spectrum.

We present a new method to synthetize colloidal Ga NPs in a selected solvent by evaporating process and with the use of an aluminum zinc oxide (AZO) as an expendable layer. The average particles dimension distribution ranged from 10 nm to 200 nm as diameter, and their aggregation status depending on the solvent nature. The colloidal solution was further characterize with the use of SEM, TEM, UV spectrophotometer and Raman spectroscopy. Moreover, one of the main issues of conventional chemical colloidal solution regards the solvent and surfactants agent selection to avoid NP agglomeration in liquid as previously discussed in Chapter 2. Thus, the colloidal electrostatic stabilization approach was investigated in deionized water (DIW), tetrahydrofuran (THF) and ethanol (EtOH). These organic solvents can be sorted in two classes: polar protic and polar aprotic. The first has molecules that easily release a hydrogen ion (usually bonded with an OH group or a nitrogen) to the reagent. In contrast, the aprotic solvents tends to supply less

protons. Agglomeration behaviors were related to the electrostatic configuration around the NP, hence their zeta potential as previously described in Chapter 2.

# 4.1 Nano-liquid agglomeration theory

A nano-liquid is defined as a colloidal solution with particles smaller than 100 nm, where the mixture properties comes both from solid and liquid phase. The NPs usually tend to agglomerate because of the particles mutual interactions and good dispersion can be a challenging task.[4] Large clusters, usually up to micron size, can produce a red-shift on the single particles absorbance frequency depending on the agglomeration size. The forces on particles in a solution are the Gravitational and Brownian forces. They may act differently depending on the NPs size, density and environment temperature as shown in Eq. (1)[5]:

$$\frac{F_{gravitational}}{F_{Brownian}} = \frac{g\ \Delta\rho\ a^3}{k_B T} \qquad (1)$$

where $a$ is the particle radius, $\rho$ is the particle density, g is the gravitational constant, $k_B$ is the Boltzmann constant and $T$ is the liquid temperature. Gravitational forces is about three order of magnitude less effective on small NP, since Brownian motion is too large to allow gravitation force act on them (e.g. sedimentation). In that case, the NPs agglomeration rate is barely determined by electrostatic (*repulsive force*) and Van Der Waals (*attractive force*) interactions. It is possible to calculate this two different contributions by the equivalent potential for a sphere particle as follow[6] :

$$V_{particel-particle} = V_{vdW_{pp}} + V_{el_{pp}} \qquad (2)$$

$$V_{vdW_{pp}} \propto -s^{-2} \quad (3)$$

$$V_{el_{pp}} \propto a\, n_{\infty}\, (k^{-1})^2\, \zeta^2\, exp(\frac{-s}{k^{-1}}) \quad (4)$$

where $n_{\infty}$is the ionic concentration of the suspension, $s$ is the distance between the two particles, $\zeta$ is the zeta potential and $k^{-1}$ is the Debye length of the suspension. The last measures the charge carrier net electrostatic effect in solution and how far those electrostatic effects persist, potentially screening the particle surface from other particle interaction. According to the Derjaguin-Landau-Verwey-Overbeek (DLVO) theory, the total surface energy can be expressed as the sum of this two interactions related to distance from the NP surface as shown in Figure 1.

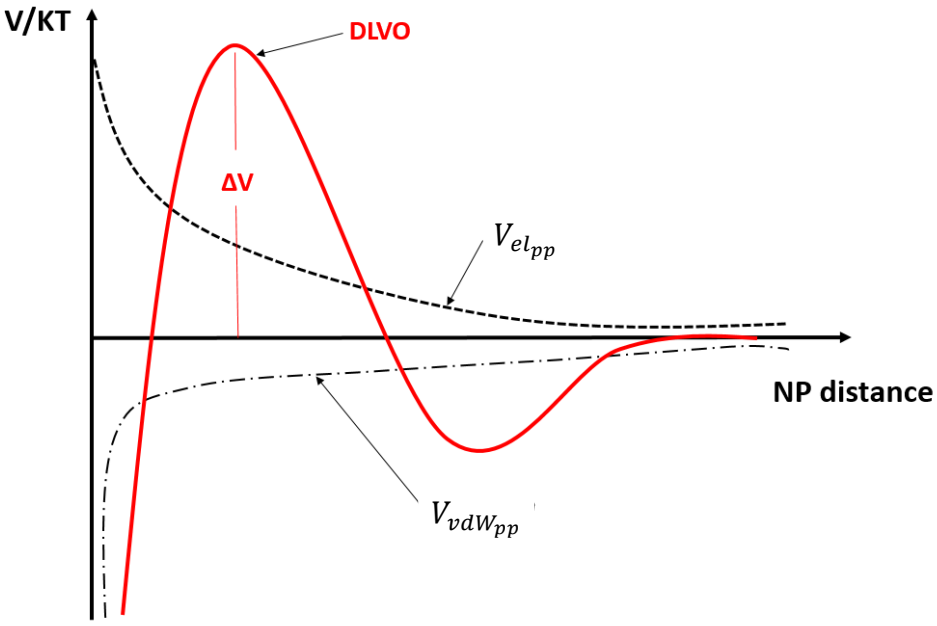


Figure 1: Potential energy trends depending on the NPs related distance.

where V/KT is the NPs interaction energy where ΔV is the potential barrier to avoid colloidal agglomeration process. An extended DLVO theory (XDLVO) shows how the DLVO curve may change because of Hydrophobic and Osmotic repulsion contributions related to nanoparticles and solution properties.[7] Considering same suspension and particles made by same material, smaller NPs potential barrier will be lower, hence higher agglomeration probability.[8]

# 4.2 Ga NPs colloidal synthesis

A colloidal solution of gallium nanoparticles was prepared with the following procedure as shown in figure 2. First, a substrate of silicon with an area of 0.5 cm x 2 cm was cleaved and cleaned using an aqueous solution of 40 % fluorhydric acid in order to remove the native oxide.

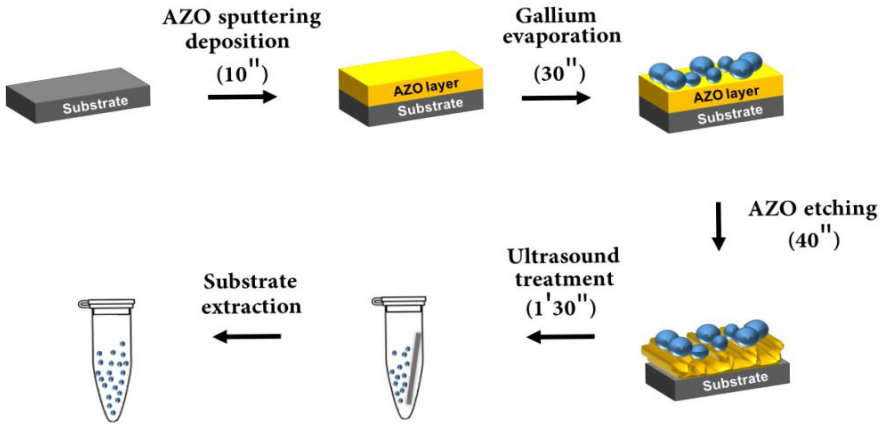


Figure 2: Colloidal Ga NPs synthesis steps

Next step was the room temperature deposition of an Aluminum Zinc Oxide (AZO) expendable layer carried out by an Alcatel A450 RF sputtering equipment. The system used an RF source set at 150 W with a 50 sccm Argon flow in order to create the plasma to etch the AZO target (Kurt J. Lesker ZnO / Al2O3, 2% Standard Doping). In addition, a pre-

sputtering step of 1 minute was set to avoid possible impurity contamination of the target. The selection of the expendable layer material was done taking into account the following parameters: Ga NPs evaporation feasibility, Ga NPs compatibility with the used acids and etching rate of the layer. Later, gallium NPs were evaporated on the sample with the use of a physical vapor deposition (PVD) equipment. For our process, 0.28 g of solid gallium target was heated for 30 seconds with 50 W DC power supply under $10^{-6}$ Torr vacuum. To pursuit a more uniform deposition, the substrate temperature was kept as low as possible with the help of an ice cooling system. At this point, several vials were filled with the following solvents: DIW and THF. The solvents were chosen because of their peculiar chemical properties, in order to study different interaction between the colloidal nanoparticles. Water is a polar protic liquid, which means higher probability of H+ ions exchange between the liquid and the NPs electric double layer. Aqueous solution gave us the possibility to study the colloids behavior at different pH levels, yielding different NP surface charges, while THF was used to test the Ga NPs in polar aprotic solvent to study the NP agglomeration property in that chemical environment. At this point, the sample was immersed in a $H_3PO_4$/acetic acid/DIW (1:1:75) bath to etch the AZO layer and weaken the NPs bonds with the substrate and promptly inserted into the selected solvent. Finally, an ultrasound treatment of 1’ 30’’ was used to break NPs up from the hard support and let them be dispersed into the liquid.

# 4.3 Ga NPs colloidal structural study

First analysis concerned the study of the nanoparticles stability in acidic environment by their evaporation on a bare glass substrate (figure 3.a). The Ga NPs were immersed in the AZO etchant solution at pH 1 for different times up to 120 minutes. After 1 minute, the scanning electron microscopy (SEM) images showed a slightly change of the NP distribution compared to the as-evaporated. It seems that bigger NP reduced their dimension, shifting the distribution towards smaller diameter values. After 120 minutes

etching, the smaller NPs (~ 20 nm) disappeared and bigger ones (~ 90 nm) keep the same distribution as in the 1 minute etching. As a result, the etching time for the colloidal synthesis was set between 30 and 40 seconds, to assure the highest NPs detachment probability during US treatment without causing possible structural damages to the nanoparticles. It is believed that the outer gallium oxide shell probably guarantee enough chemical stability of the particle at the examined time.[9, 10]

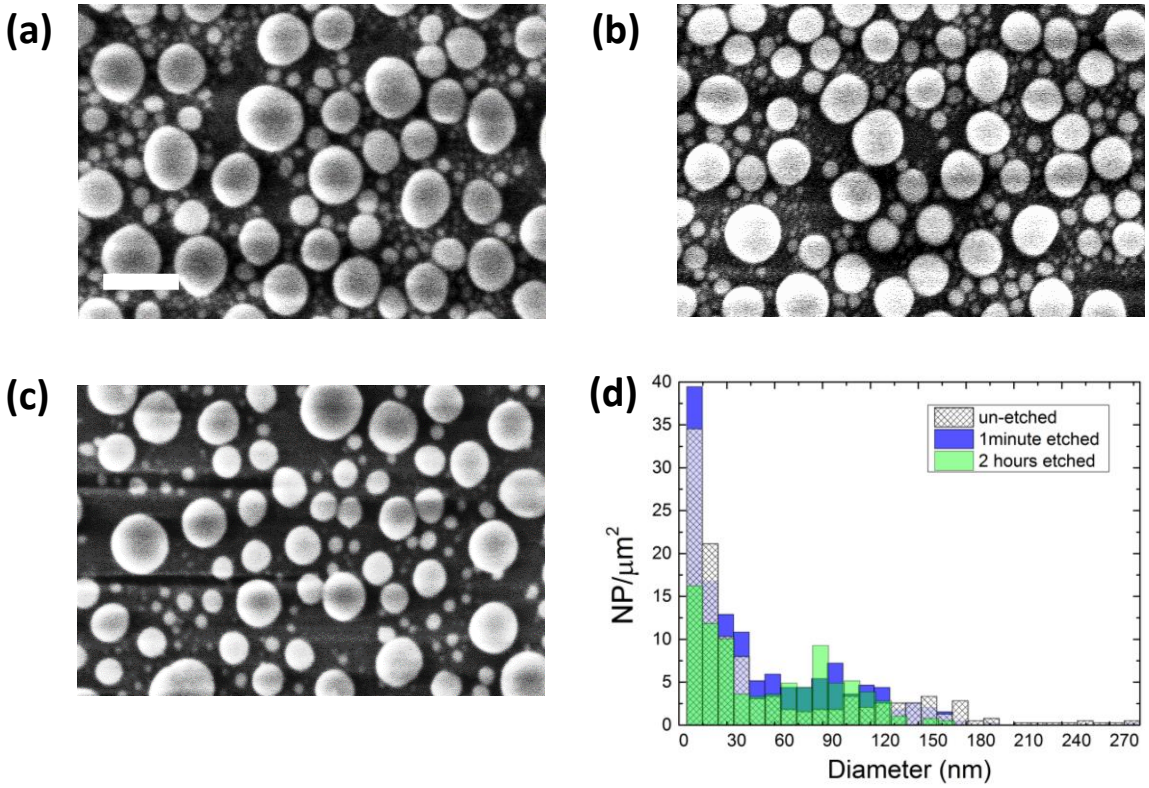


Figure 3: (a) Ga NPs evaporated on a glass substrate and immersed in an acidic bath for (b) 1 min, (c) 2 hours. (d) Histograms obtained from the SEM images. Scale bar is 200 nm in length.

Later, to characterize the sputtered AZO layer surface roughness, it was used an atomic force microscopy. In order to grow a 300 nm thick AZO layer on a silicon substrate, the process power was set at 150 W with the sample holder at room temperature and 300 $^{o}$C. Images were analyzed and post processed by Gwydion software to investigate grain boundaries density of different samples. As Atomic Force Microscopic (AFM) analysis exhibit (Figure 4), the RT sample shows a less average surface roughness (6 nm) compared

to the high temperature grown layer (13.6 nm).The higher the roughness, the more the available surface can be covered by NP leading to higher NP yield. Also, the high temperature case showed lower grain boundaries density compare to the RT, which may allow a more uniform process during the etching step. Given that results of 300 °C were promising, an analysis of the Ga NPs growth on this two different expendable layers were studied to identify the more suitable candidate for our synthesis.

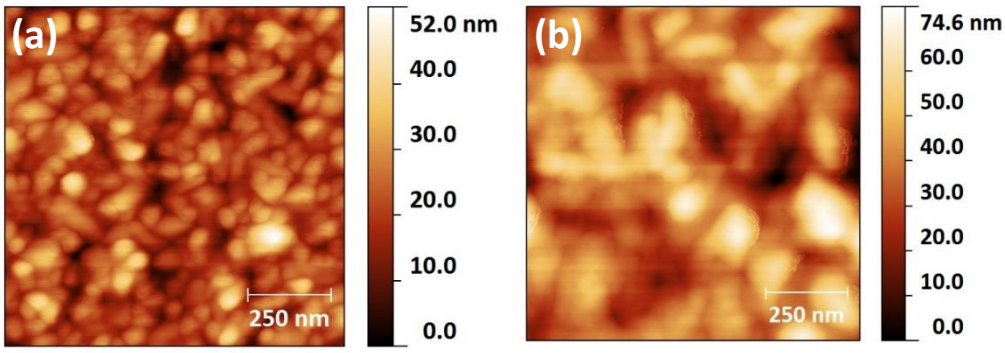


Figure 4: AFM images of the surface of (a) AZO layer deposited at RT and (b) AZO layer deposited at 300 °C.

Further TEM analysis of the evaporated sample were carried out (figure 5). The NP shows an average contact angle less than 90° no matter the dimension. It indicates that the AZO surface has hydrophilic property with Ga material. The latter tends to easily wet

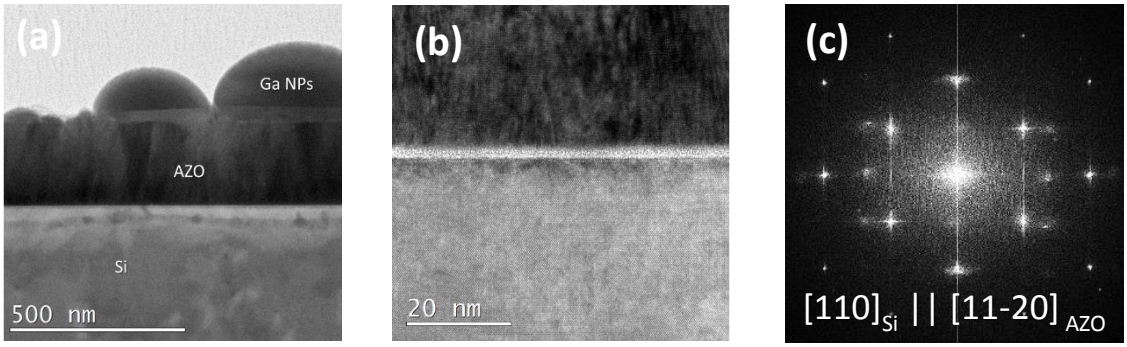


Figure 5: (a) TEM image of Ga NPs showing different sizes on AZO/Si substrate. (b) HRTEM image of the interface between the Si and the AZO. (c) FFTs of the AZO and Si substrate.

the surface resulting in higher mobility of the NP, which can lead to the formation of bigger structure due to clustering phenomena.[11] However, comparative studies of the Ga NP distribution on different substrates (Si and quartz) after 60'' evaporation time found similar NP size as in the AZO case. As expected, the expendable layer measured a thickness of about 200 nm with an excellent quality at the Si interface (figure 5.b).

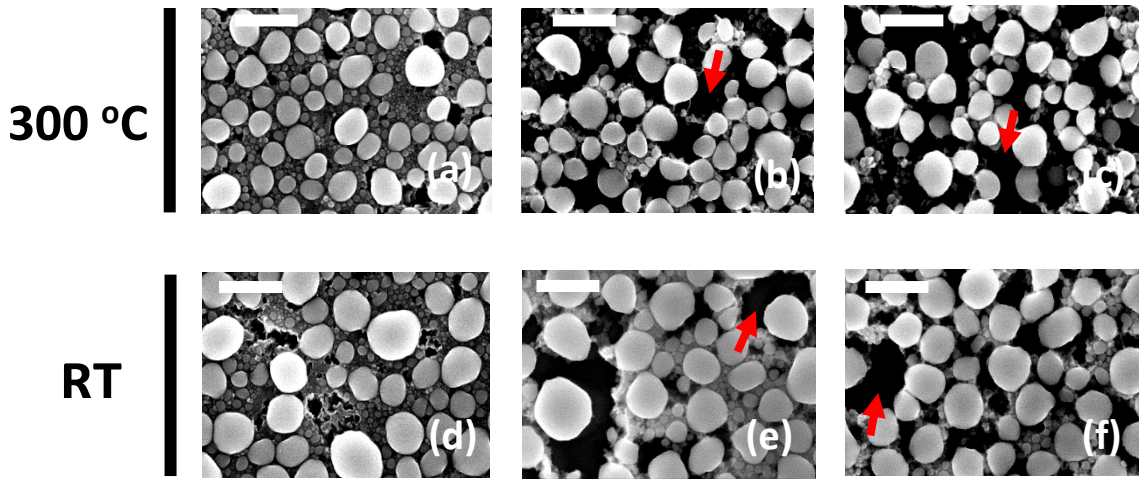


Figure 6: Ga NP/ AZO/ Si sample immersed in water/ phosphoric acid/ acetic acid bath for (a,d) 5 s (b,e) 15 s and (c,f) 20 s. Scale bars are 500 nm in length.

The fast Fourier transform (FFT) of high resolution measurements showed the epitaxial relationship of the AZO with the beneath Si substrate as: $(0001)[11\text{-}20]_{AZO}||(001)[110]_{Si}$. It is strongly believe that the preferencial growth direction is likely due to the 300 °C temperature process as the good Si interface as well. The high interface quality and the preferential orientation of the AZO material help to obtain a homogeneous etching process of the expendable layer during the NPs dispersion step.

Figure 6 shows SEM viewgraphs during the etching process of GaNP/AZO/Si samples with AZO layers deposited at RT and 300° C. For the high temperature growth sample, the etching rate is faster and steadier than in the RT case, breaking up simultaneously a higher number of nanoparticles from the substrate. By measuring the etching depth of bare AZO and with the Ga NPs top layer, the etching rate was found to be 18 nm/s and 6 nm/ s

respectively. The sample showed good etching resistance within the first 5 seconds due to the presence of the Ga NPs coverage. After that time the AZO layer almost disappeared and left most of the nanoparticles weakly bonded with the substrate. This non-linear behavior can be caused by the incoming discontinuity of the Ga NPs protection layer effect, which leads to a gradually higher etching rate of the substrate because of the increasing ratio between etched surface and acid solution.

The as-evaporated NPs size distributions were calculated for both cases, in order to recognize the process with higher yield. Figure 7 bar graph shows the distributions, where the first column is centered at a diameter of 12 nm with a width of ± 6 nm. The RT sample shows higher presence of bigger NPs with shortage of smaller one. The higher grain density of the RT may leads to higher free surface energy, hence larger mobility of the Ga NP during the coalescent phenomena. Nevertheless, the higher NP density in the 300 °C case might be related to the rougher surface because of a larger surface to volume ratio in those samples. Therefore, absorption analysis on the corresponding colloidal solutions in THF were carried out to find the relationship between the initial NP distributions and the detected absorption. The high temperature growth of the expandable layer brought to a 50% enhancement of the signal compared to the RT case and for this reason, it was chosen to develop our Ga NP colloidal solutions.

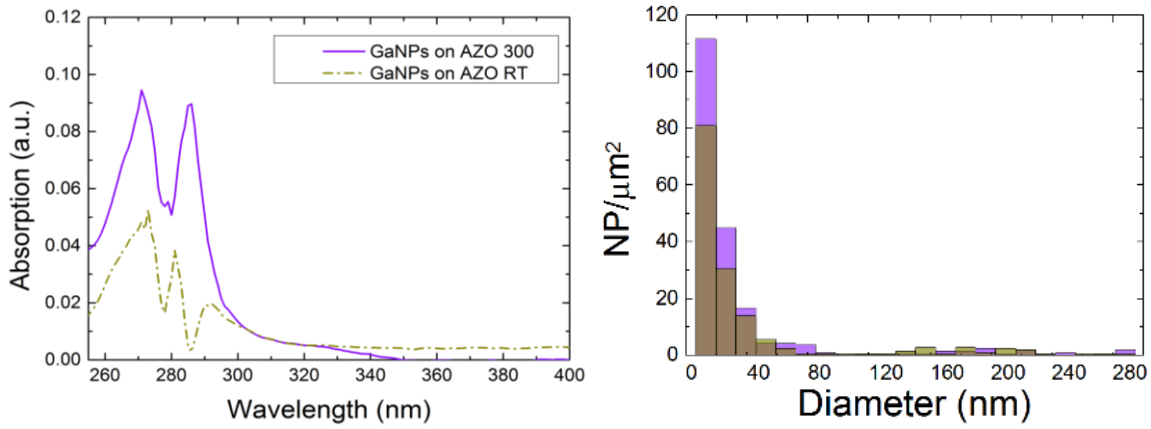


Figure 7: Absorption spectra in THF solvent. The inset plot shows the distributions of as-evaporated Ga NPs on an AZO layer deposited at RT and AZO layer deposited at 300 °C.

# 4.4 Optical characteristic of Ga NPs colloidal

## 4.4.1 Ga NPs colloidal THF solvent

The UV spectrophotometer results in Figure 9 shows the absorbance band related to the dispersed nanoparticles distribution in THF solvent. As organic solvent, it shows an absorbance cutoff wavelength at 220 nm and only the data above 250 nm were considered reliable and related to our Ga NPs colloids sample. For the sake of comparison, Ga was evaporated for 30'', 45'' and 60'' to give different NP size distribution as shown in figure 9.a, 9.b and 9.c. According to Beer-Lambert's law, the colloidal concentration will be strictly related with the spectrophotometer measured optical signal. The experimental colloidal spectrum exhibits two main absorption peaks at 273 nm and 285 nm. The peaks

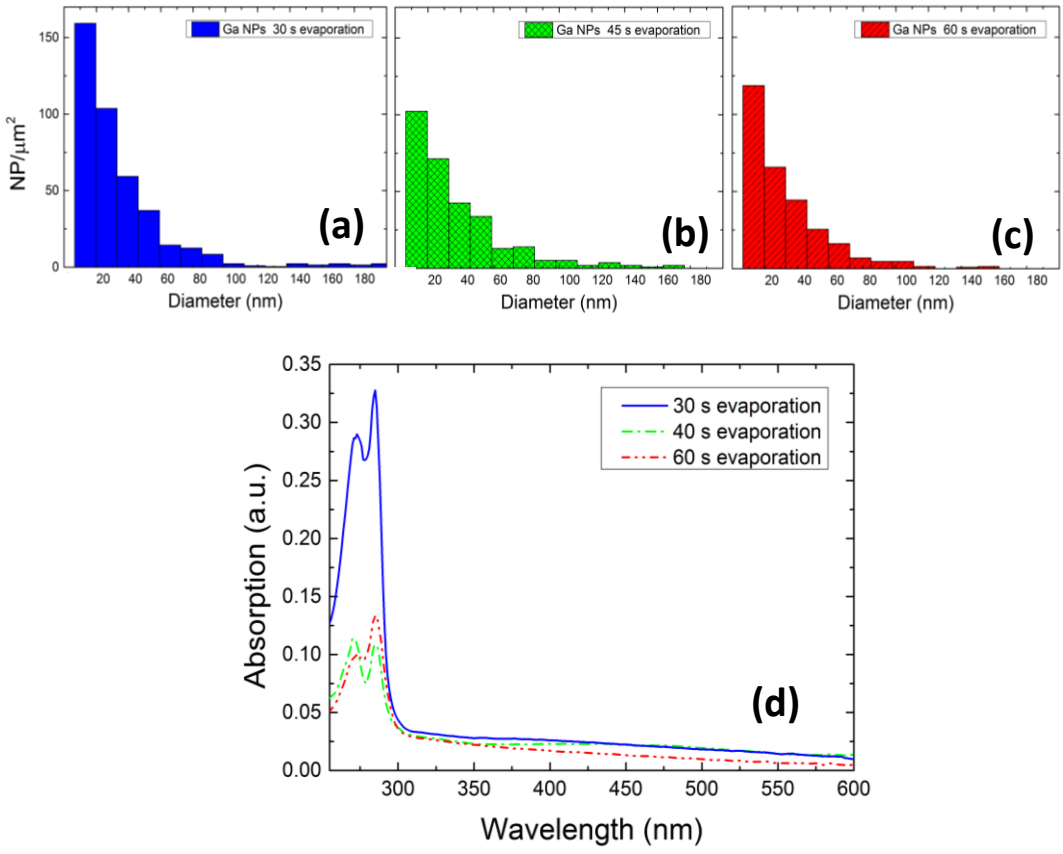


Figure 9: Ga NPs distributions for (a) 30 s, (b) 45 s and (c) 60 s evaporation time. (d) The optical absorption was measured after colloidal preparation in THF.

were found to be related with the NPs distribution, with particular relevance of diameter changes beneath 50 nm. The smaller the NP, the more they absorbs in the UV region. Thus, because of the relative NPs density, first peak on the left was ascribe to NP with a diameter of 10 nm, while the second was related to bigger NP distribution. However, it would be expected that higher density would result in bigger absorption but interestingly it does not. Regarding bigger NPs than 50 nm, their contribution was likely connected to the absorption band between 300 and 600 nm due to their low concentration.

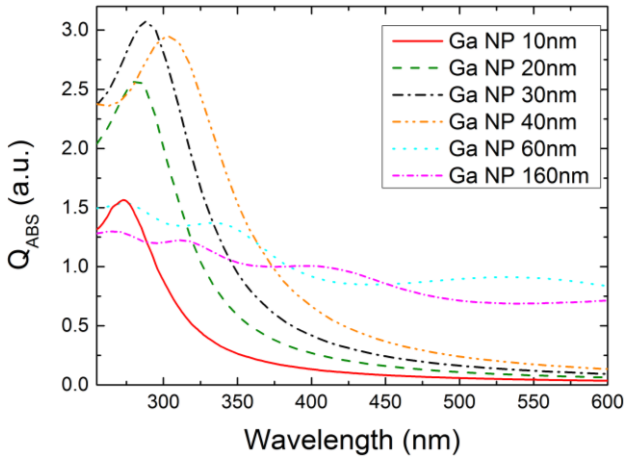


Figure 10: Numerical simulation of $Q_{ABS}$ in structures with different diameters was carried out in order to find a relationship between the measured spectra and the NPs distributions.

To investigate on the characteristics of the NP absorption, simulations by DDA method[12] were carried out in order to correlate absorption peaks with the Ga NPs size distribution for a hemisphere with 2 nm outer gallium oxide shell immersed in THF. The gallium oxide and the liquid Ga permittivities referred to Rebein et al.[13] and Knight et al.[14] works respectively, whereas solvent optical characteristic were extracted from Snyder's work.[15] The optical investigation was performed for wavelengths ranging from 255 to 800 nm. The simulations took into account a circular polarized light incident beam trying to emulate the un-polarized beam of the spectrophotometer source. Concerning the basic simulation parameters, it was used a cut-off and error tolerance value of $3 \times 10^3$ and $10^{-4}$ respectively. As shown in Figure 10, the result are expressed in terms of absorption efficiency ($Q_{ABS}$) that mainly depends on the analyzed cross-sectional area. The simulated

NP diameters ranged from 10 to 160 nm with the purpose to study the experimental as-evaporated NP size absorption behavior (figure 10). For structures with diameter longer than 60 nm a multipole oscillatory phenomena are clearly visible and multiple absorption peaks appear. Thus, it seems that experimental absorption characteristic originate from NP smaller than 60 nm as previously stated.

Finally, the narrow absorption band suggest that our colloidal likely do not flocculate in THF, remaining stable (not agglomerated) inside the solution due to the aprotic nature of the solvent.

## 4.4.2 Ga NPs colloidal in deionized water (DIW)

Before to discuss about the Ga NPs colloidal in DIW, previous consideration about the difference of the solvent nature is due. According to the double layer theory explained in Chapter 2, the thickness of the NP/liquid interface can be calculate as the reverse of the Debye-Huckel constant ($\boldsymbol{\kappa^{-1}}$). Since the ionic strength (I) is calculated as $\frac{1}{2}\sum \boldsymbol{c_i z_i^2}$, where c is the ions concentrations and z their valency, it is obvious that a protic solvent such as DIW will show higher I than an aprotic one as THF. Figure 11 is a general representation of two solvent with higher or lower ionic strength value, with the resulting shrinking of the

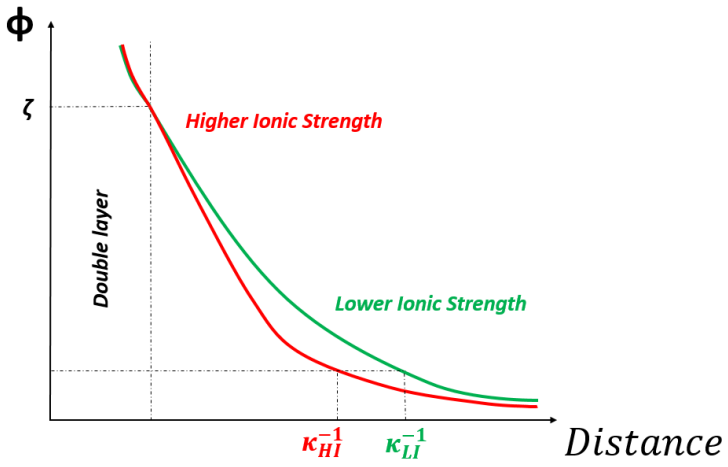


$$\kappa^{-1} = \sqrt{\frac{\varepsilon_0 \varepsilon k_B T}{e^2 2 N_A I}}$$

Figure 11: Potential representation across the double layer for NPs in a high and low ionic strength solution. The NP/liquid interface limit is expressed as the reverse of the Debye-Huckle constant $\kappa$

equivalent double layer spatial limit. The smaller the $\boldsymbol{\kappa^{-1}}$, the higher the chances for two NP to interact. Additionally, the single NP mobility (μ) in the solution can be also estimated as follows [16] :

$$\mu = \frac{2\varepsilon_0 \varepsilon \zeta \, f(\kappa r)}{3\eta} \qquad (5)$$

where ε is the permittivity of the solution, ζ is the zeta potential, f(κr) is the Henry function and η is the medium viscosity. Considering the same NP radius with equal ζ and f(κr) values, the $\mu$ value will result higher in DIW than in THF because of the difference in the permittivity. Jointly to the previous consideration on the double layer thickness in DIW, it is expected a faster NP agglomeration with an equivalent less peaked light absorption band.

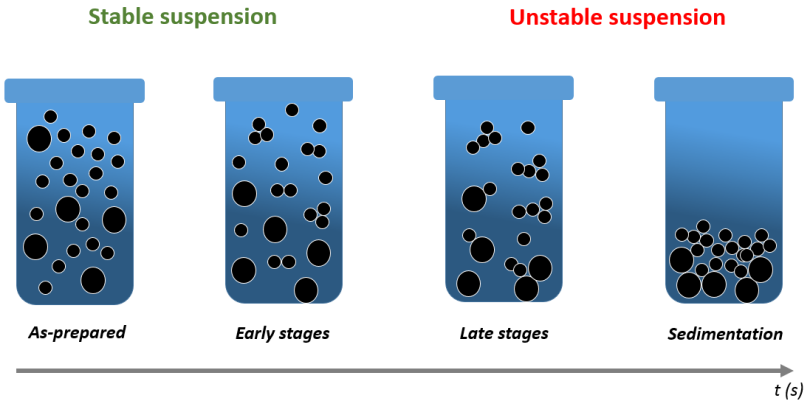


Figure 12: Colloidal configuration depending on their agglomeration status

In our case, evaporated Ga NPs with same size distribution of figure 9.a were suspended in DIW. To test the effect of different solvent ionic strength, the pH was varied ranging a value from 2.8 to 8.5. The acid/base level of the sample was adjusted carefully adding NaOH $10^{-1}$ M and HCl $10^{-1}$ M solutions with the use of a micropipette tool. According to other authors measurements [17] , the Ga Ox NPs in aqueous solution zero value of the zeta potential – the so-called point of zero charge (PZC) – can be found at a

pH level of 8.4 for particle with an average effective radius of 330 nm . Because of the native Ga Ox shell surrounding the colloidal, first analysis assumed similar PZC value.

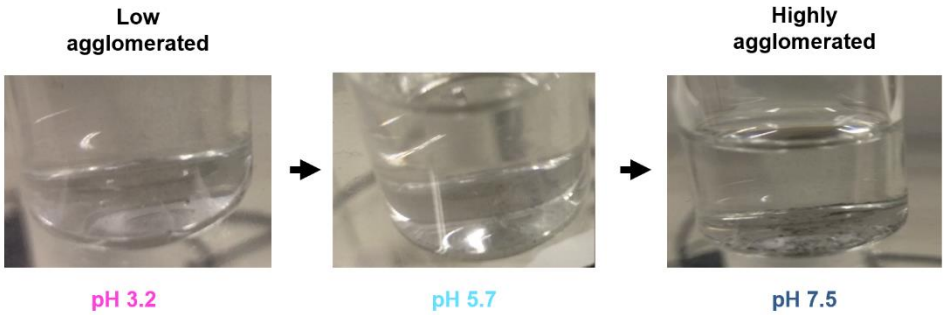


Figure 13: Agglomeration evidences during the pH changes. The closer to the PZC, the faster the big clusters sediment

Considering a NPs colloidal suspension with a no unimodal distribution, there are four possible scenarios of their agglomeration status in water medium: Stable suspension, early stages, unstable suspension and sedimentation (Figure 12). Initially, NPs starts to form dimers and trimers depending of the so-called aggregation rate coefficient (*k*). After a certain time, most of the aggregates sedimented on the bottom, depending on the cluster dimension. The closer the pH to the critical value of PZC, the bigger the aggregates

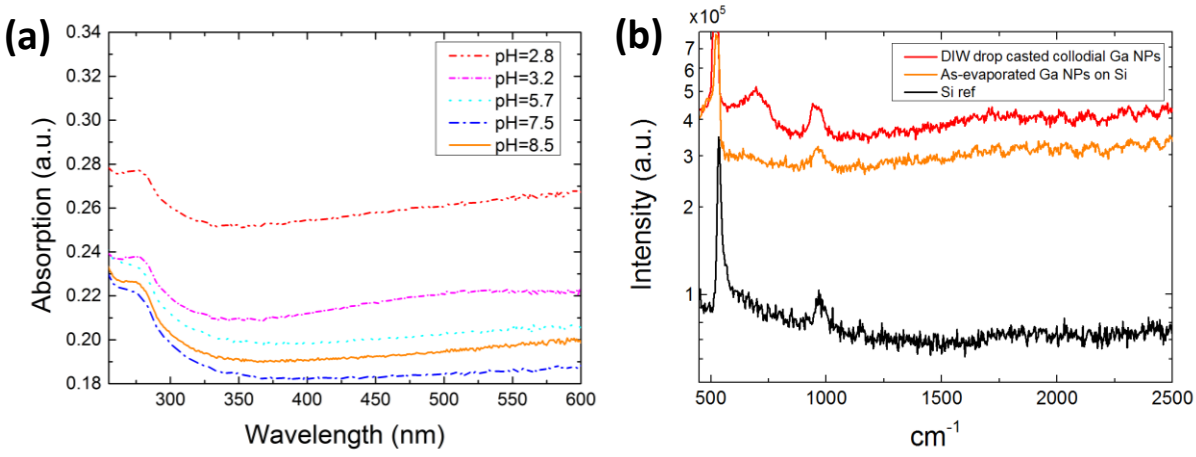


Figure 14: (a) Absorption measurements of aqueous colloidal solutions for different pH levels ranging from 2.8 to 8.5. (b) Raman shift measurement of silicon (green) and drop casted Ga NPs from DIW (red) and EtOH (blue) colloidal solutions.

in the solution, hence a faster sedimentation dynamic. This behavior was also studied for Ga NPs colloidal in different acidity solutions, where for a pH of 7.5 closer to the NPs PZC, a higher agglomeration status was observed (figure 13).

Figure 14.a shows the sample absorption at different pH value, which was related to the agglomeration status. First measurement was taken at 2.8 pH, for which low agglomerated status was expected. In this case, it was obtained the highest optical absorption due to the interaction between the laser beam and the suspended NPs. Shifting the pH level to the hypothetical PZC value, two different absorption contribution can be noted. In fact, the peak at 274 nm was related to smaller NPs of 40 nm diameter because of their higher concertation and the similarity to the previously measured absorption in THF. The rest of the absorption signal was related to bigger agglomerations at their early stage formation. Thus, raising the pH value allows clusters formation and sedimentation at the same time, which main effects are the red-shifted absorption wavelength and the absorption amplitude drop respectively. For a pH level of 7.5, colloid is highly unstable reaching the minimum measured optical absorption. At higher pH values, the colloidal seems to reach a more stable status that allows the absorption raising up again. Because of this, it is believed that PZC of Ga NPs in DIW has to be around a pH of 7.5. The shift in the PZC value is due to the smaller dimension of our colloidal compared to the one of the reference, since faster aggregation may occurs at lower pH as the NP size decrease. [8]

Further simulation on NP agglomeration evaluated Ga NPs cluster absorption curves in DIW, varying the number of the aggregated NP from 8 to 64 sphere nanoparticles.[18] The cluster were made of NP of same diameter size, which in this case were 20 and 30 nm. Previous analysis of 8 sphere cluster of bigger NPs produced a $Q_{ABS}$ signal out of the considered spectra range. According to Mie theory, when the light beam interacts with an NP cluster, it will be likely scattered than absorbed because of the bigger effective radius of the agglomeration compared to the single NP. Moreover, both $Q_{ABS}$ and $Q_{SCA}$ red-shift along the spectra and multi pole resonance effect can even take place depending of the

structures proximity. As figure 15.a shows, if more than 16 nanoparticles of 20 nm diameter agglomerate, the calculated absorption peak starts to decrease. It seems that for bigger cluster a new peak appears in the deep ultraviolet zone (end of violet curve), which is likely caused by the plasmonic resonance coupling between the NPs. Similar results were found for the 30 nm NP clusters (Figure 15.b), where 16 was the maximum number of agglomerated structure before the absorption drop off. In this case, biggest agglomeration did not show any increasing trend in the UV region of the spectra. The simulation results strengthening the hypothesis that Ga NPs colloidal in DIW flocculate depending of their zeta potential at the considered pH status. The farther the pH to the PZC, the higher the cluster number of agglomerated NPs, leading to a low colloidal absorption signal.

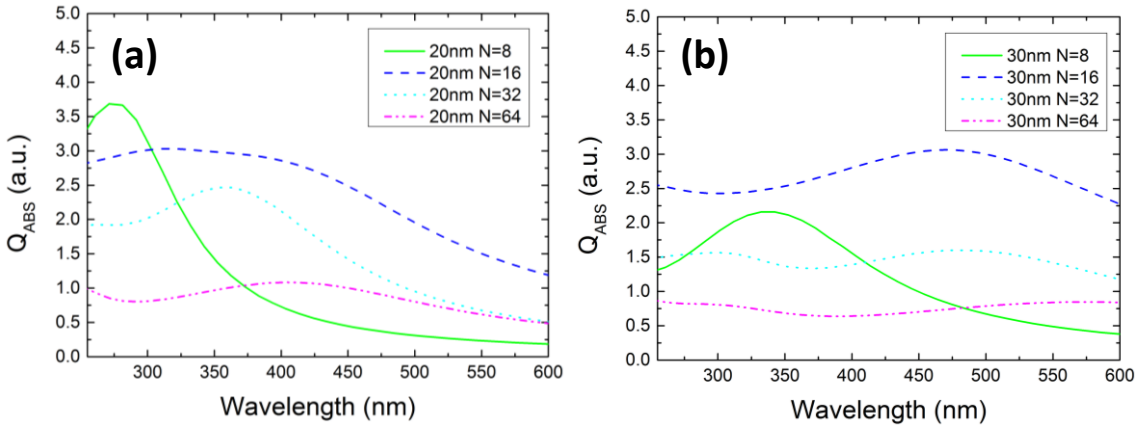


Figure 15: Results of the simulations for NPs clusters made of N number of agglomerated spheres with (a) 20 nm and (b) 30 nm in diameter size.

Finally, drop casted colloidal composition was characterize by Raman spectroscopy technique (Figure 14.b). The plot shows the two main order peak of the Silicon and a new peak appears only for the DIW colloidal sample. The peculiar peak at 695 $cm^{-1}$ could possible belong to the gallium oxide hydroxide nanoparticles shell, which is produced during the ultrasonication treatment step. [19] Thus, it is known that ultrasound can damage the particles oxide surface and increase the hydroxyl concentration by splitting the water

molecule. In that scenario, the chemical reactions during the oxide shell transformation process would be the following:

$$Ga^{3+} + 2H_2O_{(1)} \leftrightarrow GaO(OH)_{(s)} + 3H^{+}_{(aq)} \quad (5)$$

$$Ga_{(s)} + 2H_2O_{2(aq)} \rightarrow GaO(OH)_{(s)} + H \quad (6)$$

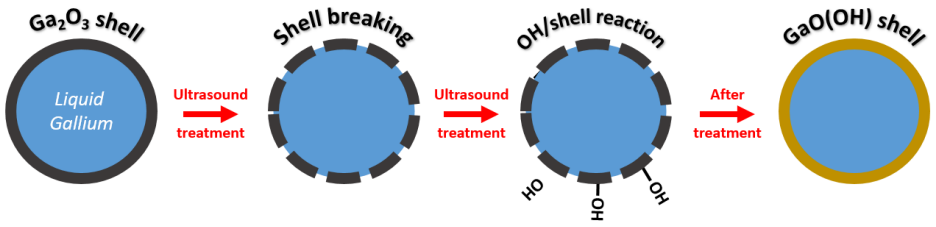


# 4.4.3 Ga NPs colloidal in ethanol (EtOH)

As previously discussed, there are several methods to assure the colloidal stability depending on the solvent and the NP material. Theoretically, when EtOH is used as colloid solvent, local polymerization around the NP could be possible. The ethanol molecules can use the NP surface as catalyst site to polymerize[20], promoting steric bonds for a higher solution stability. As shown in figure 15.a, colloidal were found completely covered by the polymerized material but it was found to crucially affect the absorption property.

The as-synthetized colloidal shows a broad absorption along the spectra (Figure 16.b), which is likely due to high proximity of the NPs in the conglomerated structure, as also seen in the DIW clustering simulations. Interestingly, the void showed at 240 nm could be related with the cluster of small Ga NP, strengthening the agglomeration hypothesis due to their less absorption contribution in that region.

Further experiment attempted to warm up the colloidal solution aiming to dissolve the undesired cover layer, freeing the NPs from their polymer cage. Using a hot plate, it was reached the EtOH boiling temperature of 78 °C during a short time of 20''. The

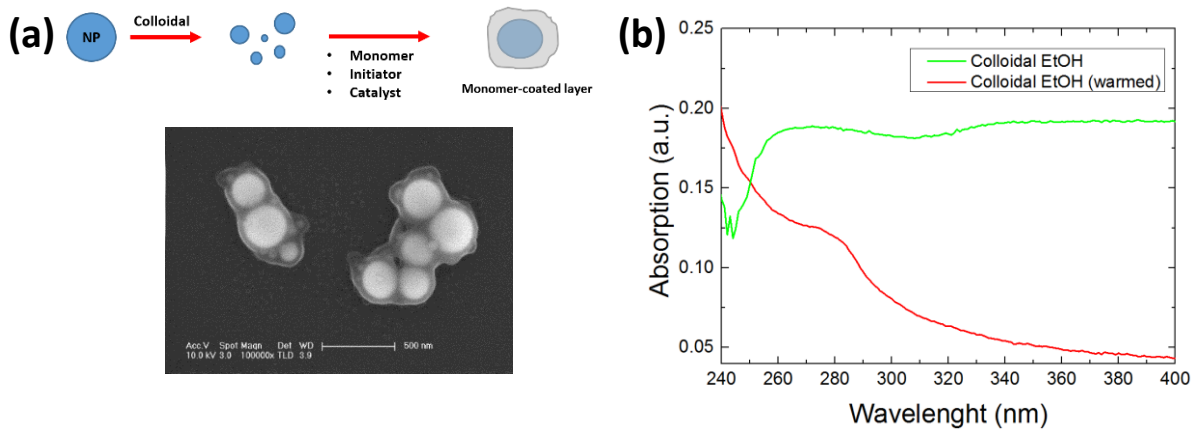


Figure 16: (a) Colloidal EtOH absorption before and after the thermal treatment with clear evidence of the agglomeration effect on the optical solution property. (b) Cover compound phenomena sketch and SEM image.

spectroscopy measurement showed a significant change of the curve with the appearance of an absorption peak at 278 nm. Previous work on solid Ga ultrasonication in isopropanol solvent[21] demonstrated the Ga NPs absorption band around 280 nm for structures with a diameter between 30 and 60 nm. Because the similarity of the chemical-optical properties between EtOH and isopropanol, we strongly support the hypothesis that smaller colloid NP mainly contribute to the rising of the observed absorption peak of the red curve in Figure 16.b. Further simulations of bigger NPs in ethanol found this structure absorbs and scatters the light out of the considered wavelength range (not shown). Compared to DIW colloidal solution, the absorption signal is reduced, even if compared to the less stable pH case. However, the experiment allowed to compared as the two polar aprotic solvents similarly affect the absorption feature depending of the colloidal agglomeration status.

# 4.5 Ga NPs colloidal plasmonic absorption study by Electron Energy Loss Spectroscopy

Previously elemental analysis discussed in section 4.3 allowed to optimize the colloidal solution synthesis, in order to achieve the highest NP dispersion due to selective etching of the chosen expendable layer. The spectroscopic results showed the absorption

property of the colloidal depending of the surrounding material but no direct evidences of the plasmonic resonance wavelength of a single Ga NP was detected. For this reason, EELS measurements were carried out using DIW colloidal solution, which was the more suitable for this purpose because of the moderated NP agglomeration status and the absence of organic rest after the drop casting. To perform the measurement, the NPs were poured on a SiN micronet to allow the electron beam passing through the sample. After several attempts, it was achieved to isolate single or small agglomeration of Ga NPs of an average dimension of 50 nm.

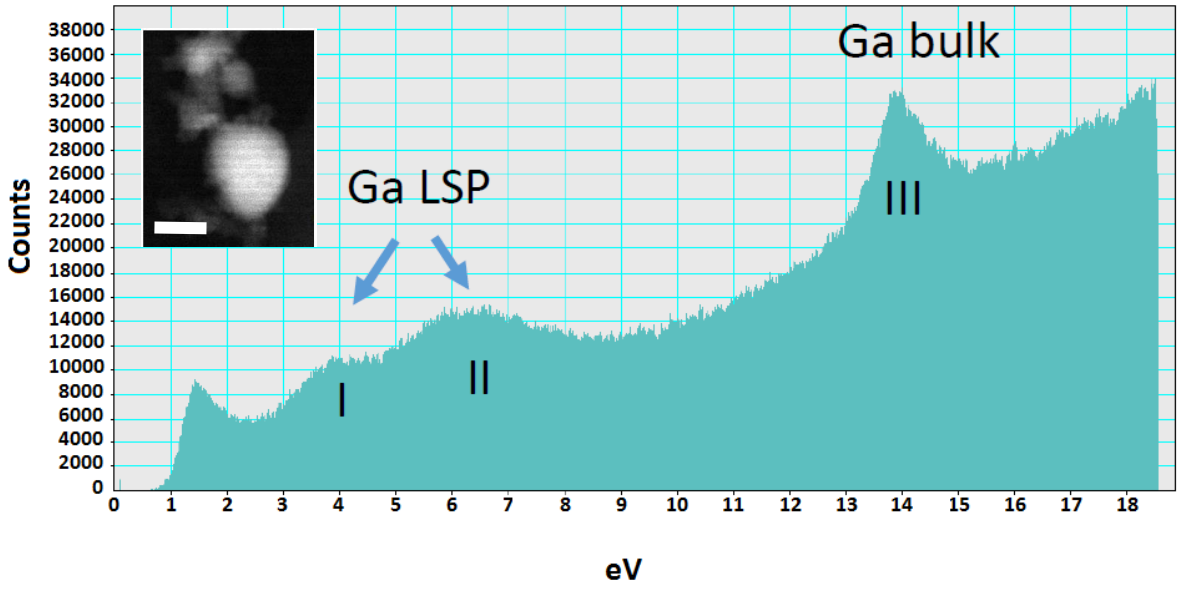


Figure 17: EELS measurements of the Ga Np showed in the inset. The surface and bulk plasmon signals are clearly displayed.

Figure 17 shows the EELS spectrum of a Ga NPs aggregation made by two structures with a diameter of about 20 nm and one of 50 nm as shown in the figure inset. At higher energy, the bulk plasmon resonance is revealed with a distinct peak at 14 eV. It was observed that no matter the NP dimension, the resonance from the oscillation of the internal localized electron always appears at the same energy range.. The energy band at which the localized absorption occurs well agrees to the measured spectroscopic absorption of Figure 10. Since the NPs do not differ too much in dimension, it was not

easy to discern the absorption contribution of every structure in the range between 3 eV and 7 eV. The first (4 eV) and second (6 eV) peak on the left have been found related with the LSP around the structure as further single NP LSP resonance analysis demonstrated.

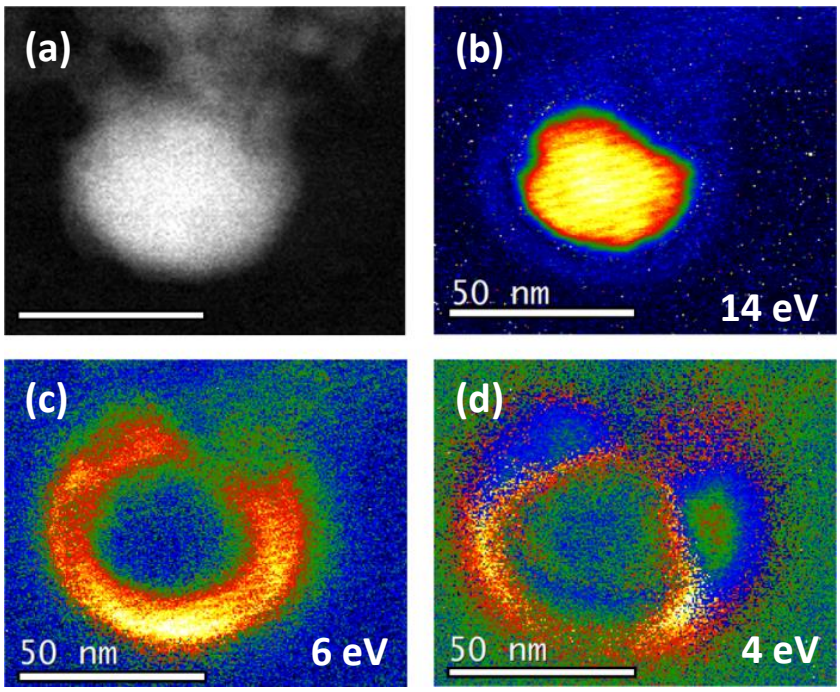


Figure 18: (a) TEM image of a single Ga NP. EELS signal intensity map at (b) 14 eV, (c) 6 eV and (d) 4 eV. Clearly the highest LSP signal was obtained for 6 eV energy (λ=206 nm), which is reasonably similar to the measured one using spectroscopy equipment.

Figure 18 shows the TEM images of a single 50 nm diameter Ga NP and its energy mapping related to its plasmonic absorption. Remarkably, the measurement showed the spatially absorption variation across the Ga NP as no previous work has done before. Every point represent the intensity of the LSP or bulk plasmon energy peak in the considered pixel. The bulk resonance image was obtained for an electron beam energy of 14 eV (figure18 .b), while LSP resonance evidences were acquired at 6 eV (figure 18 .c) and 4 eV (figure 18 .d) respectively. It is clear as bulk plasmon were excited inside the NP, while LSP signal correspond to the edge of the sphere. For the higher energy LSP at 6 eV (λ= 206 nm), the plasmon propagated intensely inside the structure for about 12 nm. At

low energy, the absorption among the structure drastically reduced and only some two lobes of the previous semicircle gave back signal.

To conclude, the measured NP absorption energy was reasonably close to the one obtained by spectroscopy equipment, attesting its plasmonic nature. The little blue shift discrepancy is likely due to the change of medium refractive index from 1.33 (DIW) to 1 (Air) during the measurement. The LSP absorption spectral broadening is caused by the NP shape irregularity and because of differences of the surrounding Ga Ox shell thicknesses. Additionally, as the NPs are not perfect spheres, it is worth to mention that the particle asymmetry and the incidence angle of the illuminating beam might result in different LSP energies.

# Conclusions

A new Ga colloidal fabrication method in polar aprotic (THF) and protic (DIW, EtOH) solution was developed. It allowed good tunability of the solution optical properties depending of the chosen solvent. The process steps were optimized to achieve higher yield jointly with the desired NPs shape and size distribution. The endurance of the Ga NP were also tested in harsh acidic environment, which opens the possibility of their implementation in the medical field such as for drug delivery application. In the case of DIW solvent, agglomeration phenomena was found to be driven by the charge accumulation around each NP and it has been controlled by changing the solution pH level. Finally, EtOH colloidal solution demonstrated the requirement of a post warming step to overcome the steric agglomeration effect due to the ultrasonic process step. High optical absorption with relative low agglomeration status was achieved in the last instance using THF solvent. For this case, the differences in the Ga NPs size distribution were related to the absorption spectra, demonstrating the role of smaller colloidal NPs and the absorption contribution. Further simulations agreed with previous statement, confirming the importance of the small colloidal NP optical absorption. To conclude, a direct

evidences of the surface and bulk plasmonic resonance of a drop casted NP were obtained. According to our knowledge, it was the first time that LSP and bulk plasmon signal were detected in a single structure with such a high spatial and energy precision. The measurements confirmed the UV absorption trend of small Ga NPs and also set the bulk plasmon activity at the 14 eV. The overall study of the colloidal optical properties will be useful for their further implementation in sensor surface modification for future applications. [22, 23] The physical synthesis by evaporation of NPs lead to higher yield compared to the common chemical methods. The colloidal properties could be also tune by changing the NPs material, their dimension and the used solvent. Nevertheless, pre-treatments for further functionalization could be exploited focusing on tuning the final colloidal optical absorption. [24]

# References


[1] D. M. Schaadt, B. Feng, and E. T. Yu, "Enhanced semiconductor optical absorption via surface plasmon excitation in metal nanoparticles", Applied Physics Letters **86** (6), 063106 (2005).

[2] Antonio García Marín, Tania García-Mendiola, Cristina Navio Bernabeu, María Jesús Hernández, Juan Piqueras, Jose Luis Pau, Félix Pariente, and Encarnación Lorenzo, "Gallium plasmonic nanoparticles for label-free DNA and single nucleotide polymorphism sensing", Nanoscale **8** (18), 9842 (2016).

[3] Yue Lu, Quanyin Hu, Yiliang Lin, Dennis B. Pacardo, Chao Wang, Wujin Sun, Frances S. Ligler, Michael D. Dickey, and Zhen Gu, "Transformable liquid-metal nanomedicine", Nature Communications **6**, 10066 (2015).

[4] Robert Taylor, Sylvain Coulombe, Todd Otanicar, Patrick Phelan, Andrey Gunawan, Wei Lv, Gary Rosengarten, Ravi Prasher, and Himanshu Tyagi, "Small particles, big impacts: A review of the diverse applications of nanofluids", Journal of Applied Physics **113** (1), 011301 (2013).

[5] Vivek Sharma, Kyoungweon Park, and Mohan Srinivasarao, "Colloidal dispersion of gold nanorods: Historical background, optical properties, seed-mediated synthesis, shape separation and self-assembly", Materials Science and Engineering: R: Reports **65** (1), 1 (2009).

[6] Kunal V. Savaji, Olivia Niitsoo, and Alexander Couzis, "Influence of particle/solid surface zeta potential on particle adsorption kinetics", Journal of Colloid and Interface Science **431**, 165 (2014).

[7] Hiroki Yotsumoto and Roe-Hoan Yoon, "Application of Extended DLVO Theory: I. Stability of Rutile Suspensions", Journal of Colloid and Interface Science **157** (2), 426 (1993).

[8] Y. Thomas He, Jiamin Wan, and Tetsu Tokunaga, "Kinetic stability of hematite nanoparticles: the effect of particle sizes", Journal of Nanoparticle Research **10** (2), 321 (2008).

[9] Shigeo Ohira and Naoki Arai, "Wet chemical etching behavior of β-Ga2O3 single crystal", physica status solidi c **5** (9), 3116 (2008).

[10] Jaehui Ahn Younghun Jung, Kwang Hyeon Baik, Donghwan Kim, Stephen J. Pearton, Fan Ren, and Jihyun Kim,, "Chemical Etch Characteristics of N-Face and Ga-Face GaN by Phosphoric Acid and Potassium Hydroxide Solutions", J. Electrochem. Soc. **159** (2), 117 (2012).

[11] J. A. Marqusee and John Ross, "Theory of Ostwald ripening: Competitive growth and its dependence on volume fraction", The Journal of Chemical Physics **80** (1), 536 (1984).

[12] Bruce T. Draine and Piotr J. Flatau, "Discrete-Dipole Approximation For Scattering Calculations", J. Opt. Soc. Am. A **11** (4), 1491 (1994).

[13] M. Rebien, W. Henrion, M. Hong, J. P. Mannaerts, and M. Fleischer, "Optical properties of gallium oxide thin films", Applied Physics Letters **81** (2), 250 (2002).

[14] Mark W. Knight, Toon Coenen, Yang Yang, Benjamin J. M. Brenny, Maria Losurdo, April S. Brown, Henry O. Everitt, and Albert Polman, "Gallium Plasmonics: Deep Subwavelength Spectroscopic Imaging of Single and Interacting Gallium Nanoparticles", ACS Nano **9** (2), 2049 (2015).

[15] Joseph J. Kirkland Lloyd R. Snyder, Joseph L. Glajch, *Practical HPLC Method Development*. (John Wiley & Sons, 2012).

[16] B. Charleux, C. Coperet, and E. Lacote, *Chemistry of Organo-hybrids: Synthesis and Characterization of Functional Nano-Objects*. (Wiley, 2015).

[17] J. N. Díaz de León, "Binary γ-Al2O3–α-Ga2O3 as supports of NiW catalysts for hydrocarbon sulfur removal", Applied Catalysis B: Environmental **181**, 524 (2016).

[18] Shen Yue, B. T. Draine, and T. Johnson Eric, "Modeling Porous Dust Grains with Ballistic Aggregates. I. Geometry and Optical Properties", The Astrophysical Journal **689** (1), 260 (2008).

[19] S. Avivi, Y. Mastai, G. Hodes, and A. Gedanken, "Sonochemical Hydrolysis of Ga3+ Ions: Synthesis of Scroll-like Cylindrical Nanoparticles of Gallium Oxide Hydroxide", Journal of the American Chemical Society **121** (17), 4196 (1999).

[20] Chin Ming Hui, Joanna Pietrasik, Michael Schmitt, Clare Mahoney, Jihoon Choi, Michael R. Bockstaller, and Krzysztof Matyjaszewski, "Surface-Initiated Polymerization as an Enabling Tool for Multifunctional (Nano-)Engineered Hybrid Materials", Chemistry of Materials **26** (1), 745 (2014).

[21] Akihisa Yamaguchi, Yu Mashima, and Tomokazu Iyoda, "Reversible Size Control of Liquid-Metal Nanoparticles under Ultrasonication", Angewandte Chemie International Edition **54** (43), 12809 (2015).

[22] Shuwen Zeng, Dominique Baillargeat, Ho-Pui Ho, and Ken-Tye Yong, "Nanomaterials enhanced surface plasmon resonance for biological and chemical sensing applications", Chemical Society Reviews **43** (10), 3426 (2014).

[23] Jyh-Lih Wu, Fang-Chung Chen, Yu-Sheng Hsiao, Fan-Ching Chien, Peilin Chen, Chun-Hong Kuo, Michael H. Huang, and Chain-Shu Hsu, "Surface Plasmonic Effects of Metallic Nanoparticles on the Performance of Polymer Bulk Heterojunction Solar Cells", ACS Nano **5** (2), 959 (2011).

[24] Zhong Li, Lisa A. Fredin, Pratyush Tewari, Sara A. DiBenedetto, Michael T. Lanagan, Mark A. Ratner, and Tobin J. Marks, "In Situ Catalytic Encapsulation of Core-Shell Nanoparticles Having Variable Shell Thickness: Dielectric and Energy Storage Properties of High-Permittivity Metal Oxide Nanocomposites", Chemistry of Materials **22** (18), 5154 (2010).

# Chapter 5
# Plasma and chemical treatment of Ga NP arrays

In the last decades, nanostructures have been widely used to modify material properties such as absorption, reflection and scattering. Gallium nanoparticles (Ga NPs) are made of a liquid gallium (Galiq) surrounded by a thin native oxide shell. It has been demonstrated that thermal process can vary the NP outer shell as much as the process time lasts. Samples were made with thermally evaporated Ga NPs on Si for different evaporation times. The used NP range from 10 to 1000 nm in diameter allowing most of the compositional, morphological and optical analysis. Two different approaches have been used to change the surface morphology of Ga NP coverage. First, the effectiveness of plasma oxygen sputtering to shape Ga NPs is discussed. Previous simulation of sputtering oxygen ions on gallium surface allowed to determine reasonable processes powers, which were used for different NP size. Remarkable control of the NP surface coverage and size distribution was achieved. The Ga NP were shaped in height/radius ratio (h/d) and their contact angles with the substrate, also achieving Ga nanocones (NCs) structures. The changes enhance the light absorption of the sample depending on the etching time and powers. Further plasma etching with $O_2/CHF_3$ gases allowed black silicon formation for visible light high absorption sample. In this case, NP acts as a hard mask while the oxyfluoride ion etches the surface. To conclude, chemical wet etching method with $HP_4O_3$ and HCl acids was investigated to control successfully the Ga NP surface distribution.

## 5.1 Plasma Treatment

## 5.1.1 $O_2$ plasma RIE: time and power dependency

The resultant morphology of the RIE modification will depend on two main process parameters: time and power. The tuning of these two are strictly related with the starting NP dimension and the desired nanocones aspect ratio. Small structure cannot endure under high power process, while bigger ones could not be affected by incident low energy ions.

Let us considered three possible cases for a heavy oxygen ion impinging on the NP oxide surface. If the ion does not achieve to have enough energy to displace any Ga atom, it will be scattered away, with no effect on the NP. In the case that an oxygen ion has enough energy to move Ga atoms from the lattice, sputtering process will occur. Furthermore, the incident ion can be implanted through the oxide shell to bond with the $Ga_{liq}$ beneath to create new inner Ga oxide layer. As time passes the sputtering process begins to etch the NP decreasing the native oxide value and shaping the NP to nanocones. The effect of oxygen ion erosion on gallium surface has been investigated with simulations using SRIM software [1]. This tool allows to calculate the stopping and range of an ion into matter varying several parameters such as power and incidence angle. In order to simulate the number of the target sputtered atoms during each ion impact, the so called sputtering yield (SY), the target density value is needed.

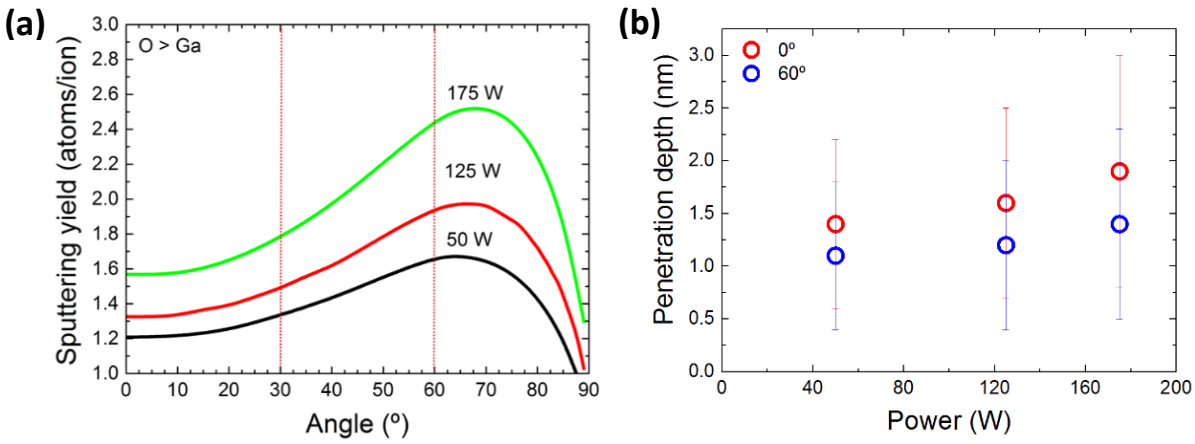


*Figure 1: SRIM sputtering simulations of Oxygen ion impinging on Ga. (a) The ion penetration depth calculation showed low power and angle dependency. (b) On the contrary, sputtering yield strongly depend on process parameters.*

Unfortunately, the density of a native gallium oxide shell around the particle has not been calculated until now and same as in other works, the bulk liquid gallium value has been used instead. The simulated power were the same allowed by the used RIE system and they have been particularly selected to study the shape modification for different NP dimension. As previously said, the material plasma etching will physically and chemically interact with the NP material, presumably changing its shape and composition. The number of sputtered target atoms after each ion impact - the so called Sputtering Yield (SY) – has been largely studied from Yamamura et al [2], demonstrating a $\frac{1}{\cos(\theta)}$ proportional dependence with the ion incidence angle $\theta$ on the surface.

Figure 1.a shows the simulated SY angle dependence with clear differences in terms of yield between the three curves at fixed incidence ion angle. According to the simulations, the SY is maximum near 65°, which means that the lateral side of the NP will be etched faster than the top. Nevertheless, the ion penetration depth (Figure 1.b) into the material has been found barely affected from the incidence angle parameter and almost independent on the treatments powers. Therefore, a new inner oxide growth layer can be produced due to the oxygen average penetration depth of similar thickness to the native GaOx shell thickness.

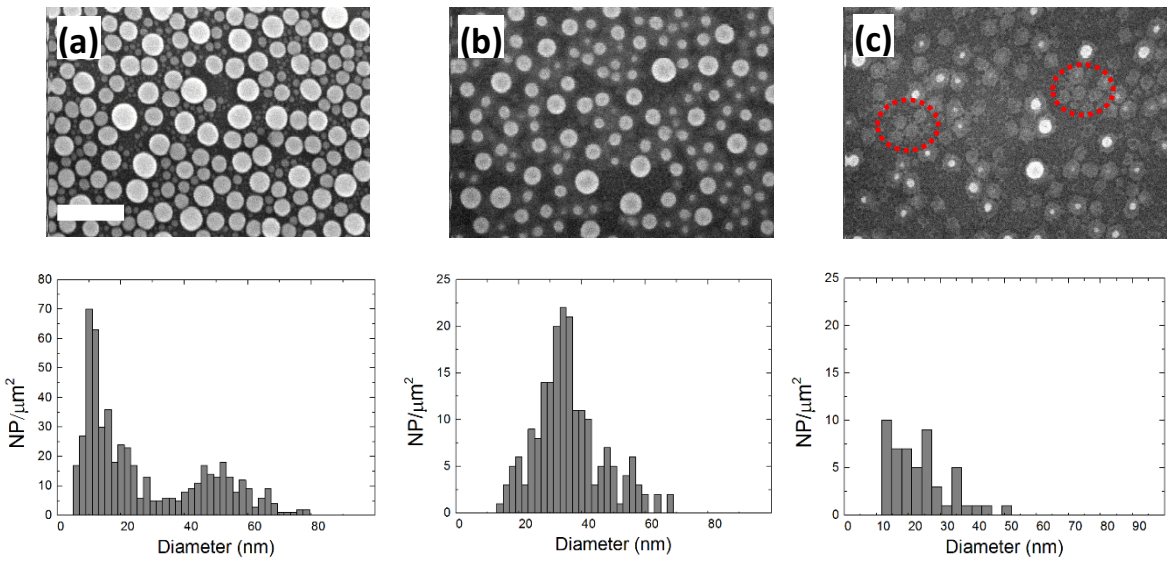


*Figure 2: SEM images of 50W process at (a) as-evaporated, (b) 15' and (c) 30' time steps. Scale bar corresponds to 200 nm. The related surface coverage value are 80%, 43% and 3% respectively, while the NP size distribution are the ones shown below. The red dashed circles highlight the presence of unrecognized material plates.*

Samples with an average NP diameter of less than 100 nm were grown to study the effect of low energy process. Figure 2 shows the sample SEM images after 50W treatment for as-evaporated, 10' and 30' time step. The equivalent NP dimeter histograms (not shown) shows a narrowing of the size distribution also related to a change of the percentage surface coverage from 80% (as-evaporated) to 3% (30'). The process time affects the optical surface property as shown from elipsometry measurements later on.

After long time processes, unusual surface plates were observed (Figure 2.c red dashed circles). The plates change the surface morphology and could have a role in tuning the sample optical properties. To investigate the nature of these areas different microscopy techniques were used, such as atomic force microscopy (AFM) and Kelvin probe force microscopy (KPFM). By means of AFM it was measured an average plate height of 1.5 nm. The plate could originate from the selective etching of the Silicon substrate, but it has been demonstrated that low energy $O_2$ plasma is ineffectiveness to damage the Si surface during short time [3]. To further investigate the origin of the plates, KPFM provided insight about the surface work functions potential (W) value in order to detect material compositional differences across the sample. The work function can be defined as the energy needed to move an electron from the occupied energy level (Fermi level) out of the material (vacuum level). It can be calculated from the following equation:

$$V_{CPD} = \frac{(\mathrm{W}_{sample} - \mathrm{W}_{tip})}{e} \qquad [1]$$

where the $V_{CPD}$ is the contact potential difference, $\mathrm{W}_{sample}$ is the sample work function, $\mathrm{W}_{tip}$ is the tip work function and $e$ is the elementary charge value. The measurement was carried out using a Pt/Ir tip, which has a work function value of 5.4 eV.

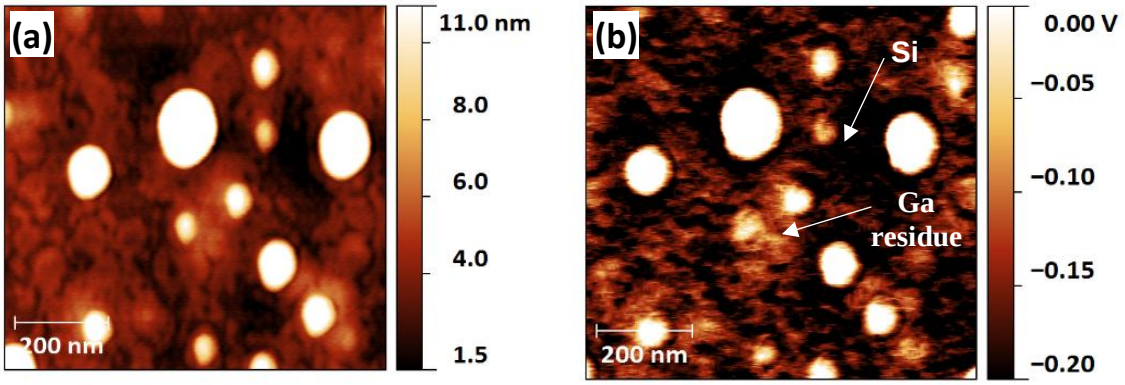


*Figure 3: Surface images of a 30' etch taken with different microscopy techniques. (a) AFM analysis revealed the surface morphology. (b) Further KPFM measurement demonstrated that plates are not made of the same substrate material, which allows to discard substrate damaging issue during the process*

Considering the $Ga_2O_3$ (4.9 eV) [4] and Si (4.9 eV) [5] work functions, it would be theoretically not possible to distinguish the oxide and substrate in terms of potential difference. Nevertheless, figure 3.b shows that the regions with a larger measured potential match the NP position. The plates also show higher potential than the beneath substrate. We speculated that plates are likely made of GaOX but with higher potential in comparison to $Ga_2O_3$ due to their extremely thin dimension (between 0.5 and 4 nm). The work function value for such a small quantity of material can differ up to some electron-volts value from the bulk[3]. Then, the plates might be generated from the NPs oxidation after RIE process ruling out substrate damaging issue during the process.

Later, ellipsometry measurements of all the 50W time steps were carried out (Figure 4). The obtained imaginary part of the pseudo-dielectric permittivity allowed to correlate the RIE surface modification with changes in the sample optical absorption. The intensity gradually increase until the Ga NP signal disappear, revealing for the beneath silicon signal (yellow line). As the etching time goes by, the as-evaporated absorption peak blue-shifts from 495nm to 350 nm. The shift is due to a reduction of the average NP radius from 40 nm to 20 nm as size histograms confirmed. The NP peak tuning can be exploited in applications where particular coupling with functional monolayer absorption such as in DNA chains or self-assembled structures especially in the bio sensing field [6,7].

Further experiments at 125 W and 175 W on NP with diameter smaller than 100 nm diameter were carried out but the power was too high for such a small structure. The SEM and elipsometry measurements evidenced a complete erosion presenting the bare substrate silicon signal after 6'. In order to further investigate the surface modification of

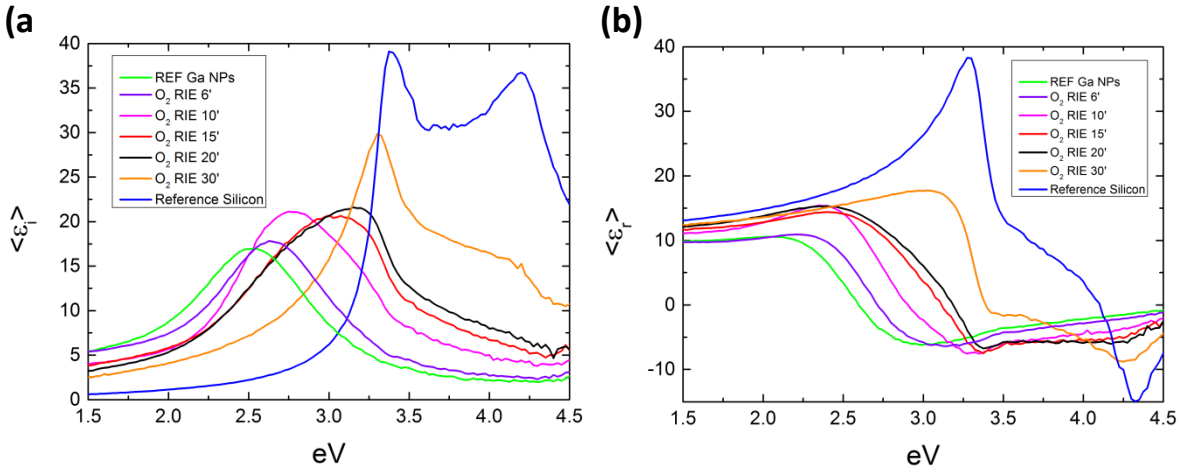


*Figure 4: Elipsometry measurements of the (a) imaginary and (b) real part of the pseudo-electric permittivity function.*

Ga NP coatings, NPs with diameters larger than 100 nm were thermally evaporated. The process has been carried out at 50 W, 125 W and 175 W power, with an equivalent ion energy of 0.3 KeV, 0.5 KeV and 0.7 KeV respectively. The etching time steps were intentionally selected from 2 minutes to 30 minutes to avoid premature NP complete erosion.

Figure 5 shows the cross-sectional images of the samples at four different time steps. For all the samples, the initial NP surface coverage was 79% with an average height of 70 nm and an average radius of 60 nm. As the etching process progress, the NP shape changes to a nanocone geometry due to the effect of the plasma and the dependence of the SY function on the incident angle along the NP surface. After 20' of 50 W process, the nanocone lateral surface forms an angle with the substrate interface – the so called contact angle - of around 45° with a remarkable decrease of the surface coverage to 45%. The lowest sputtering power results in highly homogeneous erosion around the NP shell, with a modification of the average radius from 60 nm to 55 nm and a decrease of the

average height from 70 nm to 55 nm. For the 125 W process, nanocones structures ware achieved with an etching time between 6’ and 10’. After that time, the cone shape seems to be compromised with large roughening of the NP surface. In this power case, the optimized nanocone structure was achieved after 4’ etching (not shown) with a surface coverage value of 40%. The contact angle, average height and radius of the NP remained the same as in the previous 50 W case. Regarding the 175W process, similar results to the 125 W process were obtained but with a maximum etching time of 6’.

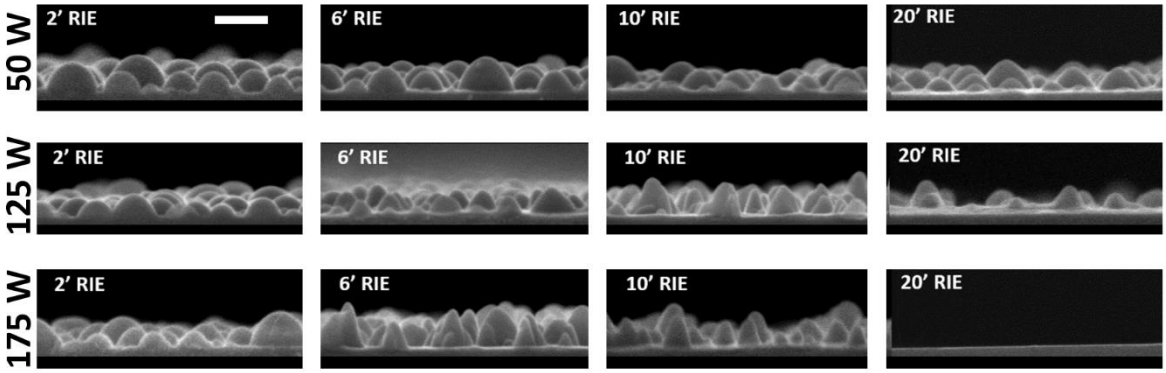


*Figure 5: Cross-sectional images of NP samples at different etching times (As-evaporated, 2’, 6’, 10’ and 20’) for 50 W, 125 W and 175 W plasma powers. Scale bar corresponds to 200 nm.*

In order to analyze the NP reshaping process, the relationship between the sputtering time and the height/diameter (h/d) ratio was calculated (Figure 6.a). The maximum values correspond to the highest aspect ratio. For the 125W and 175W the nanocones formation time is 6’ and 10’, respectively. After that time, the entire structure quickly disappears. During the 50W process, the overall h/d ratio slowly tends to decrease from 0.65 to 0.4 as the cone height is reduced.

At 50 W, the nanocones shape appears between 10’ and 20’, while longer plasma exposition (30’) results in a cone height reduction maintaining similar average radius value of 55 nm. Reaching the optimize nanocone geometry does not imply any modification of the hemisphere original h/d ratio but a change of the NP contact angle as shown in figure 6.b. Once fixed the power, there will be a critical time where cone shape appears after which the nanocones start to deteriorate until its complete erosion.

Interestingly, the higher power (125 W and 175 W) treated NPs increase their height after a lapse of time.

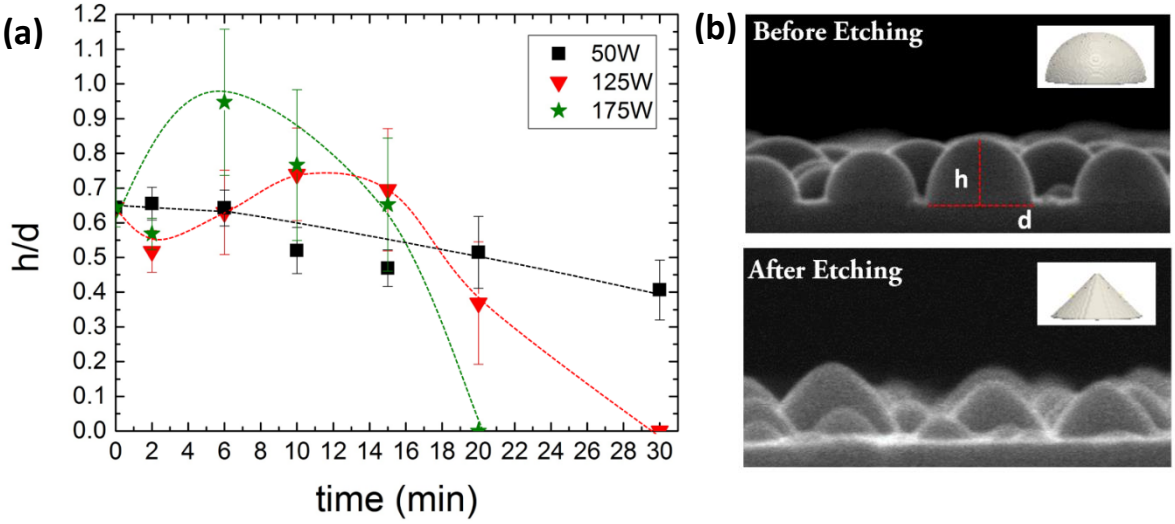


*Figure 6: (a) The h/d values as function of the etching times. The zero value represents the limit time after while the NP geometry is lost. (b)Before and after etching reshape of the NP.*

To understand the material modification during the plasma treatment, the crystal structure of the sample has been analyzed by grazing incidence X-ray diffraction technique (GIXRD). It was used a X'Pert Pro Panalytical system with Cu X-ray tube as source and collimated light in a Soller slit (0.04 rad). The output signal was detected by means of a Xe gas scintillator with fixed incidence angle of 0.5°, 2θ angle varied from 10° to 90° with 0.04° step and an acquisition time of 4 s analyzed. Samples were etched at 50 W and 100 W powers both for 20 minutes. The measurements were compared to $\Upsilon$ Ga solid reference [8], which has been demonstrated to match reasonably well the Galiq x-ray scan [9]. Thus, the as-evaporated sample peaks at 35° and 45° following the most intense diffraction lines of the solid Ga. This behavior is due to the Galiq presence inside the NP as reported before [10]. Regarding the treated samples (blue and orange line), the band gradually disappear suggesting that most of the material has been turned into oxide. The low presence of GaOx material does not provide a clear diffraction pattern in the system.

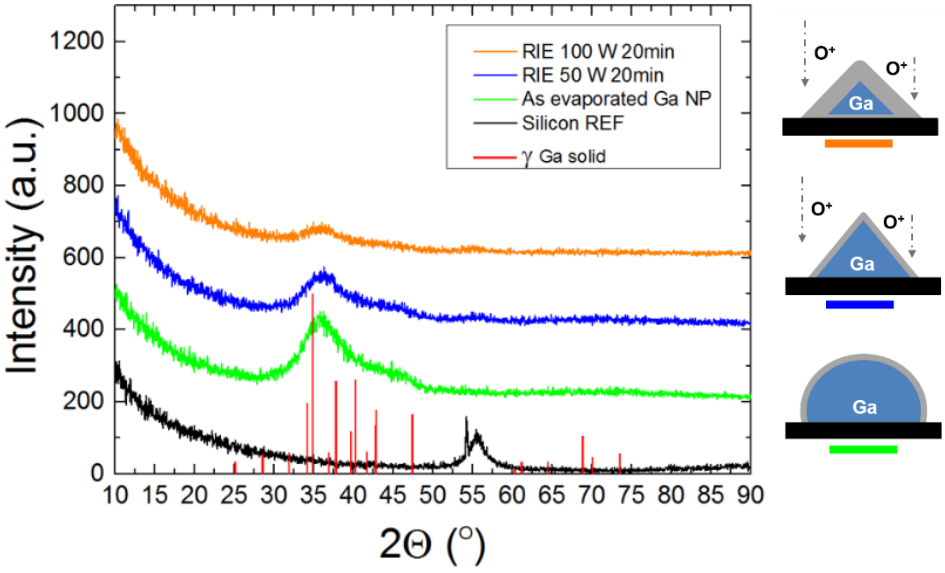


*Figure 7: X-Ray scans of samples treated at different powers during 20' in comparison to silicon substrate diffraction pattern. The diffraction lines for Y- Ga are also provided as obtained from the International centre for diffraction data*

In order to better control the Ga nanocones fabrication process, the reshaping mechanism has been further investigated. As in the smaller NP case for high powers, the structure height increases over the as-grown value. Figure 8 shows cross-sectional images of treated samples at different sputtering powers for 20 minutes. As the power increases, the shape changes from hemispherical (as evaporated) to rough corrugated structure (175 W process), with an equivalent increment of the height. The NP morphology for 125 W treatment shows uncommon asperities that mostly pop up on the upper part of the structure.

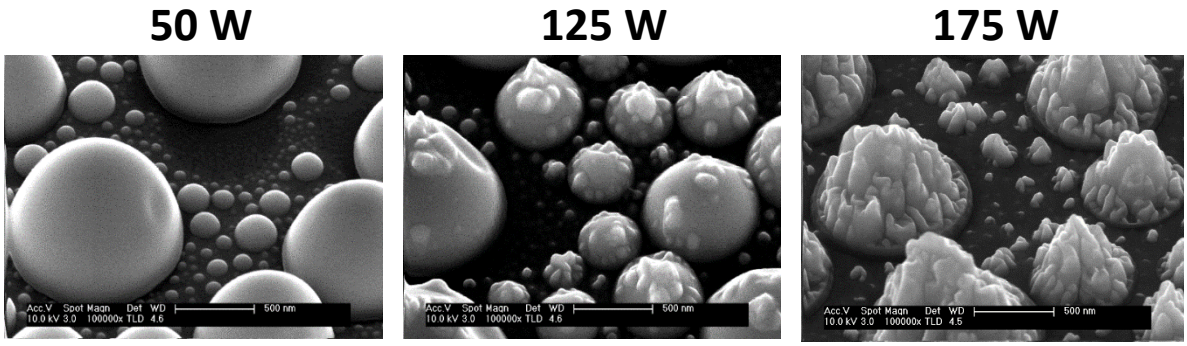


*Figure 8: Tilted 40° SEM images of the 50W, 125W and 175W processes for 20'.*

From tilted images of 50 W and 75 W samples (Figure 6.b), unusual dip appeared on the NPs surface. This phenomena was observed also from other authors during thermal modification of Ga NPs after oxygen thermal treatment above 200 C° [10], which gives an idea of the raised local temperature during the plasma etching. During the treatment, the temperature gradient and the difference in atomic concentration activate diffusion mass, as well as the vacancies, at the NP inner interface. This process, also known as Kirkendall diffusion effect [11], was study to refer to nonreciprocal mutual diffusion at the metal alloys interface but recently it has been largely used to explain hallow formation in core-shell NP compound systems [12,13,14].

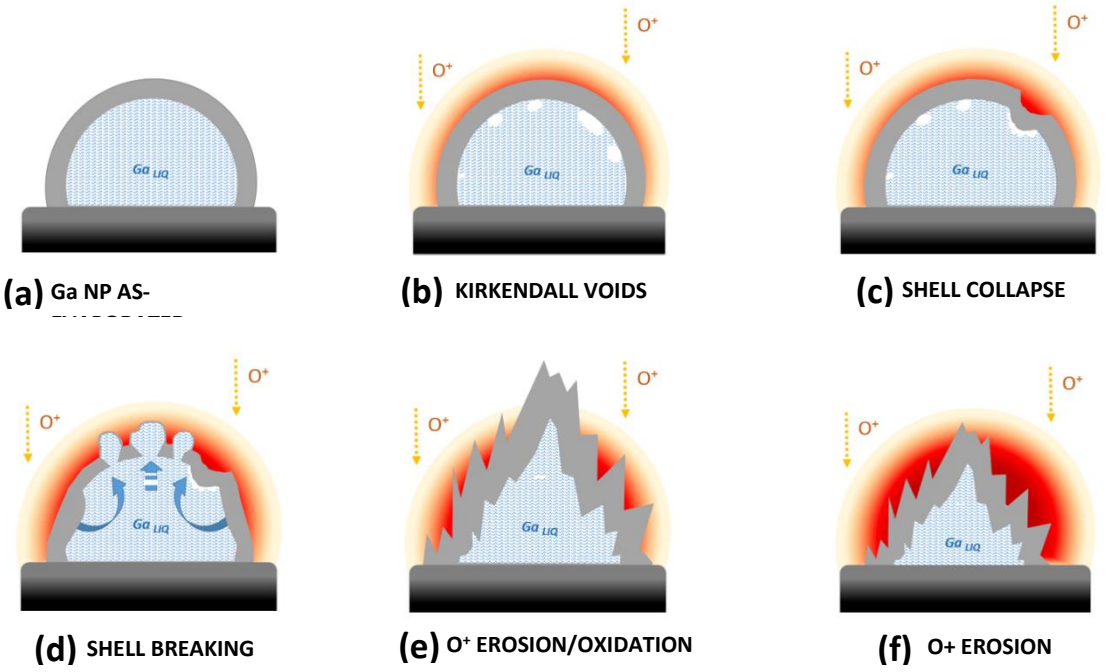


*Figure 9: Ga nanocone formation model*

During oxidation, nitridation or sulfidation dynamics, the outward diffusion of core material can be faster than the inward of the shell leading to higher probability of the excess vacancies accumulation. Once that the void is formed, the outer shell likely collapse because the change of the pressure vector direction between $P_{IN}$ and $P_{OUT}$ (Figure 9.c). The formed vacancies can bring to a tensile stress generation in the oxide leading to plastic deformation of the surrounding shell.

From figure 8, notice that dome collapse seems to occur only for bigger NP, while smaller ones keeps the hemispherical shape. The NP measured curvature slope changes as a consequence of the different etching rate of the hemispherical structure. The difference in top and side SY shown in figure 1 results in higher lateral erosion of the native oxide shell. Interestingly, the contact angle is close to angle where the SY is maximized in the simulations. Because of the new formed oxide, the liquid inside will increase the internal pressure on the dome surface until breaking it and leaking out of the core (Figure 9.d). As long as the material comes out, it slowly begins to oxidize forming a wrinkled structure a preferential growth in the vertical direction of the oxide grains (Figure 9.e).

## 5.1.2 Optical properties of Ga nanocones

Spectroscopy Ellipsometry (SE) measurements have been use to correlate each sputtering process with the imaginary pseudo-electric permittivity (Figure 10.a). The nanocone structures showed an enhancement of the absorption compared to the untreated sample (blue line). The resonance peak is due to the excitation of the plasmonic longitudinal mode (in-plane), which is detectable for our SE system. The sudden increase of the Ga NPs reference spectra towards the deep ultraviolet (UV) region was attributed to the transversal mode (out-of-plane) resonance of the sample. During the etching process, smaller NPs will drastically change their size in terms of h/d ratio, while bigger structure will be less affected. Figure 10.a shows the pseudo-electric permittivity of the time optimized structure for each time. It means that each sample show best nanocone reshaped NP before forming wrinkled structure due to over etching. For the 175 W curve, the nanocones were not completely formed and similar signal to the untreated sample was measured. For the 50 W and 125 W nanocones samples, the resonances blue-shift from 740 nm (blue line) to 700 nm (red line) due to a decrease of the NPs average radius from 60 nm to 55 nm. As time passes, the NPs peak disappear giving rise to the beneath silicon absorption band at 400 nm wavelength (orange line).

A more extended study of the Ga nanocone optical properties has been carried out with the use of discrete dipole approximation (DDA) FORTRAN code implemented by DDSCAT software [15]. The simulated structures design was based on the SEM images of the optimal etching times of each process. The advantage of using DDA simulation lays on the possibility to solve Maxwell equations in geometrical complex structures, with a precise determination of the scattering (Qsca), absorption (Qabs) and extinction (Qext) coefficients. Previous elipsometry measurements showed an increase of the pseudo imaginary permittivity (<εi>) compared to the untreated sample.

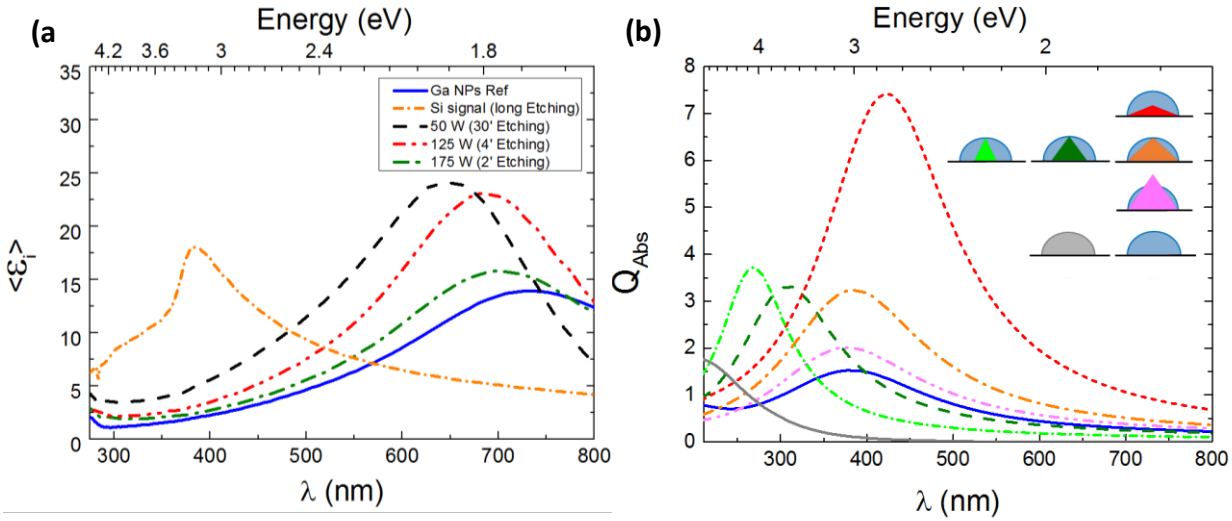


*Figure 10: (a) Elipsometry effective permittivity measurements of the nanocones optimized structures. Treated NPs absorption increased compared to as-evaporated sample (blue line). (b) DDA simulations of different nanocones aspect ratio.*

As long as the NP shape changes, the plasmonic resonance shifts and intensity changes due to a reduction of the effective radius of simulation (Figure 10.b). For fixed radius, as long as the cone height decrease, the absorption coefficient intensity significantly increases (orange and green curves). The smaller the h/d, the higher the Qabs value. Simulation of structures made of only $Ga_2O_3$ were also run (grey curve). In this case, a lower Qabs was obtained at ultraviolet wavelength with no dependence on the geometry. No matter which the h/d ratio is, the Qabs of the oxide structure remains unvaried. Simulation results agree with experimental data, where resonant peaks shift and increase value depending on the nanocone aspect ratio.

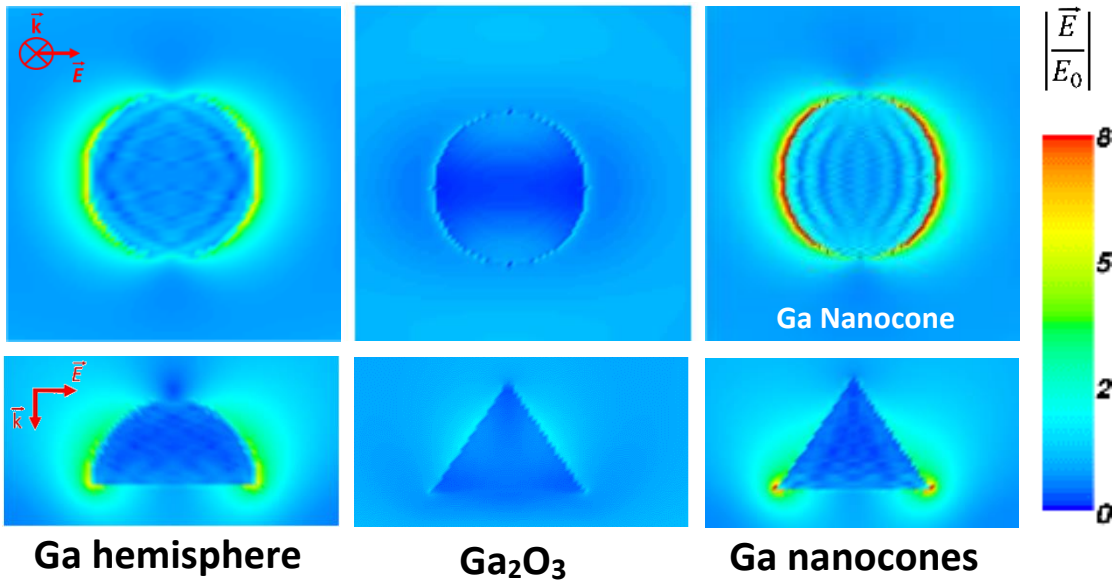


*Figure 11: Near-field calculation at λ=400nm on the x-y plane confirmed the nanocone higher surface field enhancement compared to Ga NP as-evaporated hemisphere structure.*

Previous results predicted the far-field structures absorption and scattering behavior for an incident polarized light. For application where strong interaction between the NP and functionalized layer is needed, the near-field analysis may help to optimize the geometry of the propose structure. Simulations were run for an incident field along the Z axes (from the top to base of the NP), so that the in-plane mode (parallel to the substrate) will be excited as in the SE measurements (Figure 11). By the change of the nanocone aspect ratio allows to focus the absorbed impinging field primarily at the sharp tip zone, leading to an enhancement of the absorbance intensity. Compared to the hemispherical NP, the nanocone contact angle with the substrate will be higher (sharp edges) with higher optical field concentration around the structure. Simulation confirmed that no plasmonic resonance occurs for the oxide structure.

## 5.1.3 $CHF_3/O_2$ plasma RIE

The use of trifluoromethane ($CHF_3$) with $O_2$ in the RIE processes has been largely used for Si surface modification to transfer pattern by means of a previous deposition of a hard mask. The anisotropic etching characteristic allows the formation of large aspect ratio

structures such as silicon nanopilars, also known as black silicon. [16] The surface modification is mainly used to lower the light reflection and to change the wettability of the surface for ARC and self-cleaning applications.[17, 18] In this work, Ga NPs have been used as a hard mask to produce Si nanocolumns (SiNCs) of different shape depending on the gases flow and the process time. The developed structures were further optically characterized by ellipsometry technique, where the highest nanocolumns showed low reflection properties in the visible range and small differences between both polarization components upon reflection on the nanostructured surface.

In the experiments conducted to fabricate Si nanocolumns through the use of $CHF_3/O_2$, several runs were carried out to find the right gas flow ratio for a fixed plasma power of 50 W. Firstly, pure $CHF_3$ (25 sccm) was used in order to get nanocolumns structure. This approach was found unsuccessful and SEM analysis revealed the formation of a homogeneous blurring surface layer that we hypothesized that might be related to local gas polymerization. The polymer-forming rises from the carbon and fluorine bond using the NP as catalyzing surface.[19] Adding a small quantity of $O_2$ (5 sccm) avoid the polymer layer formation and allows the SiNCs formation due to the synergetic mechanism of the supplied gases (Figure 12). Once the plasma is formed, the fluorine radicals etch the silicon oxide while oxygen radicals passivate the dangling bonds of the bare Si surface with $SiO_xF_y$ compound.[20] At the same time, the $CF_x^+$ ions anisotropically etch the new $SiO_xF_y$

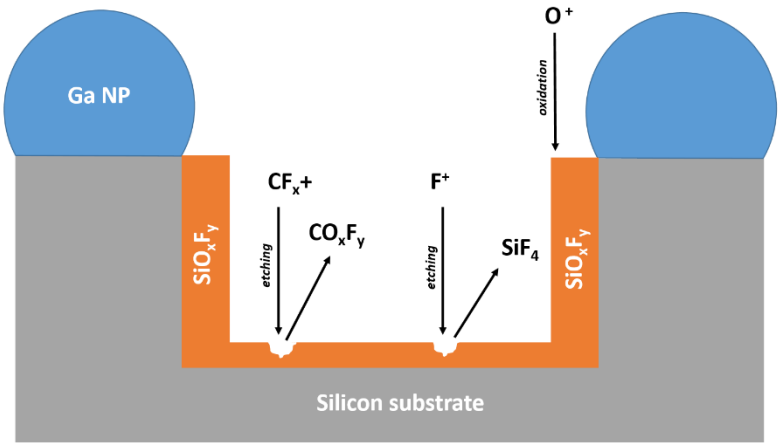


*Figure 12: Chemistry of the SiNCs formation during the $CHF_3/O_2$ plasma etching*

layer shaping the nanocolumns and producing the volatile $CO_xF_y$. Furthermore, Ga NPs size also decreases during the etching process due to the chemical and physical effect of both $O^+$ and $CF^+$ ions as discussed in Section 5.1 and a preliminary work.[21]

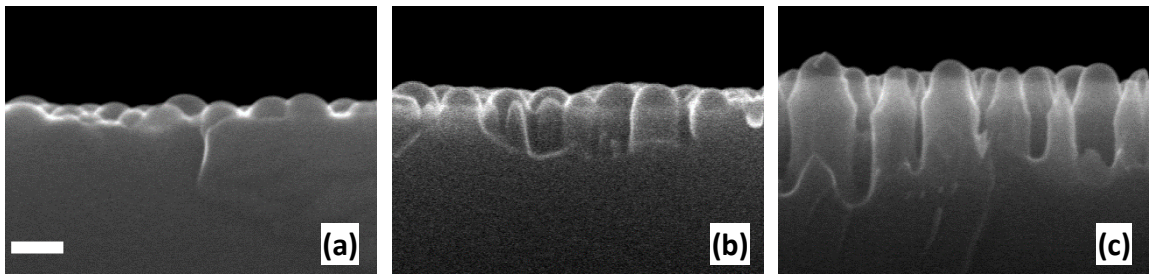


*Figure 13: SEM images of (a) as-evaporated, (b) 10'etched and (c) 15' etched samples for $CHF_3$ and $O_2$ flows of 25 sccm and 5 sccm respectively. Scale bar corresponds to 100 nm.*

The directional etching process is analyzed through cross-sectional SEM images taken in samples etched during 10 and 15 minutes (Figure 13). For a 15-min etching, the SiNCs average height is 200 nm with a variable diameter between 40 nm and 100 nm. As a consequence of the Ga NP size reduction, the nanocolumns are tapered shape (Figure 13.c). In order to study the effect of the gas flow on the nanocolumn morphology, an

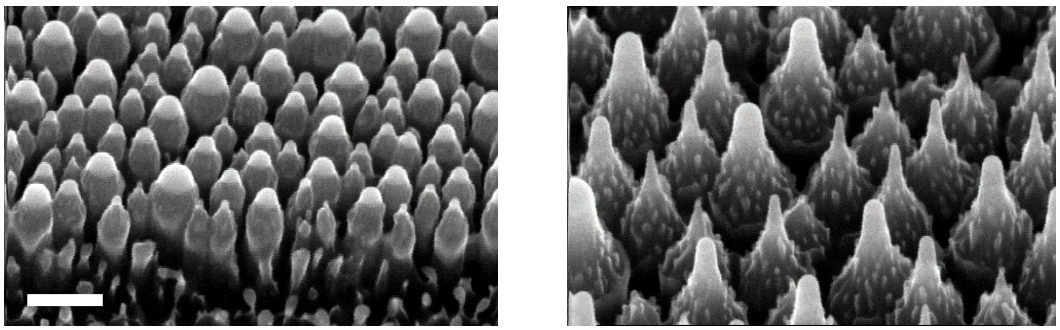

*Figure 14: Nanocolumns structure after 15' etching process for the $CHF_3$ flow cases: (a) 25 sccm and (b) 100 sccm. Oxygen flow was maintained steady at 5 sccm. Scale bar corresponds to 200 nm.*

aerial viewgraph of the 15 min etched sample was compared to a sample treated under a plasma formed from a 100 sccm flow of $CHF_3$ for the same time (Figure 14). The gas flow increase leads to obtain significantly tapered structures with a nanotip end covered by the remaining GaNP. Also, nanostructures density decrease since nanocolumns made by smaller NP disappear faster than the other.

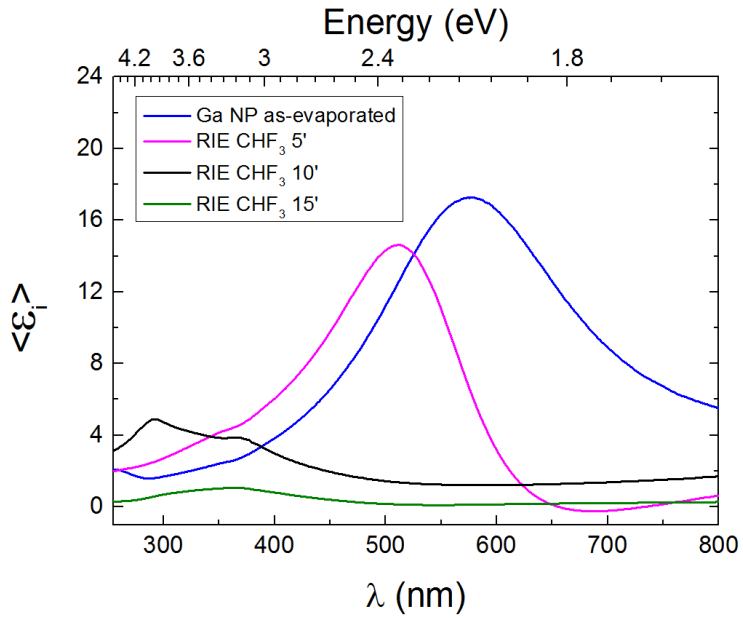


*Figure 15: (a) SE measurements of the pseudo-dielectric imaginary part of the as-evaporated and etched samples. Clearly plasmon resonance absorption decrease as time as the etching process goes by.*

Further optical measurements of the developed structures were carried out. From the ellipsometry spectroscopy (SE) (Figure 15), it was observed a decrease of the plasmonic peak absorption related to the Ga NPs presence (λ=575 nm). The longer the etching time, the lower the equivalent absorption. It is believed that the NPs average dimension reduce its value while the etching process occurs, leading to a blue shift of the absorption peak. About the decrease of the amplitude signal, it was thought at the first instance that the appearance of the SINCs strongly modify the Ga NPs surface distribution, hence the absorbed incoming light. However, looking at the sample with naked eyes, the surface changes from to be reflective (Figure 16.a before etching) to a deep black color (Figure 16.a after etching). According to the Rayleigh and Mie scattering theories [22], the incoming light will be higher scattered between the nanostructured Si, depending of the structure size comparison with the relative light wavelength. This phenomena will assure

higher chances for the light to be absorbed and that is the reason of the sample black appearance. Regarding the SE analysis decrease, it was found that samples with formed nanocolumns did not give back enough signal to the equipment detector, which was wrongly interpreted as low absorption result. Also, the 15 mins etched sample shows a

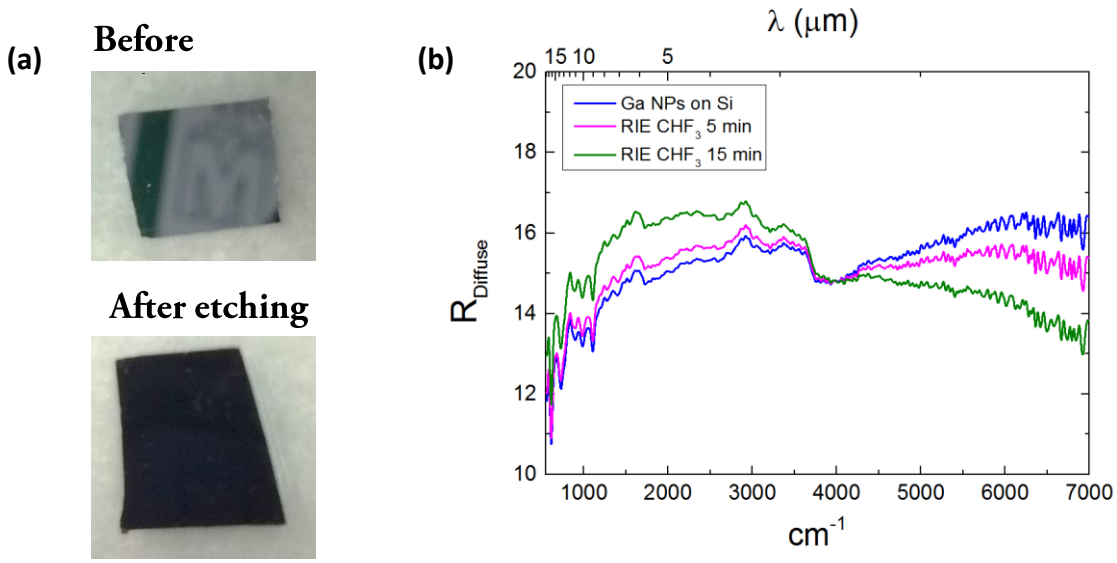


*Figure 16: (a) Looking at the samples with naked eyes shows peculiar dark colour after SiNCs formation. (b) FTIR diffuse reflectance measurements.*

gradually enhancement of the absorption figure as much as the input light moves toward IR wavelengths. It well agree with previous structure scattering statement and with the further diffuse reflectance analysis shown in figure 16.b.

The diffuse reflectance spectra of the as-evaporated, 5' and 15' etched samples was investigated with the use of Fourier transform infrared (FTIR) technique (Figure 16.b). Diffuse reflectance for the three samples shows a different behavior in the spectral range under study. At small wavenumbers (500-3500 $cm^{-1}$), the diffuse reflectance increases with the etching time due to the higher surface scattering but with less impinging light bouncing into the structure. However, at high wavenumbers (4000-7000 $cm^{-1}$), the diffuse reflection diminishes revealing light trapping effect and grading of the surface layer

effective permittivity.[23, 24] These effects have their origin in the multiple scattering process taking place in the region between the nanostructures as the wavelength becomes shorter. As the SiNCs getting higher, the impinging light can be scattered between the structures with higher chances to be transmitted into the material. Finally, the unusual

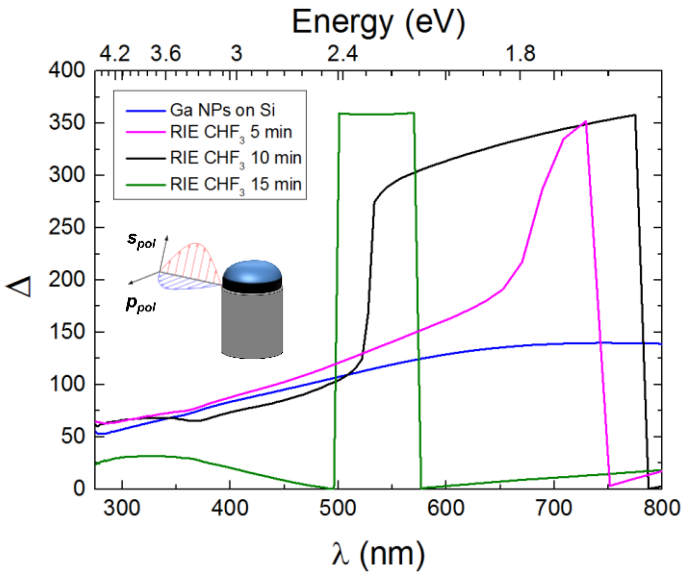


*Figure 17: the graph shows the SE phase shift measurements of the as-evaporated and different etched samples. After nanocolumns formation, the delta value slightly changes across the spectra not considering the step wavelengths interval.*

abrupt slope of the curve at 3800 $cm^{-1}$ (2630 nm) was due to the measurement normalization with the FTIR lamb base line, with no physical reason nor valuable delivered information.

Finally, the samples sensitivity to the light polarization vector was also investigated. Because of the SE elliptical light polarization, a phase shift between the s and p polarization vector at the light/surface interface would be possible depending on the material. Then, incident light phase shift parameter was measured at 70° for treated and untreated samples. A remarkable change of the Δ was obtained during the nanocolumns formation (Figure 17) especially for the 15' process. It seems that formed nanocolumns caused a similar phase shift in both polarization components resulting in a low Δ value close to zero (green curve). The measured ψ parameter - which is proportionally to the

amplitude of the component reflected signal (see chapter 2) – varies between a value of 30 and 35 between 2 and 1.5 eV range. It means that mostly both the s and p components will interact with the structures, making this structure suitable for maximizing the absorption incoming signal for unpolarized light source such as solar cells applications.

# 5.2 Wet etching: Ga NPs coverage and their endurance in harsh environment

In order to control the NPs coverage rate on a surface and their size distribution, wet etching will be also possible. This method consists in using a chemical acidic or basic solution to selectively etch a surface structure. Compared to dry etching methods, the use of a solution allows large area process with easy reproducibility, where usually no equipment are needed. Common metal and oxide etchants in wet etching process can be HF, HCl or $H_3PO_4$ [25], which have been largely used in microelectronics and material modification. Normally the acid is put in solution with deionized water (DIW) in a specific concentration from which the etching time will depend. Nevertheless, different etching methods such as drop casted, acidic bath or vapor can be chosen depending on the purpose.

To investigate the thermally evaporated Ga NPs endurance in harsh environment, the following acid solutions were used:

- ***$H_3PO_4$ : DIW [1:100]***

  Phosphoric diluted solution was used to test the effect of weak acid (low dissociation constant $K_A$) on the NP-covered Si surface for a 30' and 60' time. It is a non-toxic acid largely used in food additive, cleaning products and water treatment.

- ***HCl : DIW [1:100]***

Chloridric diluted solution was used to test the effect of a strong acid (high dissociation constant $K_A$) on the NP-covered Si surface for a 30' and 60' time. It is largely used in microelectronic process to clean the surface from metallic leftover and for the industrial production of plastic and food additive.

Both are well-known oxide etchants and they have been widely used to etch native shell around metal NPs.

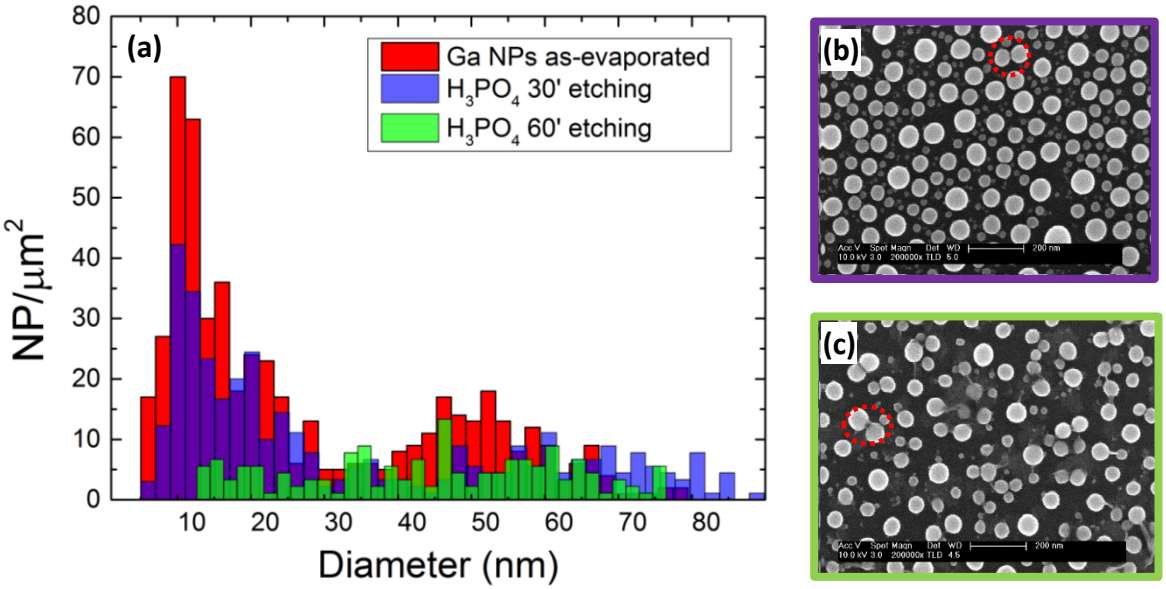


*Figure 17: (a) NPs size histograms for as-evaporated, 30' and 60' $H_3PO_4$ etched samples. The surface coverage can be reduced from 80% to 31% and small NP density can be strongly reduced, turning the distribution from bimodal to quasi-monomodal. The SEM Images are taken from the (b) 30' and (c) 60' etched samples.*

First, we studied the effect of $H_3PO_4$ etching on the NP surface coverage. The structures diameter distribution was calculated from the related SEM image as shown in figure 17.a. Before the etching, Ga NPs showed a bimodal distribution with two size ranges exhibiting diameters between 5 and 25 nm (1st range), and between 30 and 80 nm (2nd range). During the first steps, the acidic treatment removes the oxide layer around the nanoparticles exposing the bare Ga surface to the chemical environment of the solution. On the other hand, the ions in the solution contribute to reoxidize the surface of the bare nanoparticles in a competitive process that produces the effective reduction of the NP size. Eventually, the uncovered metal can gain surface mobility leading to the interaction

and coalescence of some of the NPs according to the Oswald ripening theory. [26] After 30' etching process, parts of the smaller NP disappeared, while bigger ones increased their dimension likely because of NP coalescence during the etching. After 60' etching, it was obtained a quasi-monomodal distribution where most of the small NP disappeared. The related SEM images gave clear evidence that Oswald ripening occurred between the NP, where some NP couples are found due to their displacement and interaction (red dashed circles in Figure 17.c). The surface coverage rate was tuned from 80% (as-evaporated) to 31%, depending on the etching time. Interestingly, the $H_3PO_4$ weak acid nature likely allowed a slow etching process of the structure, promoting the coalescence phenomena between the NPs.

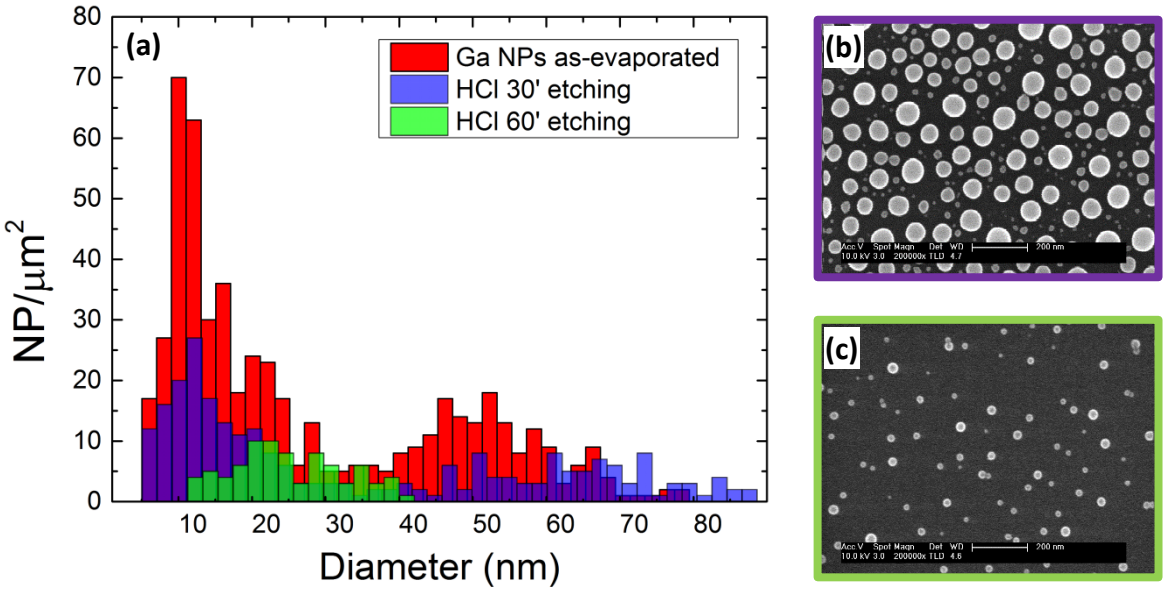


*Figure 18: (a) NPs size histograms for as-evaporated, 30' and 60' HCl etched samples. The surface coverage can be reduced from 80% to 5% and bigger NP density can be strongly reduced, turning the distribution from bimodal to quasi-monomodal. The SEM Images are taken from the (b) 30' and (c) 60' etched samples.*

Finally, HCl acid solution was used to study faster wet etching process effect on the Ga NP. A similar conclusion can be drawn as in the $H_3PO_4$ but the native oxide etching occurs faster than in the previous case. After 60' process, the as-evaporated bimodal distribution can be turned to monomodal but with smaller NP and low surface coverage (5%) than in the $H_3PO_4$.

# Conclusions

To conclude, Ga hemisphere and nanocones have demonstrated to increase the local electric field around the structure depending of their geometry. According to the simulations results, the conical NPs obtained from the plasma treatment enhances the electromagnetic field two fold near the base of the structure compared to the as-evaporated hemispherical one.

Jointly with the oxygen plasma treatment, the wet etching based on HCl and $H_3PO_4$ can be successfully used to control the Ga NPs surface coverage and their size to tailor the characteristics of the NP coating.

Finally, SiNCs were fabricated with the use of Ga NPs as a hard mask. The reflected light by the surface has been lowered in a range between 1450 nm to 2500 nm as shown by the FTIR measurements. Additionally, the absorption of visible light seems to be improved through light trapping effects. Then, the developed structures will find large use for the sensor surface modification to achieve lower incident light reflection [27,28], higher LED extraction efficiency [29] and tuning of the bio-sensor surface functionalization layer.

# References


[1] James F. Ziegler, "SRIM-2003", Nuclear Instruments and Methods in Physics Research Section B: Beam Interactions with Materials and Atoms **219-220**, 1027 (2004).

[2] Y. Yamamura et al, "Angular Dependence of Sputtering Yields of Monatomic Solids", Institute of Plasma Physics **Report No. IPPJ-AM-26** (1983).

[3] A. U. Alam, M. M. R. Howlader, and M. J. Deen, "The effects of oxygen plasma and humidity on surface roughness, water contact angle and hardness of silicon, silicon dioxide and glass", Journal of Micromechanics and Microengineering **24** (3), 035010 (2014).

[4] K. Kikuchi, S. Imura, K. Miyakawa, H. Ohtake, and M. Kubota, "Properties of Ga 2 O 3 /Ga 2 O 3 :Sn/CIGS for visible light sensors", Journal of Physics: Conference Series **619** (1), 012009 (2015).

[5] F. G. Allen and G. W. Gobeli, "Work Function, Photoelectric Threshold, and Surface States of Atomically Clean Silicon", Physical Review **127** (1), 150 (1962).

[6] T. García-Mendiola A. García Marín, C. N. Bernabeu, M. J. Hernández, J. Piqueras, J. L. Pau, F. Pariente, E. Lorenzo, "Gallium plasmonic nanoparticles for label-free DNA and single nucleotide polymorphism sensing", Nanoscale **8**, 9842 (2016).

[7] Chenxiang Lin, Yan Liu, and Hao Yan, "Self-Assembled Combinatorial Encoding Nanoarrays for Multiplexed Biosensing", Nano Letters **7** (2), 507 (2007).

[8] International Centre for Diffraction Data.

[9] Maksym Yarema, Michael Wörle, Marta D. Rossell, Rolf Erni, Riccarda Caputo, Loredana Protesescu, Kostiantyn V. Kravchyk, Dmitry N. Dirin, Karla Lienau, Fabian von Rohr, Andreas Schilling, Maarten Nachtegaal, and Maksym V. Kovalenko, "Monodisperse Colloidal Gallium Nanoparticles: Synthesis, Low Temperature Crystallization, Surface Plasmon Resonance and Li-Ion Storage", Journal of the American Chemical Society **136** (35), 12422 (2014).

[10] S. Catalán-Gómez, A. Redondo-Cubero, F. J. Palomares, F. Nucciarelli, and J. L. Pau, "Tunable plasmonic resonance of gallium nanoparticles by thermal oxidation at low temperatures", Nanotechnology **28** (40), 405705 (2017).

[11] Fritz Aldinger, "Controlled porosity by an extreme kirkendall effect", Acta Metallurgica **22** (7), 923 (1974).

[12] Hong Jin Fan, Ulrich Gösele, and Margit Zacharias, "Formation of Nanotubes and Hollow Nanoparticles Based on Kirkendall and Diffusion Processes: A Review", Small **3** (10), 1660 (2007).

[13] A. M. Gusak and T. V. Zaporozhets, "Hollow nanoshell formation and collapse in binary solid solutions with large range of solubility", Journal of Physics: Condensed Matter **21** (41), 415303 (2009).

[14] Abdel-Aziz El Mel, Ryusuke Nakamura, and Carla Bittencourt, "The Kirkendall effect and nanoscience: hollow nanospheres and nanotubes", Beilstein Journal of Nanotechnology **6**, 1348 (2015).

[15] Bruce T. Draine and Piotr J. Flatau, "Discrete-Dipole Approximation For Scattering Calculations", J. Opt. Soc. Am. A **11** (4), 1491 (1994).

[16] Svetoslav Koynov, Martin S. Brandt, and Martin Stutzmann, "Black nonreflecting silicon surfaces for solar cells", Applied Physics Letters **88** (20), 203107 (2006).

[17] Lin Yao and Junhui He, "Recent progress in antireflection and self-cleaning technology – From surface engineering to functional surfaces", Progress in Materials Science **61**, 94 (2014).

[18] Xin-Tong Zhang, Osamu Sato, Minori Taguchi, Yasuaki Einaga, Taketoshi Murakami, and Akira Fujishima, "Self-Cleaning Particle Coating with Antireflection Properties", Chemistry of Materials **17** (3), 696 (2005).

[19] C. Gatzert, A. W. Blakers, Prakash N. K. Deenapanray, D. Macdonald, and F. D. Auret, "Investigation of reactive ion etching of dielectrics and Si in CHF3⁄O2 or CHF3⁄Ar for photovoltaic applications", Journal of Vacuum Science & Technology A **24** (5), 1857 (2006).

[20] H. Jansen, M. de Boer, R. Legtenberg, and M. Elwenspoek, "The black silicon method: a universal method for determining the parameter setting of a fluorine-based reactive ion etcher in deep silicon trench etching with profile control", Journal of Micromechanics and Microengineering **5** (2), 115 (1995).

[21] Heon Lee, David B. Oberman, and James S. Harris, "Reactive ion etching of GaN using CHF3/Ar and C2ClF5/Ar plasmas", Applied Physics Letters **67** (12), 1754 (1995).

[22] Xiaofeng Fan, Weitao Zheng, and David J. Singh, "Light scattering and surface plasmons on small spherical particles", Light: Science &Amp; Applications **3**, e179 (2014).

[23] Rolf Brendel, *Thin-Film Crystalline Silicon Solar Cells: Physics and Technology*. (John Wiley & Sons, 2011).

[24] Mehdi Keshavarz Hedayati and Mady Elbahri, "Antireflective Coatings: Conventional Stacking Layers and Ultrathin Plasmonic Metasurfaces, A Mini-Review", Materials **9** (6), 497 (2016).

[25] W. H. Tarn P. Walker, "Handbook of Metal Etchants", (1990).

[26] J. A. Marqusee and John Ross, "Theory of Ostwald ripening: Competitive growth and its dependence on volume fraction", The Journal of Chemical Physics **80** (1), 536 (1984).

[27] K. V. Baryshnikova, M. I. Petrov, V. E. Babicheva, and P. A. Belov, "Plasmonic and silicon spherical nanoparticle antireflective coatings", Scientific Reports **6**, 22136 (2016).

[28] Jonathan Moghal, Sasha Reid, Lisa Hagerty, Martin Gardener, and Gareth Wakefield, "Development of single layer nanoparticle anti-reflection coating for polymer substrates", Thin Solid Films **534**, 541 (2013).

[29] Gabriel Lozano, Said R. K. Rodriguez, Marc A. Verschuuren, and Jaime Gómez Rivas, "Metallic nanostructures for efficient LED lighting", Light: Science &Amp; Applications **5**, e16080 (2016).

# Chapter 6

# Antireflective coatings based on Ga NPs for avalanche photodiodes

The detection of an impinging light signal by a sensor will depend on the specific wavelength and the device active semiconductor material. In the case of a photodiode structure, the incident photon has to provide enough energy to excite electrons from the valence to the conduction band in order to generate significant photocurrent. For infrared (IR) application, Gallium Arsenide (GaAs) alloys have been largely used to produce highest efficiency solar cells and infrared sensor for security and space applications. [1, 2, 3] The reason of their success lays on the excellent epitaxial growth quality and its bandgap energy of 1.4 eV, which allows to produce device with low signal to noise ratio. However, one of the main GaAs compounds issue is related to the high surface reflectivity of this material due to the abrupt change of refractive index between air (n=1) and the semiconductor (n≈ 3.4) at the working wavelength. The use of an antireflective coating (ARC) can easily overcome this problem allowing a higher light current conversion due to the raise the number of transmitted photons into the device. One of the most promising and innovative ARC layer strategy has been based on the use of nanostructured layer made by NPs.[4,5,6] This solution allows high tunability of the developed ARC physical parameter and easy fabrication compared to conventional technological solution.

For this reason, the development of innovative antireflective coatings (ARCs) for these light sensor devices has been deeply investigated to minimize the reflectivity. This chapter will show the development of tuned Ga NPs-based ARCs for InGaAs/InAlAs APD structures.

# 6.1 Ga NP antireflective coating (ARC) effect

Herein the results of Ga NPs as ARC on different substrates are presented. Before to test and investigate them on fabricated APD devices, the Ga NPs optical properties were previously studied on InAs and quartz bare surface. The NPs were deposited by direct thermal evaporation on the samples, an easy and low cost process expendable for a plenty of devices. The measurements gave the possibility to tune the NP dimension and their surface coverage to achieve the lower reflection value. Finally, it was attested their effectiveness on the device performance enhancement in four different cases: room temperature deposition, adding a buffer layer between NPs and after thermal treatments of both previous cases.

## 6.1.1 Reflectivity properties of Ga NPs coating layer

When NPs cover a material surface, the improvement of ARC property can be attributed to a reduction of the surface reflectivity. Physical parameters of the Ga NPs layer can be obtained using the Maxwell-Garnett effective medium approximation as previously explained on Chapter 2. The advantages of using Ga NPs compared to other materials is strictly related to the possibility to vary the metal/oxide ratio through low temperatures treatments with easy and cost effective process. Thus, the effective permittivity of the equivalent layer can be tailored in a broad range that allows optimization of device responsivity.

According to the basic ARC theory [7], the best refractive index value for a coating layer is $n_{ARC} = \sqrt{n_{air} n_{sub}}$, which in the case InAs surface devices is aspect to be close to 1.9, while in the case of quartz approach 1.22 . Table 1 includes the calculated values of the effective refractive index of the extreme cases, either liquid gallium or gallium oxide

according to the Maxwell-Garnett theory for different coverage percentuages. The constant values of the metal and oxide Ga were taken from Knight et al [8] and Rebiena et al [9] works.

TABLE 1: Calculation of the effective refractive index for liquid and oxide Ga NPs layer with hemisphere shape, 23 nm average diameter and surface coverage volume fraction values of 20%,40% and 60%.

| Material | 20% | 40% | 60% |
|---|---|---|---|
| *Liquid gallium* | $n_{eff} = 1.33$ | $n_{eff} = 1.74$ | $n_{eff} = 2.37$ |
| *Gallium oxide* | $n_{eff} = 1.11$ | $n_{eff} = 1.24$ | $n_{eff} = 1.36$ |

It can be deduced that only a surface coverage value between 40% and 60% of liquid gallium NP may allow to reach the desired $n_{ARC}$ value of 1.9. However, varying the Ga NP oxide shell thickness can also induce a change of the structure overall refractive index depending on the metal/oxide ratio. [10] Figure 1 shows the schematically situation of a spherical Ga NP and the equations to calculate the effective permittivity of the parametrized oxide shell. Both ways of tuning refractive index of Ga NPs are powerful methods to match the best ARC condition on a given substrate. Previous works of our group demonstrated that the thickness of the oxide shell can be enlarged through thermal

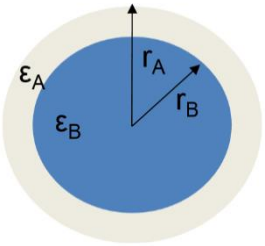


$$\varepsilon_{eff} = \varepsilon_B \frac{\varepsilon_A + 2\varepsilon_B + 2f(\varepsilon_A - \varepsilon_B)}{\varepsilon_A + 2\varepsilon_B - f(\varepsilon_A - \varepsilon_B)} \quad (1)$$

$$f = \frac{r_A}{r_B}$$

Figure 1: Sketch and formula to calculate the relative effective permittivity of a sphere core-shell structure like the used Ga NP.

treatment in low temperature range (< 300 $^{o}$C). [11] We have followed this method to modify the refractive properties of InAs and quartz substrate.

# a) Ga NPs on InAs

In order to study the effect of a Ga NPs layer on InAs optical properties, the semiconductor surface was coated with Ga using a Joule-effect Edwards E306 evaporation system. Gallium 99.9999% was heated for 10''with a 50 W DC power source under $10^{-6}$ Torr pressure. By changing the evaporation time, different NPs size distribution were compared to study their effect on the optical surface properties. The distance between the crucible heater and the samples was set at 20 cm and the gallium nucleation process was steady with the use ice cooling system. In fact, the lower the temperature of the nucleation interface, the less the nanoparticles coarse with one another.

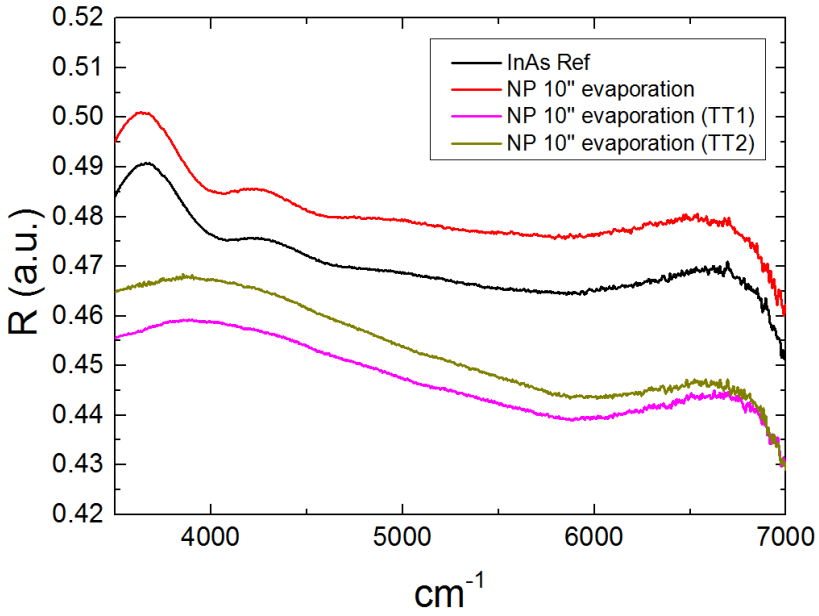


Figure 2: Reflection measurement of treated Ga NPs layer on InAs surface. After thermal treatments, lower light reflection was achieved along the examined spectral range.

The Ga NPs covered surface was further characterized by specular reflectance measurement using a Fourier transform infrared spectroscopy (FTIR) technique. The measurement includes a broad infrared range, from 7.000 cm-1 (1.428 nm) to 500 cm-1 (20.000 nm). Figure 2 compares the normal reflectance results as function of the interested incident light wavenumber range for bare InAs reference, 10'' evaporated NP and thermally modified NPs samples. The deposited structures have an average diameter of 23 nm, which makes negligible the surface IR light scattering contribution due to their small dimension. [10] However, the reflection signal along the spectrum was found higher than the bare InAs substrate, likely because of the liquid gallium absorption in the IR range. [12] Additionally, the NP composition was modified with the use of different thermal treatments that made possible to vary the native oxide shell thickness. First treatment called TT1 was a 90 °C anneal during 120 minutes, while second treatment called TT2 involved a first 90 °C for 120 minutes step plus 140 °C anneal during 120 minutes. Both cases showed a decrease of the reflected light at the InAs surface in the whole considered infrared range. It strengths the hypothesis that a compositional change of the Ga NPs equivalent layer may better approach the $n_{ARC}$ condition.

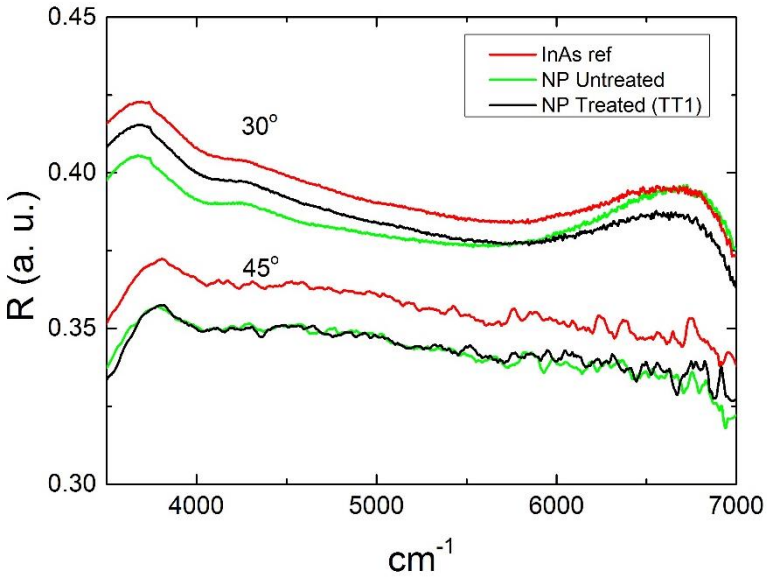


Figure 3: Reflection measurements of treated and untreated Ga NP layer at 30° and 45°. For both cases, it was obtained an enhancement of the InAs surface acceptance angle of an impinging light.

To further investigate the effect of Ga NPs coverage on the reflectance, tilted FTIR analysis was also performed at different incidence angles of 30º and 45º (Figure 3). In this case, the study was carried out on the untreated and TT1 Samples. For both sample, it was observed a decrease of the reflectivity, with an enhancement of the surface acceptance angle of the incident light. Interestingly, the untreated sample (green line) shows a different behaviour at normal and tilted incidence. The origin of this could lay on the increase of the forward scattering phenomena at tilted angles caused by the NP layer.

# b) Ga NPs on quartz

This study will investigate the effect of Ga NPs on quartz surface measuring optical transmission in the IR spectra. For the considered range of wavelengths, quartz shows itself mostly transparent to the source incident light, which allows to measure light transmission. The analysed samples were made by NPs evaporations time of 10, 20 and 60 seconds with an equivalent average diameter of 23 nm, 100 nm and 300 nm respectively. For the sake of comparison, the sample with NPs of 23 nm in diameter was also analysed after TT1 process.

According to the effective medium theory, the presence of the NP will modify the refractive index at surface along the light path through the sample. Unexpectedly, it was observed that the untreated NPs samples do not show any transmission feature enhancement. It has been thought that multi-scattering phenomena of the out-coming light could be a possible reason. For this reason, the samples were also measured with a fixed tilt angles of 15º, 30º and 45º to detect changes on the light transmission (Figure 4). As in the previous analysis on InAs, the TT1 treated sample (orange line) measurements led to an enhancement of the transmittance at all the tilted cases in the spectra region between 2,350 $cm^{-1}$ (4.2µm) and 2,700 $cm^{-1}$ (3.7 µm).

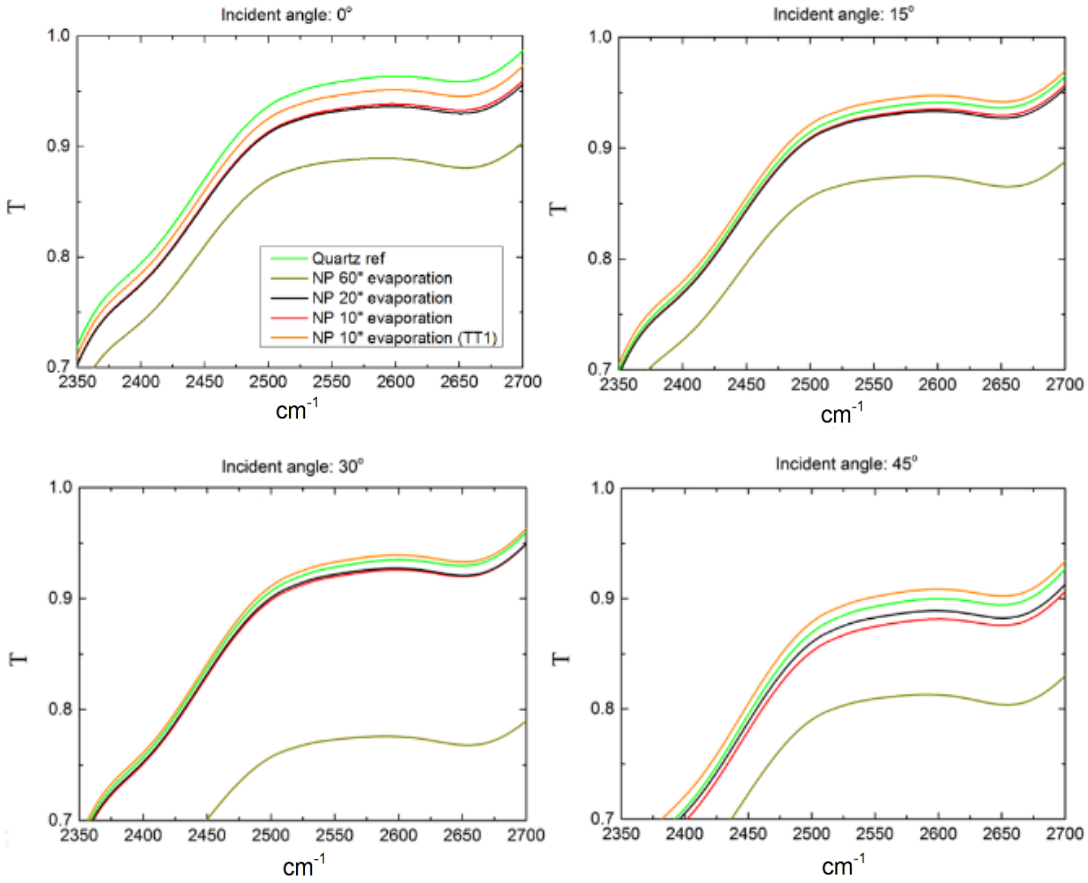


Figure4: Transmission measurement of G NPs layer on quartz at 0°,15°,30° and 45°.

## 6.1.2 $In_{(0.53)}Ga_{(0.47)}As/In_{(0.52)}Al_{(0.48)}As$ APD samples

Generally, performance of an APD device can be evaluated in terms of the exhibited dark current ($I_D$), responsivity (R) and excess avalanche noise factor (F). The $I_D$ represents the current signal when the device is not under illumination due to leakage phenomena, which depends on the material intrinsic defects. The relationship between impinging photons and the generated current is determined by the R and it is strictly related to the device material and structure. Since the device current generation is based on electron avalanche mechanism, a low F is important to keep a high signal to noise ratio. In the case of a device with high R and low $I_D$ and F, it would be easier to detect low illumination level.

Optical communications applications in the IR range requires the use of $In_xGa_{1-x}As$ alloy as the absorption layer in avalanche photodiodes. The x represents the material in continent, which is adjusted to match the lattice parameters of the substrate in order to avoid defects or interlayer surface stress generation. Considering an InP substrate, typical commercial x value is 0.53. In addition, InAlAs alloy is often used as the material of the multiplication layer because of its wide bandgap energy, which leads to obtain a low F.[13] The devices have shown good performance in optical communication such as single photons counters application.[14,15] One of the best device performances has been achieved by Nada et al.[16], who reported a $f_{3dB}$= 18.5 GHz with M=10 and a R-bandwidth product of 168 A/W·GHz with a vertically illuminated device of InAlAs region.

| Thickness | Material | Doping type | Doping level |
|---|---|---|---|
| 100.0 nm | $In_{(0.53)}Ga_{(0.47)}As$ | P | 1.0E19 $cm^{-3}$ |
| 100.0 nm | $In_{(0.52)}Al_{(0.48)}As$ | P | 2.0E18 $cm^{-3}$ |
| 100.0 nm | $In_{(0.52)}Al_{(0.48)}As$ | Undoped | 1.0E14 $cm^{-3}$ |
| 25.0 nm | $Al_{(0.15)}Ga_{(0.32)}In_{(0.53)}As$ | Undoped | 1.0E14 $cm^{-3}$ |
| 25.0 nm | $Al_{(0.29)}Ga_{(0.18)}In_{(0.53)}As$ | Undoped | 1.0E14 $cm^{-3}$ |
| 1700.0 nm | $In_{(0.53)}Ga_{(0.47)}As$ | Undoped | 1.0E14 $cm^{-3}$ |
| 25.0 nm | $Al_{(0.15)}Ga_{(0.32)}In_{(0.53)}As$ | Undoped | 1.0E14 $cm^{-3}$ |
| 25.0 nm | $Al_{(0.29)}Ga_{(0.18)}In_{(0.53)}As$ | Undoped | 1.0E14 $cm^{-3}$ |
| 69.0 nm | $In_{(0.52)}Al_{(0.48)}As$ | P | 4.2E17 $cm^{-3}$ |
| 1000.0 nm | $In_{(0.52)}Al_{(0.48)}As$ | Undoped | 1.0E14 $cm^{-3}$ |
| 100.0 nm | $In_{(0.52)}Al_{(0.48)}As$ | N | 2.0E18 $cm^{-3}$ |
| 1000.0 nm | $In_{(0.53)}Ga_{(0.47)}As$ | N | 5.0E18 $cm^{-3}$ |

Figure 5: InGaAs/InAlAs device mesas structure

Figure 5 shows the InGaAs/InAlAs device structure used for the investigation. The circular mesa device with top Au contact were fabricated at the University of Sheffield using molecular beam epitaxy (MBE) technique on a semi-insulating InP substrate and optical lithography (Figure 6). The wafer primary characteristic consist of a 1700 nm thick InGaAs absorption layer and a 1000 nm thick InAlAs multiplication layer. The layers were

designed to increase the photon absorption efficiency and to reduce the tunnelling current through InAlAs. A 69 nm p-type InAlAs charge sheet region was introduced to enhance the difference between the absorption and the avalanche electric fields. The transitional AlGaInAs layers were designed to gradually change the bandgap values at the ternary materials heterojunction.

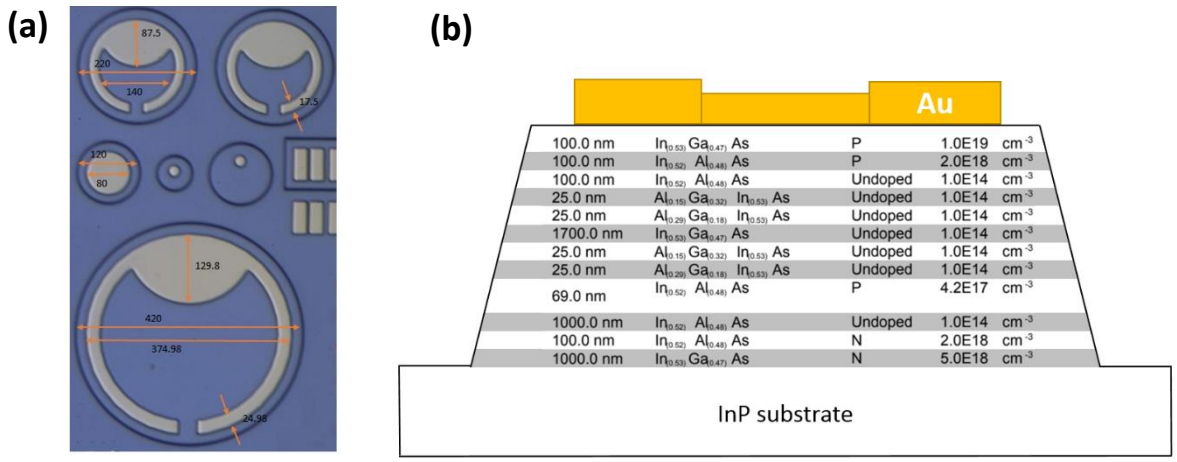


Figure 6: (a) Optical microscope images of the fabricated mesa diodes with dimensions measurement in micrometer. (b) Mesa side view sketch of the devices.

## 6.1.3 Ga NPs ARCs on APD samples

The evaporation process was carried out on a bare APD sensor and furtherly characterized by SEM as shown in Figures 7.b and 7.c.. The surface of the APD sample was covered with Ga NPs of 23 nm diameter in average and a surface coverage factor of 57%. As Figure 7.d shows, NPs size distribution was found to be slightly asymmetrical with diameters between a few nanometres and 40 nm. Investigations in other semiconductor substrates showed that the NPs have a hemispherical shape as other authors previously investigated[9] and they were also present on the device edge side with same shape and homogeneity.

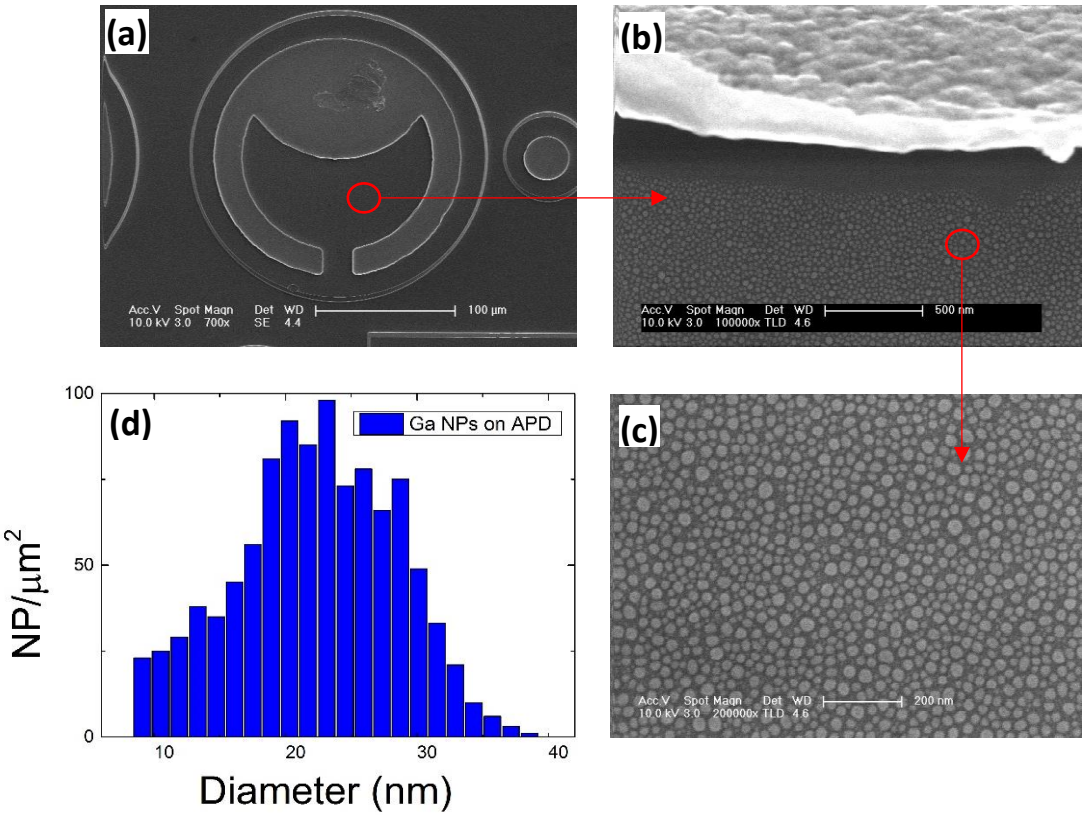


Figure 7: (a,b,c) Scanning electron microscopy images of Ga NPs evaporated on the light sensor surface. (d) NPs distribution with an average diameter of 23 nm.

On the bare sensor the deposited NPs also covered the mesa sidewalls. This has a deleterious effect on the device properties, especially on the dark current level, which is strongly increased. To prevent that, a passivation PMMA layer is introduced by spin coating before Ga NPs deposition, in one of the samples as shown in figure 8.c.. The study

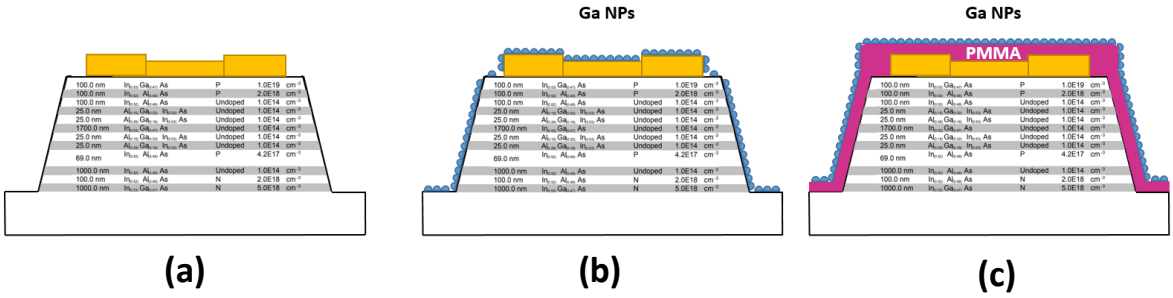


Figure 8: Sketch of the studied structure: (a) bare APD, (b) Ga NPs on APD surface and (c) Ga NPs on passivating PMMA layer.

was carried out for three different type of samples: bare APD (Figure 8.a), Ga NPs evaporated on device surface (Figure 8.b) and Ga NPs evaporated on a previous spin coated PMMA passivation layer (Figure 8.c).

## 6.1.4 Electro-optical characterization of APDs

A customized setup for the optical characterization of the InGaAs/InAlAs APD was built. The sensor photocurrent measurement required the use of a laser diode device with a 1550 nm wavelength. The laser, acquired from Covega/Thorlabs, was temperature stabilized under DC operation by a temperature controller (TEC) and it was assembled onto a Faraday cage. This allowed to directly insert the fibre on a Karl Suss four-probe station inside the cage to prevent environmental light noise. The laser beam was collimated at the fibre output and the power was adjusted by changing laser currents and inserting fibre optical attenuators. The measurements were carried out with and without illuminating the sensor, applying a reverse voltage of 75 V with steps of 0.3 V. Finally, micro-FTIR measurements were used to verify the effectiveness of the NP in lowering reflection.

## a) As-fabricated APD device

In order to compare the results between the modified and unmodified structures, the dark and photo currents of 60 µm, 110 µm, 210 µm radius devices were measured in the as-fabricated devices as references. The device dark current is generated due to surface defects issues that leads to undesired recombination phenomena. To determine the relationship between the leakage and the devices geometry, the current density was plotted against the perimeter/area (P/A) ratio for each device. For the sake of comparison, three different device for each size were analysed. Figure 9.a shows that the current density is fairly independent on the P/A ratio, showing a value close to $3\times10^{-5}\ {}^{A}/_{cm^2}$ . It

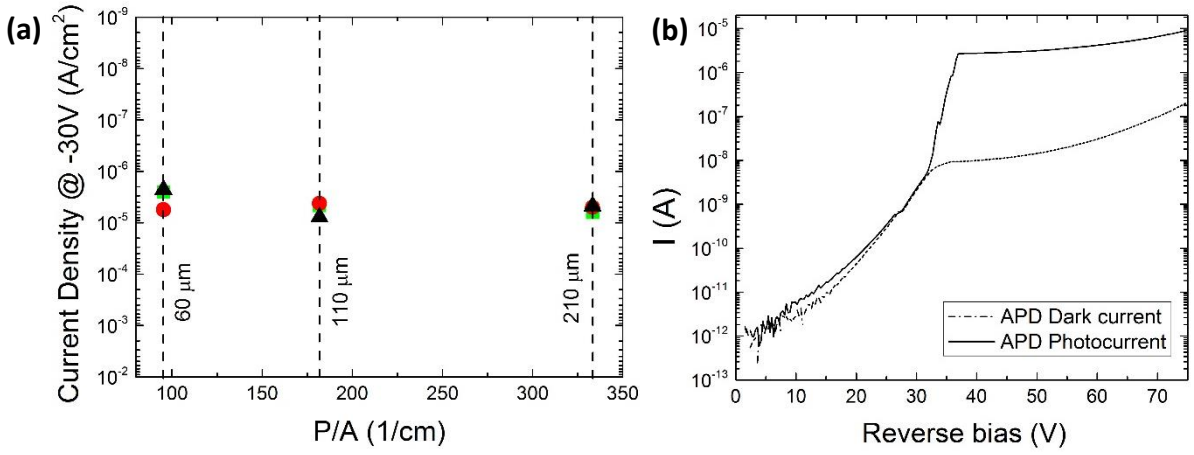


Figure 9: (a) Current density measurements for three different device sizes at 30 V reverse bias voltage. (b) Dark and photo current characteristic of 110 µm unmodified device as a function of reverse voltage.

means that the device dark current mainly scales as the device area, and less affected by mesa edge leakage. In light of the last consideration, further experiments were carried out mainly on the 110 µm radius one because of higher number availability. Figure 9.b shows the dark and light current of a typical device. The breakdown voltage was found to be 86 V, while the avalanche effect punch-through voltage is set at 37 V.

# b) Ga NP/APD device

A first device modification involved the use of Ga NPs on the surface. First, the dark I-V characteristic was measured in the modified device. The NPs evaporated on the surface enhanced the leakage current drastically enhanced compared to the unmodified APD red lined in figure 10. The increase is caused by new conduction mechanisms at the surface due to the nanoparticles vicinity near the junction at the mesa sidewalls. A large charge concentration at the surface is expected from the liquid gallium inside the NPs that might easily induce those mechanisms.

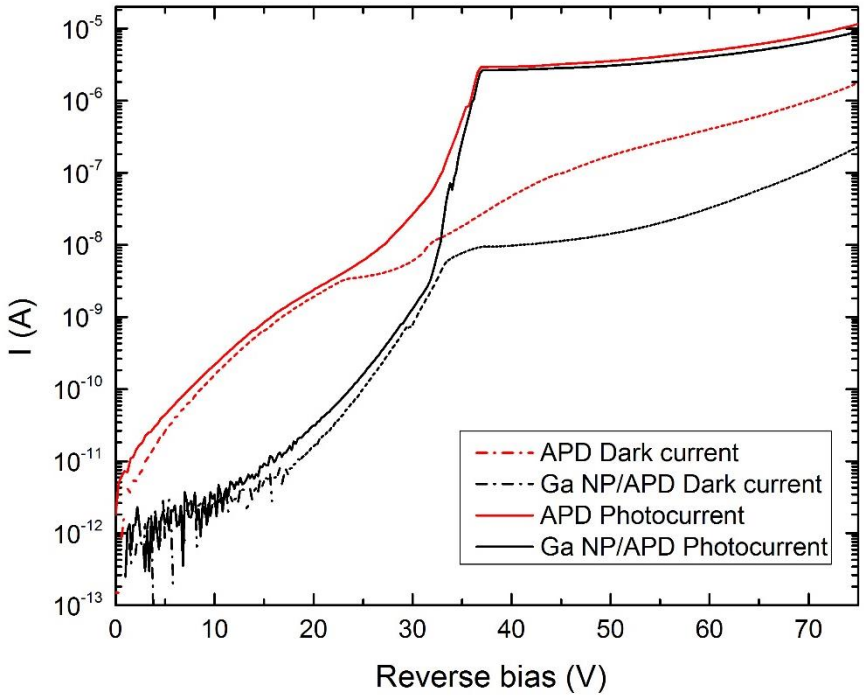


Figure 10: Both dark and light I-V characteristics comparison of before (black line) and after (red line) NP surface modification.

In fact, the GaAs based material tends to react with metals in air environment forming microconglomerates (e.g. anions) with different phase from the matrix. This means that the potential barrier height between some metal on the surface and the semiconductor will not simply be the difference between the work function and the electron affinity. The barrier will instead depend on the work function of the anion species and the so-called Fermi level pinning. In the case of Ga NP on InGaAs surface, we assume that the presence of the same metal material may balance such a creation of agglomerate on the surface. However, the contact will be ohmic because Ga has a work function of 4.36 eV while the electron affinity of GaAs is about 4.1 eV. The ohmic nature plus the possible presence of intermediate state in the gap can easily allow remarkably increase of the leakage current transport on the edge of the devices.

Regarding the measured photocurrent of the modified device, it exhibits an enhancement of about 10 % at 75 V reverse bias compared to the unmodified case (black

solid lines). The improvement was attributed to the change in the refractive index of the NPs layer, which reduced the surface reflectivity. Eventually, the device light acceptance angle could be improved by the presence of NP on the surface with an enhancement of the light generated signal. In fact, as previous tilted incoming light investigation attested, the presence of the NP may decrease reflectivity at the mesa sidewall because of the relative angle between the surface and the normal imping light.

# c) Ga NP/PMMA/APD device

As previous experiment demonstrated, the APD modification introduce surface leakage issues that raise the dark current contribution. Also, minority carriers lifetime can be reduced by surface state recombination, compromising the APD responsivity.[17] Introducing a buffer layer between the NP and the device may help to suppress carriers trapping and conduction at the surface. For this reason, further optimization of the devices involved the use of a previous spin coated PMMA layer between the NPs and the device. The used PMMA had an average thickness of 1000 nm, showing very low absorption (<0.1dB/mm) and a refractive index value of 1.57 at the device working wavelength of 1550 nm. As expected, Figure 11.a shows the dark current characteristic of

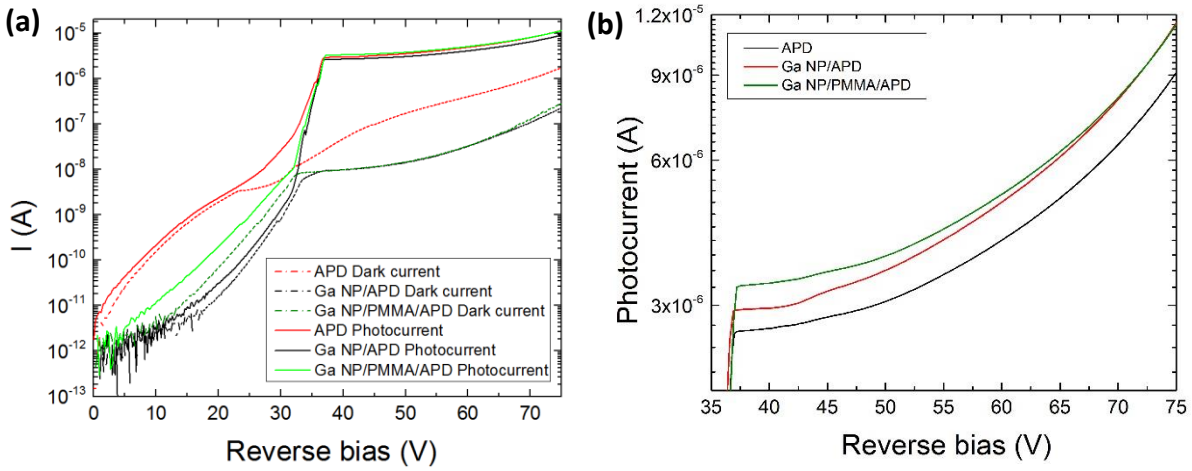


Figure 11: (a) I-V characteristics comparison of modified and unmodified structures. The use of a PMMA buffer layer between the InGaAs Surface and the NP lowered the dark current contribution, leading to similar photo-response enhancement result. (b) Photocurrent zoomed-in plot between 37V and 75V voltage range.

a Ga NP/PMMA/APD structure. The characteristic is very similar to the unmodified device above the punch through voltage (green and black line). Then, it was measured the device photocurrent that gave good results in terms of signal enhancement (Figure 11.b). Compared to the unmodified APD structure, an improvement of about 10% was achieved. In addition, a significant reduction of the dark current is achieved in comparison to the Ga NP/PMMA/APD structure.

### 6.1.5 Ga NPs thermal treated effect on the modified device response

Thus, to further optimize the optical constants of the NP layer to reduce reflectance, samples were exposed to several thermal treatments in a conventional lithography oven to thicken the Ga NP oxide outer shell. Taking into account that, the NP inner Ga and the native oxide shell materials differ in refractive index and absorption coefficient, tuning of the NP layer optical properties will be possible by changing their ratio. For the sake of comparison, TT1 and TT2 thermal processes were both used as described in the previous InAs samples characterization.

For the Ga NP/APD structure, after TT1 and TT2 the devices exhibit reduced dark currents due to increased oxide shell thickness to a value between 2 and 8 nm, as suggested by simulations and experimental data.[11] The more oxide the NPs, the lower the leakage current. This indicates that the oxidation process likely enhances the dielectric behaviour of the NPs, thus alleviating the leakage issue introduced right after their evaporation. However, in the operational range above punch-through the dark current signal is still higher than the reference device with no NPs.

On the other hand, the thermal treated Ga NP/PMMA/APD does not show significant changes after the thermal treatments above the punch-through voltage. From a practical point of view, the use of PMMA enables the trimming of the Ga NP properties

using low temperature annealing while stabilizing the dark current in the operational range.

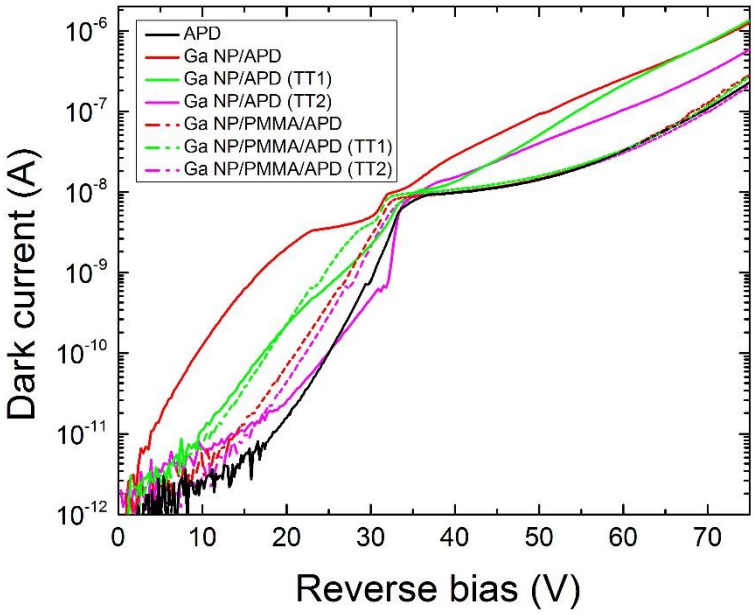


Figure 12: Dark current characteristics comparison of thermally modified structures

After thermal treatments, the photo response of both G NP/APD and Ga NP/PMMA/APD structures was also affected. As shown in Figure 13.a, in the case of ga NP/APD device, both TT1 and TT2 lead to photocurrent improvements compared to the unmodified device or untreated NP. It is believed that during the process, the effective refractive index of the NP layer changes and TT1 likely approaches the $n_{ARC}$ best value of 1.9 better than TT2. For the Ga NP/PMMA/APD case similar results are achieved even though other structural changes can play a role like the PMMA layer thinning caused by the thermal process. In fact, for Ga NP/PMMA/APD after TT1 (green line) resulted a better successful ARC design compared to the TT2 (violet line). The highest photocurrent improvement was also achieved after TT1, with almost 30 % of enhancement. Thus, TT1 sample with PMMA had similar result in terms of light signal shows the best ARC solution

displaying a dark current characteristic close to the one obtained for unmodified device, and a 30% improvement of the device response.

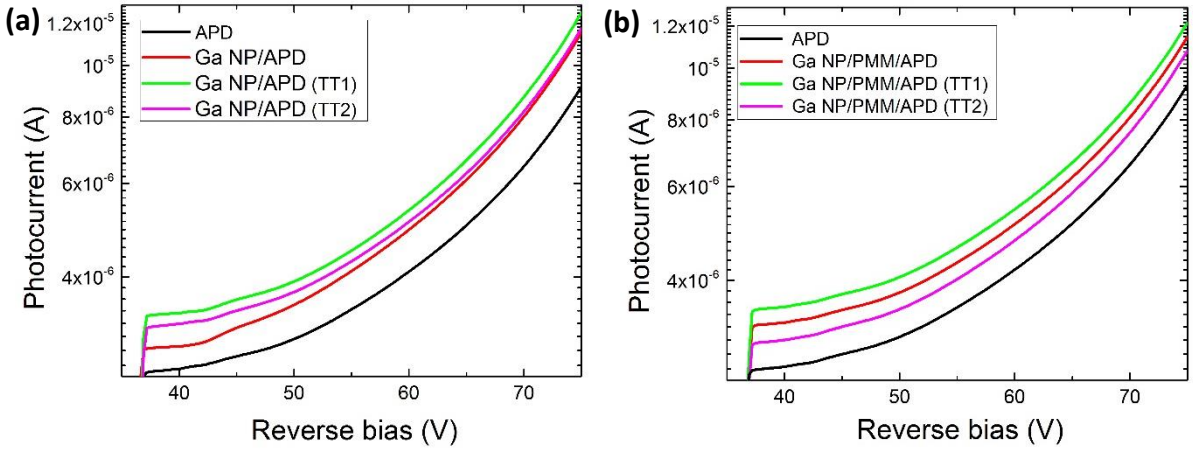


Figure 13: Comparison of the photocurrent characteristics of thermally modified (a) Ga NP/APD and (b) Ga NP/PMMA/APD structures.

# Conclusions

Generally, coating can be exploited to optimize the performance of optoelectronic devices following simulations and theoretical works.[18] Promising features of the Ga NPs for APD InGaAs/InAlAs infrared sensors modification have been investigated. Marked enhancement of the device light response has been observed due to the tunability of the outer gallium oxide shell using thermal treatments. The best result in terms of device dark current was achieved for evaporated Ga NP with average diameter of 23 nm with a surface coverage of 57% and the presence a pre-deposited PMMA layer to protect the mesa sidewalls. After TT1 thermal treatment the developed Ga NPs ARC ensured about 30% enhancement of the photocurrent signal.

# References


[1] A. Freundlich and A. Alemu, "Multi quantum well multijunction solar cell for space applications", physica status solidi (c) **2** (8), 2978 (2005).

[2] N. Vandamme, H. Chen, A. Gaucher, B. Behaghel, A. Lemaître, A. Cattoni, C. Dupuis, N. Bardou, J. Guillemoles, and S. Collin, "Ultrathin GaAs Solar Cells With a Silver Back Mirror", IEEE Journal of Photovoltaics **5** (2), 565 (2015).

[3] G. J. Bauhuis, P. Mulder, E. J. Haverkamp, J. C. C. M. Huijben, and J. J. Schermer, "26.1% thin-film GaAs solar cell using epitaxial lift-off", Solar Energy Materials and Solar Cells **93** (9), 1488 (2009).

[4] P. Spinelli, M. Hebbink, R. de Waele, L. Black, F. Lenzmann, and A. Polman, "Optical Impedance Matching Using Coupled Plasmonic Nanoparticle Arrays", Nano Letters **11** (4), 1760 (2011).

[5] T. F. Villesen, Christian Uhrenfeldt, B. Johansen, J. Lundsgaard Hansen, H. U. Ulriksen, and Arne Nylandsted Larsen, "Aluminum nanoparticles for plasmon-improved coupling of light into silicon", Nanotechnology **23** (8), 085202 (2012).

[6] N. P. Hylton, X. F. Li, V. Giannini, K. H. Lee, N. J. Ekins-Daukes, J. Loo, D. Vercruysse, P. Van Dorpe, H. Sodabanlu, M. Sugiyama, and S. A. Maier, "Loss mitigation in plasmonic solar cells: aluminium nanoparticles for broadband photocurrent enhancements in GaAs photodiodes", Scientific Reports **3**, 2874 (2013).

[7] Mehdi Keshavarz Hedayati and Mady Elbahri, "Antireflective Coatings: Conventional Stacking Layers and Ultrathin Plasmonic Metasurfaces, A Mini-Review", Materials **9** (6), 497 (2016).

[8] Mark W. Knight, Toon Coenen, Yang Yang, Benjamin J. M. Brenny, Maria Losurdo, April S. Brown, Henry O. Everitt, and Albert Polman, "Gallium Plasmonics: Deep Subwavelength Spectroscopic Imaging of Single and Interacting Gallium Nanoparticles", ACS Nano **9** (2), 2049 (2015).

[9] M. Rebien, W. Henrion, M. Hong, J. P. Mannaerts, and M. Fleischer, "Optical properties of gallium oxide thin films", Applied Physics Letters **81** (2), 250 (2002).

[10] Xiaofeng Fan, Weitao Zheng, and David J. Singh, "Light scattering and surface plasmons on small spherical particles", Light: Science &Amp; Applications **3**, e179 (2014).

[11] S. Catalán-Gómez, A. Redondo-Cubero, F. J. Palomares, F. Nucciarelli, and J. L. Pau, "Tunable plasmonic resonance of gallium nanoparticles by thermal oxidation at low temperatures", Nanotechnology **28** (40), 405705 (2017).

[12] L. G. Schulz, "The experimental study of the optical properties of metals and the relation of the results to the Drude free electron theory", Advances in Physics **6** (21), 102 (1957).

[13] Y. L. Goh, A. R. J. Marshall, D. J. Massey, J. S. Ng, C. H. Tan, M. Hopkinson, J. P. R. David, S. K. Jones, C. C. Button, and S. M. Pinches, "Excess Avalanche Noise in In0:52 Al0:48 As", IEEE Journal of Quantum Electronics **43** (6), 503 (2007).

[14] M. A. Itzler, r Ben-Michael, C. F. Hsu, K. Slomkowski, A. Tosi, S. Cova, F. Zappa, and R. Ispasoiu, "Single photon avalanche diodes (SPADs) for 1.5 μm photon counting applications", Journal of Modern Optics **54** (2-3), 283 (2007).

[15] Jun Zhang, Mark A. Itzler, Hugo Zbinden, and Jian-Wei Pan, "Advances in InGaAs/InP single-photon detector systems for quantum communication", Light: Science &Amp; Applications **4**, e286 (2015).

[16] M. Nada, Y. Muramoto, H. Yokoyama, T. Ishibashi, and H. Matsuzaki, in *Electronics Letters* (Institution of Engineering and Technology, 2013), Vol. 49, pp. 62.

[17] Lachlan E. Black, *New Perspectives on Surface Passivation: Understanding*. (Springer, Switzerland, 2016).

[18] Dehui Wan, Hsuen-Li Chen, Te-Chen Tseng, Cheng-Yi Fang, Yu-Shen Lai, and Fang-Yao Yeh, "Antireflective Nanoparticle Arrays Enhance the Efficiency of Silicon Solar Cells", Advanced Functional Materials **20** (18), 3064 (2010).

# Conclusiones

Se exponen aquí las principales conclusiones alcanzadas a lo largo de la tesis. El objeto del presente estudio fue el desarrollo de nanoestructuras de metal plasmónicas con el fin de mejorar la producción fotoeléctrica en dispositivos basados en sensores fotosensibles. Las estructuras fueron caracterizadas ópticamente y eléctricamente y se realizaron simulaciones para optimizar los parámetros de los procesos de fabricación. Asimismo, el desarrollo de nanopartículas (NPs) de galio coloidales permitió caracterizar la resonancia de absorción plasmónica tanto en distintos disolventes como en vacío.

El diseño de un nuevo método de sintetización de soluciones coloidales de galio permitió una síntesis rapida y eficaz en comparación con las técnicas descritas en la tabla 2.1. La producción mediante la evaporación termica del material garantiza la escalabilidad del proceso en grandes superficies. Dado que la mayoría de los métodos químicos requieren condiciones de reacción específicas, la utilización de NPs transferibles mediante el uso de una capa sacrificable da la posibilidad de crear coloidales para una amplia variedad de materiales y disolventes. Adicionalmente, los NPs podrían tener la posibilidad de ser caraterizadas y tratadas antes de ser dispersadas. Además, se identificaron los plasmones de superficie y volumen mediante la técnica EELS en los coloides preparados en colaboración con la universidad de Cadiz.

Se obtuvieron por primera vez nanoconos de Ga/GaOx mediante un proceso de ataque seco con plasma (RIE) de baja potencia, optimizando los parámetros del proceso de modificación estructural de las NPs. Este se ha demostrado ser un proceso fácil y rápido que puede ser aplicado en una amplia variedad de substratos. Dado que la capa más externa de GaOx se ha demostrado tener alta resistencia en altas temperaturas antes de experimentar cambios en su morfología, la estructura cónica desarrollada puede resultar útil para aplicaciones en las cuales la temperatura de trabajo sea un factor determinante.

Con respecto a las nanocolumnas de Si, estas estructuras se fabricaron utilizando las NPs de galio como mascara durante el proceso de ataque seco. Para dimensiones específicas, las estructuras desarrolladas mostraron una excelente propiedad antireflejante en el rango del infrarrojo cercano para cualquier estado de polarización de la onda incidente. Además, el uso de NPs como mascara, permite la elección de la dimensión y distribución de las nanocolumnas, lo cuál es un factor determinante de las propriedades de la capa antireflejante.

Se consiguió controlar la distribución de las NPs mediante ataque químico en HCl. Normalmente, las técnicas de crecimiento apenas permiten cambiar la densidad superficial de las estructuras. El tratamiento con HCl nos permite alterar este parámetro, siendo además compatible con la gran mayoría de procesos de microfabricación de dispositivos electrónicos

Se ha demostrado que la presencia de NPs de galio reduce la reflexión de la luz incidente sobre superficies de InAs y cuarzo. Mediante medidas de reflexión a diferentes ángulos se corroboró la mejora en el ángulo de admisión de luz en la superficie modificada con NPs. Por último, la evaporación de NPs de galio con un diámetro medio de 23nm y un factor de recubrimiento del 57% provocó una mejora de la eficiencia de fotodiodos de avalancha de alrededor de un 30%, tras tratamientos térmicos que condicen a la alteración de las proporciones núcleo-corteza en la estructuras y a un cambio en la permitividad dieléctrica de las mismas.

# Trabajo futuros

El presente estudio de las propiedades de NPs de galio permite el desarrollo futuro de revestimientos funcionales novedosos para dispositivos optoelectrónicos. Aprovechando la resonancia plasmónica del galio, las nanoestructuras desarrolladas (nanopirámides, nanocolumnas y núcleo-corteza), pueden utilizarse para implementar

biosensores altamente sensibles debido a las mejoras del campo cercano alrededor de las estructuras. De hecho, dentro de las variedades de NPs utilizadas para modificar sensores electroquímicos, la estructura núcleo-corteza Ga/GaOx puede ser de interés.[1] Recientes estudios demostraron su biocompatibilidad, posibilidad de modificación de la estructura y del proceso de evaporación y sintesis coloidal.[2] También, dado que el coste, la caracterización y la toxicidad de electrodos con metales comunes todavía no tiene la madurez suficiente para su producción a gran escala, las NPs de galio pueden contribuir al desarrollo de nuevas soluciones. Además, las últimas investigaciones sobre el acoplo del campo cercano entre Ga NP y otros materiales de nanoestructura metálica han sido prometedoras para implementar aplicaciones SERS (Surface-Enhance Raman Spectroscopy) en un amplio rango del espectro. Por último, la resistencia de las estructuras de galio en entornos ácidos hostiles puede ser aprovechada para el desarrollo de fármacos para tumores y algunos casos de cáncer donde las células enfermas cercanas a la solucion pueden reducir el nivel de pH debido a condiciones específicas.[3]

Aún así, las nanoestructuras optimizadas en este trabajo mostraron una propiedad antireflectante en un amplio rango del espectro y sería interesante investigar sus usos para otras longitudes de onda superiores a los 1.55 μm. Actualmente los rangos del infrarrojo medio y lejano han sido en su gran mayoría utilizados para telecomunicaciones de larga distancia y aplicaciones de escáner térmico. La optimización de ARCs para estos sensores ha sido objeto de estudio especialmente en ámbitos espaciales dónde la fiabilidad y la estabilidad a bajas temperaturas son indispensables. El punto de congelación del núcleo líquido de galio de -128 °C hace de las nanoestructuras de NPs de galio un válido candidato para la mejora del rendimiento de los sensores para aplicaciones en el espacio y climas extremos.

Aunque las aplicaciones fotovoltaicas y de sensores de luz, se han estudiado ampliamente a lo largo de los años, aún se buscan nuevas formas de optimización de la eficiencia, la variación de parámetros como la densidad de NPs, el tamaño, la geometría o el orden, permiten, en el caso de las nanoestructuras de galio, mejorar la eficiencia más allá de la conseguida por técnicas antireflectantes convencionales, especialmente para

dispositivos semiconductores no convencionales. De hecho, muchos materiales habitualmente utilizados en ARCs, no permiten un control sencillo de la permitividad para conseguir las condiciones antireflectantes óptimas descritas en el Capítulo 2. Cuando las NPs se depositan en la superficie del dispositivo, la resonancia plasmónica generada podría aumentar el campo eléctrico localmente, mejorando la eficiencia si ese aumento tiene lugar cerca de la región activa del dispositivo. Dado que los niveles de atrapamiento y su distribución geométrica depende del campo eléctrico interno, la NP puede mejorar el rendimiento del equipo especialmente en rangos de operación de alto voltaje.[4]

Pero no solo los sensores pueden aprovecharse de estas estructuras. Trabajos anteriores mostraron que reducir la superficie de reflexión y cambiar la morfología de la misma pueden ser aspectos clave para el desarrollo de dispositivos de fuentes de luz como los LED. Se ha demostrado que una superficie rugosa puede mejorar la eficiencia de extracción rompiendo la simetría y que las NPs depositadas en superficie pueden contribuir a generar este efecto.[5] En aplicaciones LED basadas en pozos cuánticos, las NPs de galio parcialmente o completamente oxidadas pueden conseguir una mejor de la probabilidad de inyección y extracción de luz, debido a que el band-gap del Ga Ox y su efecto en la dispersión de la luz son adecuados para ese propósito. [6,7]

# Conclusion

Herein, the main conclusions of the thesis work are presented. The study aimed to develop metal plasmonic nanostructures, in order to enhance the photoelectric yield in light sensor devices. The structures were optically and electrically characterized and simulations were run to optimize the fabrication processes parameters. Moreover, the development of colloidal Ga NPs gave the chance to fully characterize the plasmonic absorption resonance either in various medium or under vacuum.

The design of a new Ga colloidal solution method allowed a fast and yielding synthesis compared to others techniques shown in table 2.1. The production via material thermal evaporation guarantees high process scalability, with theoretical large surfaces coverage. Since most the chemical methods need specific reaction conditions, using transferable NPs from an expendable layer gives the possibility to create colloidal of a large variety of materials and solution. Additionally, the NPs can be characterized and pre-treated before being dispersed. Thanks to this achievement, surface and bulk plasmon were identified by EELs technique in collaboration with the University of Cadiz.

Original Ga/GaOx nanocones were obtained by means of low power RIE process, optimizing the sputtering process parameter such as time and power. It has been found an easy and fast one step process that can be implemented on a large variety of substrates. Since the Ga Ox shell shows high temperature resistance before suffering structural changes, the cone shell structure can find use in harsh working environment.

Capped Si nanocolumns were fabricated using Ga NPs as hard-mask. For a specific column aspect ratio, the developed structure showed excellent antireflective property in the near IR range for all the polarization states. Moreover, the use of NPs as hard mask allows to select the nanocolumns dimension and distribution.

Finally, the thermal evaporated NPs coverage was successfully controlled via wet HCl etching method. Usually, growth technique barely allows to change coverage rate and structure dimension distribution. The treatment allows to manipulate these parameters. Furthermore, the used HCl acid is compatible with most of the electronic device processes, hence an easier integration during the fabrication steps

The presence of treated Ga NPs has been also demonstrated to lower reflectivity of InAs and quart surface material. The tilted angle measurements attested the enhanced light acceptance angle of the NPs modified surface. Finally, evaporated Ga NPs with average dimeter of 23 nm and surface coverage factor of 57% were deposited on an APD device surface leading to an enhancement of the light conversion performance of about 30 %. The

peculiar core-shell structure allows high permittivity tunability of the effective layer by cost-effective thermal treatments.

# Future works

The presented study of the optical and structural properties of the Ga NP supports the idea of future development of innovative functional coating in optoelectronic devices. Taking advantages of the plasmonic resonance of Ga, the developed nanostructures (nanopyramids, nanocolumns and core-shell) can be used to implement highly sensitive biosensors due to the near field enhancement around the structures. In fact, among many of the metal/oxide NPs used for electrochemical sensor systems, the Ga/Ga Ox core-shell can still contribute.[1] Recent studies demonstrated its biocompatibility, high tunability of the structure and evaporation and colloidal feasibility. [2] Since the cost, the characterization and the toxicity of common metal NPs electrodes still have not reach the appropriate ripeness for large scale sensor production, Ga NPs may help to develop solutions for the electrochemical sensors of the futures. Also, further investigations about the near-field coupling between Ga NP and other metal nanostructure material can be promising to implement SERS (Surface-Enhance Raman Spectroscopy) applications in a broad spectral range. Finally, the endurance of the Ga structures in harsh acid environment can be exploited for the drug delivery application for tumors and cancer cases, where the target ill cell of the surrounding solution can drop off the pH level due to specific conditions. [3]

Nevertheless, optimized nanostructures in this work showed antireflective property in a wide range of the spectrum and it is reasonable to investigate their use for other working wavelengths beyond 1.55 µm. Nowadays, the mid and far IR range

have been largely used for long distance telecommunication and thermal imaging applications. Optimization of the ARCs for these sensors has been subject of study especially for space purposes, where reliability and low temperature stability is a must. The liquid Ga core freezing point of -128 °C makes the Ga NP nanostructures a suitable candidate for out-space sensor performance enhancement.

Regarding the photovoltaic and light sensors applications, they have been largely studied along the years but investigation that possibly may involve Ga nanostructures are possible. The variation of parameters such as NP density, size, geometry, or ordering can allow efficiency improvements beyond those achieved by conventional antireflective techniques, especially for the no conventional semiconductor devices. In fact, common materials used in ARCs cannot be easily tailored in terms of permittivity to match the optimal antireflective conditions described in Chapter 2. Additionally, when NP are presented on the device surface, the generated plasmonic resonance may give the chance to interact with the device field configuration because of the near field enhancement effect. Since the trapping levels and their distribution depend on it, the NP could improve the device performance especially during the high voltage operation range.[4]

But not only sensors can take advantages from these potentially high tunable structures. Previous works in literature demonstrated that lowering the surface reflection and changing the surface morphology can be a key features for the development of future light source like the light emitting diodes (LEDs). It has been demonstrated that surface roughening can enhance the light extraction efficiency [5] and NP can relatively control and parametrize the surface breaking symmetry. Regarding the quantum LED applications, partially or completely oxide Ga nanostructures can be investigated to achieve a better infection chance and higher

light extraction, since the large Ga Ox band gap and the scattering behavior can be suitable for those purpose. [6] , [7]

# Reference


[1] Jaise Mariya George, Arun Antony, and Beena Mathew, "Metal oxide nanoparticles in electrochemical sensing and biosensing: a review", Microchimica Acta **185** (7), 358 (2018).

[2] Philippe Collery, Bernhard Keppler, Claudie Madoulet, and Bernard Desoize, "Gallium in cancer treatment", Critical Reviews in Oncology/Hematology **42** (3), 283 (2002).

[3] Robert Griffiths, "Are cancer cells acidic?", British journal of cancer **64** (3), 425 (1991).

[4] Alberto Tosi, Alberto Dalla Mora, Franco Zappa, and Sergio Cova, "Single-photon avalanche diodes for the near-infrared range: detector and circuit issues", Journal of Modern Optics **56** (2-3), 299 (2009).

[5] Yu Jo Lee et al, "Increasing the extraction efficiency of AlGaInP LEDs via n-side surface roughening", IEEE Photonics Technology Letters **17** (11), 2289 (2005).

[6] Huaibin Shen, Qinli Lin, Hongzhe Wang, Lei Qian, Yixing Yang, Alexandre Titov, Jake Hyvonen, Ying Zheng, and Lin Song Li, "Efficient and Bright Colloidal Quantum Dot Light-Emitting Diodes via Controlling the Shell Thickness of Quantum Dots", ACS Applied Materials & Interfaces **5** (22), 12011 (2013).

[7] Yong Tang, Zhi Li, Zong Li, Jia Li, Shu Yu, and Long Rao, "Enhancement of Luminous Efficiency and Uniformity of CCT for Quantum Dot-Converted LEDs by Incorporating With ZnO Nanoparticles", IEEE Transactions on Electron Devices **65** (1), 158 (2018).

# Contributions

Herein a list of the student's output at national and international conferences:

1) *Enhancement of InGaAs/InAlAs avalanche photodiodes response using gallium nanoparticles coating,* **Flavio Nucciarelli**, Sergio Catalán Gómez, Anthony Krier, Chee Hing Tan, Carlos Rivera, José Luis Pau, **SPIE Optic+Photonic, San Diego 2018** (Poster)

2) *Optical coatings based on metal-oxide gallium nanoparticles for optoelectronic devices*, **Flavio Nucciarelli**, Eva Repiso, Peter James Carrington, Anthony Krier, Jose Luis Pau, **SPIE Photonic West, San Francisco 2018** (Talk)

3) *Novel strategy for developing antireflective coating based on liquid metal,* Flavio Nucciarelli, Sergio Catalan-Gomez, Gema Tabares, Jose Luis Pau, **XX Young Researchers Meeting, Madrid 2017** (Talk)

4) *Colloidal gallium nanoparticles: synthesis and UV absorption,* **F.Nucciarelli**, I.Bravo, S. Catalan-Gomez, L. Vázquez, E.Lorenzo, J.L. Pau*,* **7th early stage researchers workshop, Madrid 2017** (Poster)

5) *Thin gallium nanoparticles layer coating for infrared sensor functionalization,* **F.Nucciarelli**, C.H.Tan, X.Zhou, C. Rivera, J.L. Pau, S.Catalán-Gómez*,* **SPIE Optics and Optoelectronics, Prague 2017** *(Poster)*

6) *Surface-enhanced absorption on InGaAs/InAlAs avalanche photodiode structures operating at 1.55 um by gallium nanoparticles evaporation,* **F.Nucciarelli**, C.H.Tan, X.Zhou, J.S.Ng, C. Rivera, J.L. Pau, **19th International Conference on Molecular Beam Epitaxy, Montpellier 2016** (Poster)

He also attended several international workshops and seminars:

1) Workshop of the Marie-Curie international training network PROMIS at the University of Cadiz on design and simulation of photonic structures *(2016/2017)*

*https://www.portaldecadiz.com/provinciacadiz/20387-expertos-internacionales-en-la-uca-durante-el-ii-workshop-sobre-modelado-y-diseno-en-fotonica*

2) Summer school at the University of Montpellier on epitaxial growth techniques on semiconductor substrates *(2016/2017)*

   *http://www.physics.lancs.ac.uk/promis/news/002899/promis-summer-school-and-mbe16-conference-montpellier-31st-august--9th-september*

3) Workshop of the Marie-Curie international training network PROMIS at the University of Nottingham about opportunities in academia and industry *(2018/2019)*

   *https://www.nottingham.ac.uk/physics/events/nano11022015.aspx*

This thesis jointly to other collaboration works generated the following peer-reviewed publications as author or co-author:

1) *High Ultraviolet Absorption in Colloidal Gallium Nanoparticles Prepared from Thermal Evaporation,* ***F.Nucciarelli****, I.Bravo, S. Catalan-Gomez, L. Vázquez, E.Lorenzo, J.L. Pau,* Nanomaterials *2017, 7(7), 172*

2) *Gallium nanoparticles colloids synthesis for UV bio-optical sensors,* ***F.Nucciarelli****, I.Bravo, S. Catalan-Gomez, L. Vázquez, E.Lorenzo, J.L. Pau, Proc. SPIE 10231, Optical Sensors 2017, 1023127 (16 May 2017)*

3) *The role of the oxide shell in the chemical functionalization of plasmonic gallium nanoparticles, S. Catalán-Gómez, M. Briones, A. Redondo-Cubero, F. J. Palomares,* ***F. Nucciarelli****, E. Lorenzo, and J. L. Pau, Proc. SPIE 10231, Optical Sensors 2017, 102310D (16 May 2017)*

4) *Tunable plasmonic resonance of gallium nanoparticles by thermal oxidation at low temperatures, S. Catalán-Gómez, A. Redondo-Cubero, F. J. Palomares,* ***F. Nucciarelli*** *and J. L. Pau,* Nanotechnology, Volume 28, Number 40

5) *Size-selective breaking of the core–shell structure of gallium nanoparticles, S. Catalán-Gómez, A. Redondo-Cubero, F. J. Palomares, L. Vazquez, E. Nogales,* ***F. Nucciarelli****, B. Mendez, N. Gordillo and J. L. Pau,* Nanotechnology, Volume 29, Number 35

6) *Self-assembly of higly ordered plasmonic gallium nanoparticles driven by nanopatterning, S. Catalán-Gómez, C. Bran, N. Gordillo,* ***F. Nucciarelli****, L. Vazquez, J. L. Pau and A. Redondo-Cubero,* Nanofuture, Volume 2, Number 4

7) *Photoluminescence enhancement of monolayer MoS2 using plasmonic gallium nanoparticles, S. Catalán-Gómez, S. Garg, A. Redondo-Cubero, N. Gordillo, A. deAndres,* ***F. Nucciarelli****, S. Kim, P. Kung and J.L. Pau, Nanoscale Advances 1.2 (2019), 884-893*